Dissertation zur Erlangung des Doktorgrades

der Fakultät für Chemie und Pharmazie

der Ludwig-Maximilians-Universität München

Evaluation of Cyclic Dinucleotides and their Prodrugs in Biochemical and Cellular Assays

Dilara Özdemir

aus

Karlsruhe, Deutschland

2023

Erklärung

Diese Dissertation wurde im Sinne von §7 der Promotsionsordnung von 28. November 2011 von Herrn Prof. Dr. Thomas Carell betreut.

Eidesstattliche Versicherung

Diese Dissertation wurde selbstständig und ohne unerlaubte Hilfe erarbeitet.

München, 16.01.2023   ………………………

                                                                              Dilara Özdemir

Dissertation eingereicht am: 17.01.2023

1. Gutachter: Prof. Dr. Thomas Carell

2. Gutachter: Dr. Pavel Kielkowski

Mündliche Prüfung am: 17.02.2023

"We carry inside us the wonders we seek outside us."

Rumi

"Karanlıkta yanabilirim

Boşlukta durabilirim

Düşmem ben, kanatlarım var ruhumda"

Nil Karaibrahimgil

Bana hep inanan sevgili aileme

Published Work

- Veth, S.*, Fuchs, A.*, Özdemir, D.*, Dialer, C., Drexler, D., Knechtel, F., Witte, G., Hopfner, K., Carell, T. and Ploetz, E., 2022. Chemical Synthesis of the Fluorescent Cyclic Dinucleotides cthGAMP. *ChemBioChem* **23**, (2022).

- Stazzoni, S., Böhmer, D. F. R., Hernichel, F., Özdemir, D., Pappa, A., Drexler, D., Bauernfried, S., Witte, G., Wagner, M., Veth, S., Hopfner, K., Hornung, V., König, L. M. & Carell, T. Novel Poxin Stable cGAMP-Derivatives are Remarkable STING Agonists. *Angew. Chem. Int. Ed.* **61**, (2022).

- Traube, F.R., Özdemir, D., Sahin, H., Scheel, C., Glück, A., Geserich, A., Oganesian, S., Kostidis, S., Iwan, K., Rahimoff, R., Giorgio, G., Müller, M., Spada, F., Biel, M., Cox, J., Giera, M., Michalakis, S. & Carell, T. Redirected Nuclear Glutamate Dehydrogenase Supplies Tet3 With α-Ketoglutarate in Neurons. *Nat. Commun.* **12**, (2021).

*These authors contributed equally.

Conference and Meeting Attendances

- Traube, F., Özdemir, D., Scheel, C., Michalakis, S., Carell, T. Gdh interacts with Tet3 to supply α-ketoglutarate, linking 5mdC oxidation to neuronal function and metabolic state. Poster Presentation at the EMBL Symposium Metabolism meets Epigenetics **2019**, Heidelberg (Germany).

Acknowledgements

were just the right thing to give our thinking-brains a break. To *Leander* and *Timm* I would like to thank for their navigational help in the lab and their rare but epic music moments. Overall, we managed to leave the stress out thanks to your good mood and calmness.

To my second and irreplaceable lab partner, *Henning Nissen*, I would like to thank as well. It was a relatively short time we have spent in the little biochemistry lab, but the best experience for me. We had a great dynamic and respected each other and were always there to talk about things and experiments which bothered us. Thank you for being such a nice and kind lab partner.

I would like to thank our bouldering group of the lab, with whom I discovered my favourite sports with. *Dr. Martin Rossa*, *Dr. Leander Runtsch*, *Dr. Bastien Viverge*, *Dr. Rene Rahimoff* and of course *Eva Korytiakova*, thank you for all the experiences we had both in the bouldering gym and outdoors climbing. It was the best way to clear my head after a long work day and the fact that there was always someone motivated to go, no matter how tiring the day was, was a huge motivation to me too.

I would like to thank *Dr. Antony Crisp* for accepting me as a friend from the first day on. Thank you for introducing me to your friends-group which helped me with my integration in Munich. Also, I would like to thank for the jam sessions we had every now and then which were a real pleasure.

I would like to thank *Ece Büber* as well for being my friend and tea-break partner in the campus. Thank you for hunting me down and becoming one of my closest friends! I value the time we have spent having fun in our mother language. You are one of the people who brings the sunshine on grey and rainy days of Munich. Your thoughtfulness and quality-time you provide as a friend is a treasure to me.

I would like to thank specifically to the group of people I have spent most of my time with in the last two years, during and after working hours with our lunch cookings, aperitivos, our "wedding" parties, beer and wine tastings, brunches, our creative parties or just a bottle of "feierabend"-beer on the legendary couch. *Felix Xu*, thank you for your quirky mindset and introducing us to Kimchi fried rice. *Giacomo Ganazzoli*, thank you for your exquisite jokes and teachings on how to eat mayonnaise in 101 ways. *Fabian Hernichel*, thank you for the best tasting burgers and meat you have prepared for us and being the mediator in passionate discussions. *Aikaterini Pappa*, thank you for your healthy cookings and showing us how to enjoy the moment. *Johann de Graaff*, thank you for teaching us how to make dumplings and encouraging our relationship with beer-pong. These experiences can not be replaced by any other. Thank you for the shared fun moments. Additionally, I would like to thank Simon Veth, Annika Tölke, Corinna Sommermann, Yasmin Gärtner and Markus Hillmeier for nice and special times.

A bucket of flowers and thank you notes I would like to give to my dearest friend *Eva Korytiakova*. Without you my PhD experience wouldn't be the same. Your friendship was my safe space and support from day one until the end. I value a lot the times we have spent for mental support and your patience and loving kindness. On the other hand, I always visited your lab for some fun, laughter, good music and weird dancing challenges. The humour we shared was the most uplifting thing to experience on days when simply nothing was working. With no doubt, no party, no coffee break, no music session would have been as it was with you. Thank you for all the laughter and heart-felt moments we had.

A very special thank is for my girls *Aysu Senyüz*, *Hamide Keskin*, *Tugce Köroglu* and *Öykü Arslantay*. Our longlasting friendship since the days we spent in Bogazici is just magnificent. Even though after our graduation we ended up taking academic routes and jobs in different corners of the world, our connection was so strong to check on each other whenever we wanted. Our long video chats we had were not replacing our meetings in person, but those nights were the most fun and dynamic hours of the day. I am so happy that we, as a very diverse group of women, stick with our friendship and cherish it. Thank you so much for all the motivation and support. I am looking forward to dance at your weddings!

I would like to thank *Fabian Hernichel*, first of all for supporting me the whole time of my thesis writing period. The challenges which came with it were made easier simply with your presence. Thank you for being there and listening to me when I needed to talk and a being the second pair of eyes for my thesis. Secondly, I would like to thank you for being my rock when times were getting really hard due to the pandemic. With my family being far away, you have provided me the care and sympathy with a big heart and never judged me when I couldn't handle the homesickness. I am so grateful for your presence in my life. With you I managed to have fun on long board-game nights, cooking sessions and movie nights which gave me the power to move on and renew my energy for my lab work. Thanks to you, I have discovered a new sense of happiness. I am looking forward for the adventures we will take on next.

Last but not least, I would like to thank my family from the bottom of my heart, for their support and love they have provided which led me to start my PhD. Thank you for believing in me and supporting me with my decisions. Without you I wouldn't be able to start a new life in Munich. Thank you for the cheerful phone talks we had during the pandemic. It was always motivating to know that whenever I needed a breeze from home, I could talk to you and you were there 24/7. I am looking forward to make up for the time we have lost due to travel restrictions and spend time with you on important days and moments. I love the fact that as a family we carry a lot of diversity and are dynamic, young and free-spirited. I am looking forward to see you soon!

Table of Contents

Abstract

The innate immune pathways gained more importance since the discovery of the extended role of type I interferons. Type I interferons are produced primarily upon viral and bacterial invasions and function by inducing immune responses. As a result, innate and adaptive immune cells are differentiated, activated and recruited to the pathogen-invaded cells for destruction. Type I interferons are also produced by cancer cells and immune cells regulating the cancer immunity cycle. The cGAS-STING pathway is one of the key pathways resulting in type I interferon mediated immune response.

The cGAS-STING pathway is activated by double-stranded DNA (dsDNA) leaking into the cytosol. When cGAS (<u>c</u>ytosolic-<u>G</u>uanosine-<u>A</u>denosine-<u>S</u>ynthase) binds to dsDNA, ATP and a GTP are utilised for the production of cyclic guanosine monophosphate-adenosine monophosphate (cGAMP). cGAMP binds to STING (<u>St</u>imulator of <u>I</u>nterferon <u>G</u>enes), initiating a signalling cascade. The high rate of chromosomal instabilities in cancer cells as well as the instability of genetic material in aged cells are reasons for dsDNA to leak out from the nucleus and localise in the cytosol. Hence, the cGAS-STING pathway is activated and immune cells are recruited to the site of danger. In recent years, targeting the cGAS-STING pathway has been an emerging strategy for drug discovery and led to the development of cGAMP analogues.

The group of *Carell* has designed and synthesised cyclic dinucleotides as STING agonists (Figure I). In the first part of this thesis, the cyclic dinucleotides and their developed prodrugs were evaluated using cellular and biochemical assays. Their rate of inducing type I interferon production was monitored in THP-1 monocytic cells. Their effective concentration 50 (EC_{50}) were measured and promising cGAMP analogues were tested for their stability against currently known cGAMP degrading enzymes. Two compounds, the 2',3'-dideoxy-cGAMP and 2',3'-dideoxy-cAAMP, were identified to be stable against poxins, which are viral enzymes from the poxvirus family. Two prodrugs of 2',3'-dideoxy-cAAMP were synthetically developed by the group of *Carell*, one of them containing the SATE linkers, named PRO1, another one bearing an additional photocleavable group named PC-PRO1. These were also evaluated regarding their rate of type I interferon production. With an EC_{50} value of 49 nM, PRO1 shows a 1500-fold increase in interferon production in THP-1 monocytic cells compared to its precursor 2',3'-dideoxy-cAAMP and a 200-fold increase compared to natural cGAMP (2',3'-cGAMP, Figure I).

Abstract
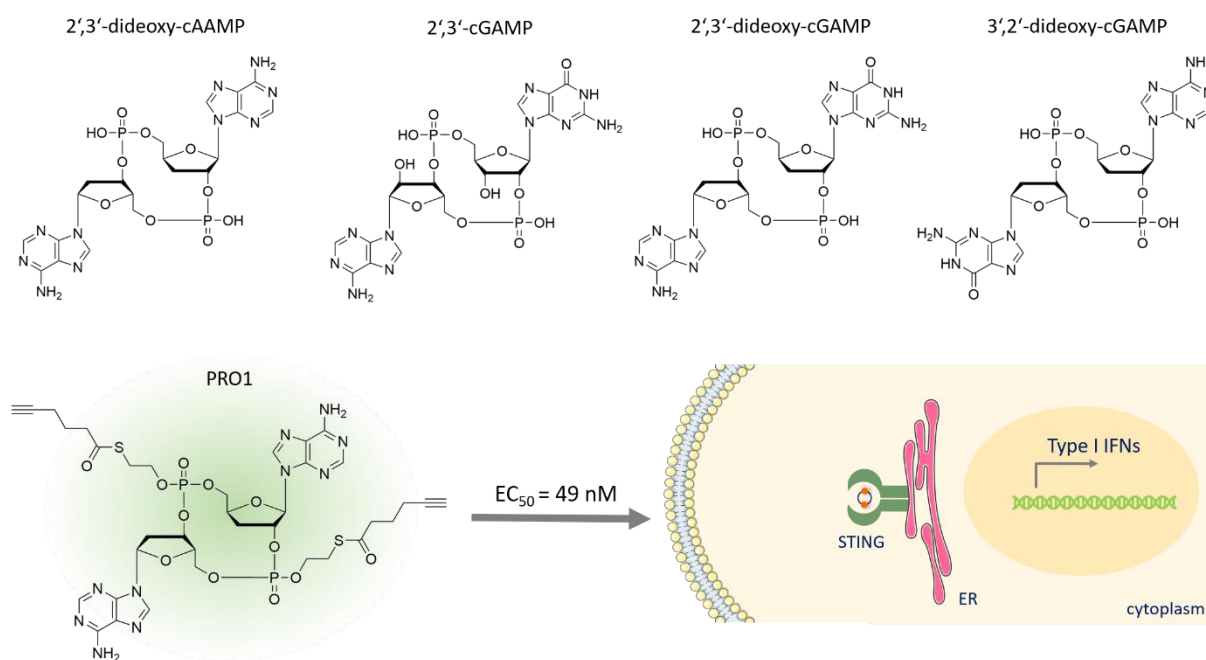
Figure I: Structures and function of agonists for STING.

Overactivation of STING and overproduction of type I interferons is related to specific diseases, aging, and metastatic activity in cancers. Therefore, besides STING agonists, STING antagonists also carry a therapeutic potential. For the development of a STING antagonist, *G. Ganazzoli* from the *Carell* group used the PROTAC (Proteolysis Targeting Chimera) approach utilising 2',3'-dideoxy-cGAMP as a STING recruiter (Figure II). This compound named PROTAC1, was evaluated in the second part of this thesis for its ability to degrade STING in different time frames. The analysis was done on THP-1 monocytic cells and western blotting was used in which the degree of STING degradation was measured by the intensity of the STING-antibody bound bands. As an internal control, the CoxIV of each sample was targeted and their band intensities were used for normalisation of the STING signal. A successful degradation of STING in THP-1 monocytic cells was observed when 25-50 nM of PROTAC1 was applied to the cells for 16 hours.
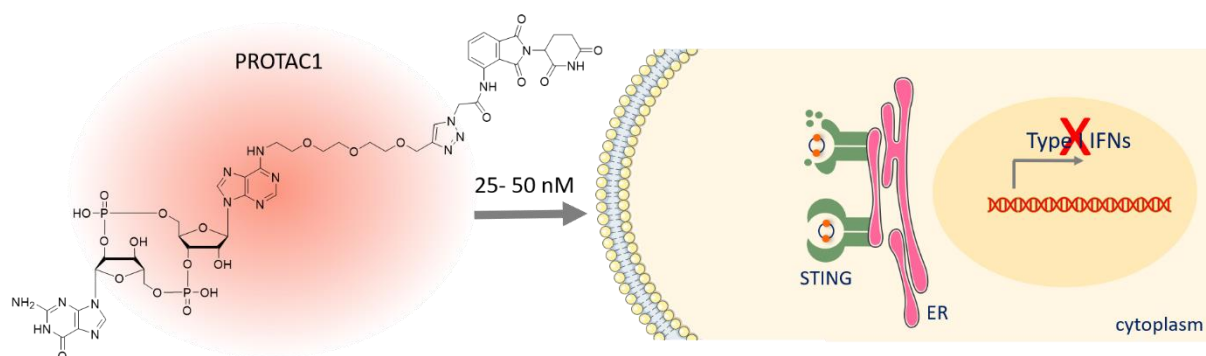
Figure II: Structure and function of the antagonist for STING.

In the published work in section 5 of this thesis, the chemical synthesis of a fluorescent cGAMP analogue, cthGAMP, was introduced. The successful entry of cthGAMP was observed in THP-1 monocytic cells with two-photon excitation microscopy. Interferon production was observed

when cthGAMP was transfected in the THP-1 monocytic cells, providing proof of biological activity. This compound was suggested for assay development purposes concerning the cGAS-STING pathway, due to its scalability of its synthetic route and biological activity.

In the second research article presented in section 5, the supply mechanism of α-ketoglutarate to the dioxygenase TET3 by the metabolic enzyme Gdh was described in hippocampal neurons for the oxidation process of 5'-methylcytosine. The oxidation of 5'-methylcstosine to 5'-hydroxymethylcytosine was observed upon Gdh localisation in the nucleus together with TET3. A functional Gdh was required for this conversion in activated hippocampal neurons. In this study, HEK293 cells were used for expression and co-expression of natural and modified enzymes, which were used for immunocytochemistry experiments. Hippocampus slices from mice were used for neural activation, immunohistochemistry and proximity ligation assays. Observations were made by confocal microscopy, whereas quantification of 5'-methylcytosine and its oxidation products were done by UHPLC-QQQ-MS.

1 Introduction

1.1 The Immune System

Higher organisms, have evolved a complex signalling network against intruding pathogens and other environmental threats, called the immune system. This network involves a broad spectrum of responses including small molecules, large proteins, and different classes of highly specified cells. The system entails the lymphatic system which reaches organs and permeates entire regions of the body[1].

In humans, the immune system is comprised of two parts, the innate and the adaptive immune system[2]. An initial molecular response against pathogens is provided by the innate immune system. It is, for example, able to recognise parts of the bacterial membrane and foreign particles, genetic material and viral particles, all of which are named pathogen-associated molecular patterns (PAMPs)[3]. On the other hand, it can also recognise endogenous molecules of the body signalling a malfunction such as cell debris released from dead cells or secreted signalling molecules, all of which are called danger-associated molecular patterns (DAMPs)[4]. All are recognised by pattern recognition receptors (PRRs) which are always present and therefore quick to respond by triggering downstream immune signalling via a variety of innate immune cells (Figure 1).

If the pathogen cannot be eliminated by the innate immune system, the adaptive immune system is activated[5]. In this slower yet targeted response, antigen-specific receptors are developed by lymphocytes. Those consist of B cell and T cell lymphocytes, which produce antibodies and provide cell-mediated responses (Figure 1). The antibodies bind to the specific antigen and prevent interaction with the host. Produced antibodies are saved as a repertoire in the immunological memory and can provide life-long immunity[6].
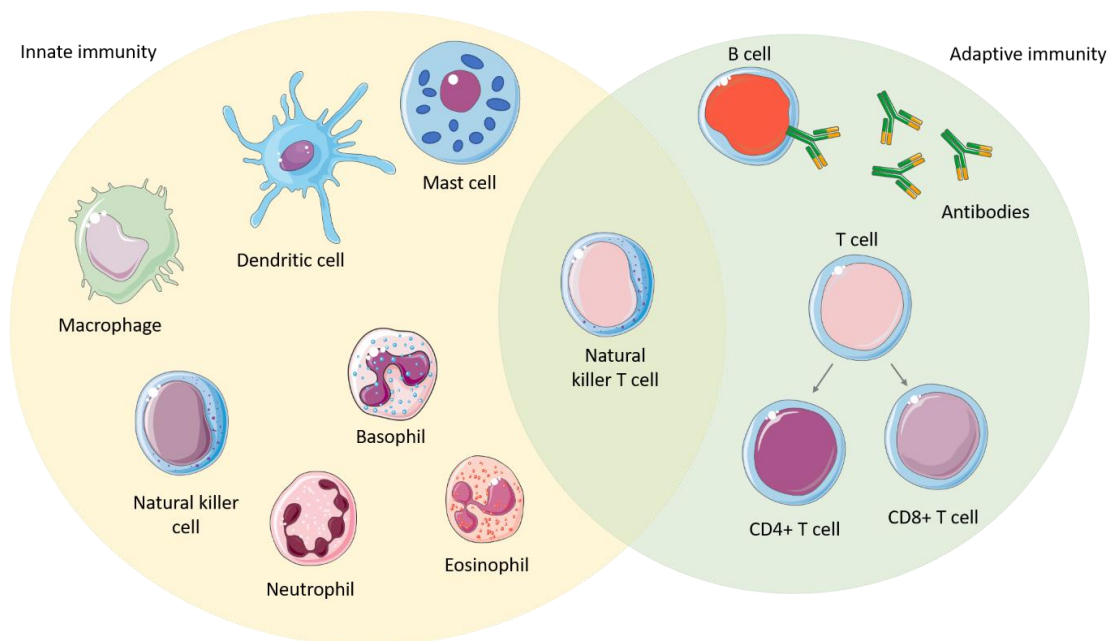
Figure 1: Cells of the innate and adaptive immune system.

1.2 The Innate Immune System

The innate immune system is an evolutionary older defence mechanism with which human beings are born with. The skin and mucous membranes layering inner organs serve as a first physical barrier against pathogens and are considered as a part of innate immunity. When these layers are injured and cannot prevent the pathogen intrusion, molecular cascades and various cell types of the innate immune system are activated. PAMPs and DAMPs are exposed to PRRs, which signal downstream to adaptor proteins and prepare an immune response by activating transcription factors. Interferons and cytokines are produced in response to attract macrophages, natural killer cells and other cell types to clear the site of injury or danger. This type of response is generally the same towards the various types of stimuli. The innate immune system is therefore also called the "nonspecific" immune system.

Among all types of PAMPs and DAMPs one very important stimulus for the innate immune system is genetic material. Single-stranded RNA (ssRNA), double-stranded RNA (dsRNA), single-stranded DNA (ssDNA), double stranded DNA (dsDNA) or DNA:RNA hybrids are sensed by specific PRRs (Figure 2)[7,8]. Whether it is bacterial, viral, or derived from the host, all forms of genetic material are recognised by specialised receptors. These receptors can be cell membrane bound or endosomal receptors as well as cytosolic receptors (Figure 2)[9–11]. In eukaryotic cells the host DNA, in other words self-DNA, is packaged and confined in a membrane-bound space. Upon cell stress or in the wake of certain signalling cascades, self-DNA may leak into the cytosol of the cell, where it is recognised by specific cytosolic PRRs. DNA sensing PRRs do not discriminate between foreign and host DNA.

PRRs function downstream through adaptor proteins (Figure 2). These adaptor proteins activate IκB kinase-ε (IKKε) and TANK-binding kinase I (TBK1), both of which phosphorylate Interferon Regulatory Factor 3 (IRF3), IRF7, or free <u>N</u>uclear-<u>F</u>actor-<u>kappa</u> light-chain enhancer of activated <u>B</u> cells (NF-κB). These transcription factors travel to the nucleus, triggering type I interferon production (IFNs), and the formation of other cytokines, chemokines along the NF-κB pathway[12,13]. Type I IFNs are small proteins interfering with viral infection, taking part in inflammation and immunoregulation. Among the type I IFNs there are 13 homologs of IFN-α and one IFN-β[14]. IFN-α is released mostly from plasmacytoid dendritic cells (DCs), whereas IFNβ can be released from all nucleated cells[15,16]. IFN-I subtypes bind to the interferon-alpha/beta receptors (IFNAR) with different affinities, thereby determining downstream signalling and gene expression profiles (Figure 2)[17]. At the end of the cascades, Interferon Stimulated Genes (ISGs) are transcriptionally activated[18]. There is a permanent basal level of released IFN-I signalling to keep the cells prepared for any environmental challenge[19]. NF-κB can induce two signalling pathways, the canonical and non-canonical NF-κB[20]. Both are involved in immune mechanisms, whereas the canonical NF-κB pathway responds to a broader set of signalling molecules[20–22]. NF-κB pathways are activated both in innate and adaptive immune systems[23].
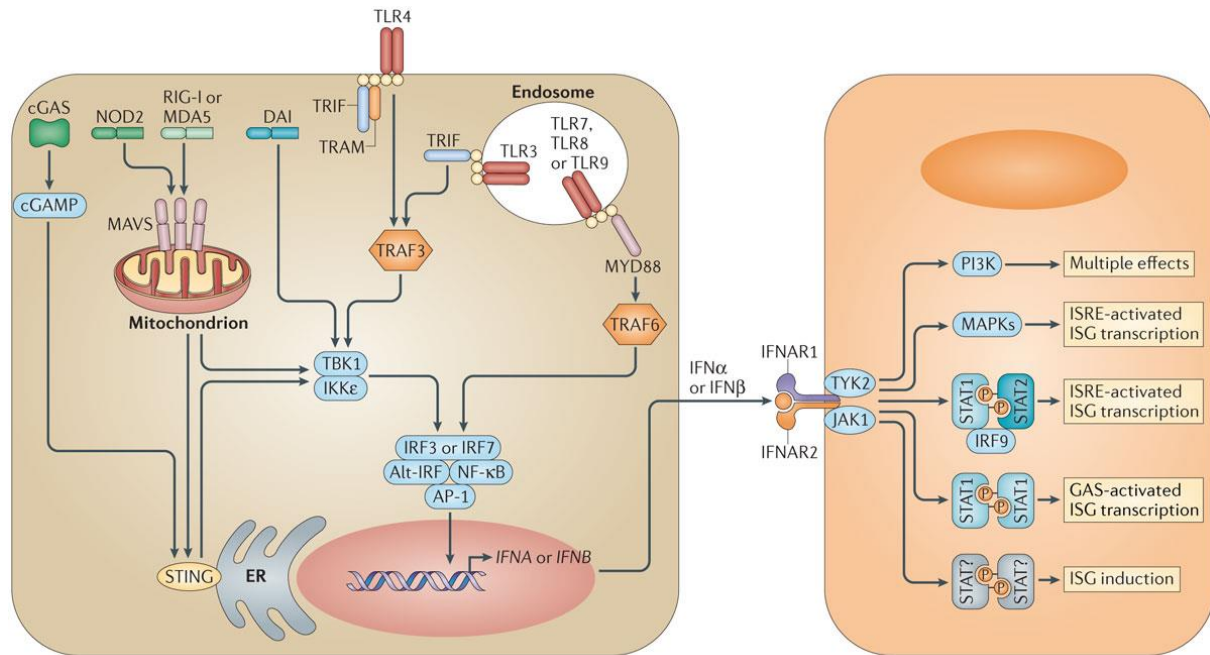
Figure 2: Type I interferons upstream and downstream pathways. The left cell: PRRs such as cGAS, NOD2, RIG-I, MDA5, and TLR receptors are shown. Downstream adaptor proteins such as STING, MAVS, and MYD88 are depicted. Transcription factors such as IRF3, IRF7, and NF-κB activate interferon production (IFNα and IFNβ). The right cell: IFN receptors are shown (IFNAR1 and IFNAR2). IFN-I induced activation of different processes are described. Figure from McNab et al[24].

1.3 The cGAS-STING Pathway

One of the innate immune signalling pathways under intense research in recent years is the cGAS-STING pathway. Its main role is to detect cytosolic dsDNA and activate a signalling cascade, which results in the production of type I IFNs (Figure 3). The cGAS-STING pathway is defined as an innate immune pathway defending us against viral and bacterial infections. However, the pathway itself was found to function in many other processes as well. cGAS-STING signalling occurs in different cell types and molecular environments, in which it leads the cell to many distinct outcomes such as autophagy, apoptosis and senescence. Apart from viral and bacterial threats, cGAS gained a crucial role for cytosolic self-DNA detection in the context of cancer immunity and aging.
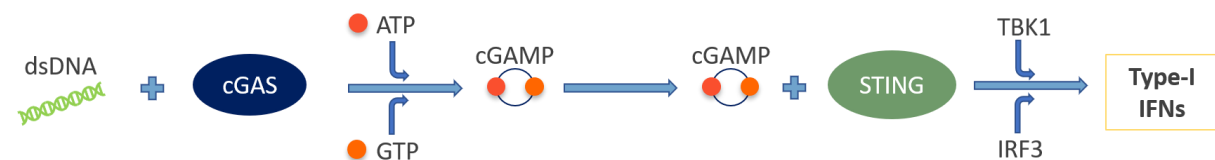
Figure 3: A simple depiction of the cGAS-STING Pathway. cGAS detects and binds double-stranded DNA (dsDNA). One ATP and GTP is catalysed by cGAS to produce cyclic- guanosine monophosphate-adenosine monophosphate (cGAMP). STING binds cGAMP. TBK1 and IRF3 are recruited by STING leading to type I IFN production.

Introduction

1.3.1 The Mechanism of the cGAS-STING Pathway

Despite its versatility in outcome, the mechanism of the cGAS-STING pathway can be best described by looking at its most known and well explained signalling cascade leading to IRF3 activation. The pathway commences with the detection of cytosolic dsDNA by cGAS and the formation of a cyclic signalling molecule cGAMP. The N-terminus of cGAS anchors the enzyme to the plasma membrane, keeping it away from nuclear vicinity[25]. The crystal structure of cGAS bound to DNA reveals a conserved binding region with histidine and cysteine residues coordinating a zinc ion[26,27]. When cGAS binds to dsDNA it forms a complex in which the zinc domain binds to the phosphate backbone of the DNA[28,29]. Compared to mouse cGAS, human cGAS contains two substitutions (K187N and L195R) that increase the selectivity for longer DNA strands[30]. Therefore, human cGAS preferably binds to longer chains of DNA and tends to coordinate with more cGAS dimers, forming a DNA-protein ladder[31]. This ladder formation and the preference for longer dsDNA strands leads to higher amounts of produced cGAMP, resulting in a more intense signal. Furthermore, when cGAS binds to DNA a phase separation occurs due to the positively charged N-terminus of cGAS and free zinc ions, promoting cGAMP production[32]. 2',3'-cGAMP (referred to as cGAMP or natural cGAMP) is produced in a two-step reaction from ATP and GTP[33–35] (Figure 4). The produced cGAMP bears a 2'-5' and a 3'-5' bond, giving it its unique structure and allowing it to bind to human STING with much higher affinity compared to other bacterial cyclic dinucleotides (CDNs)[36,37].
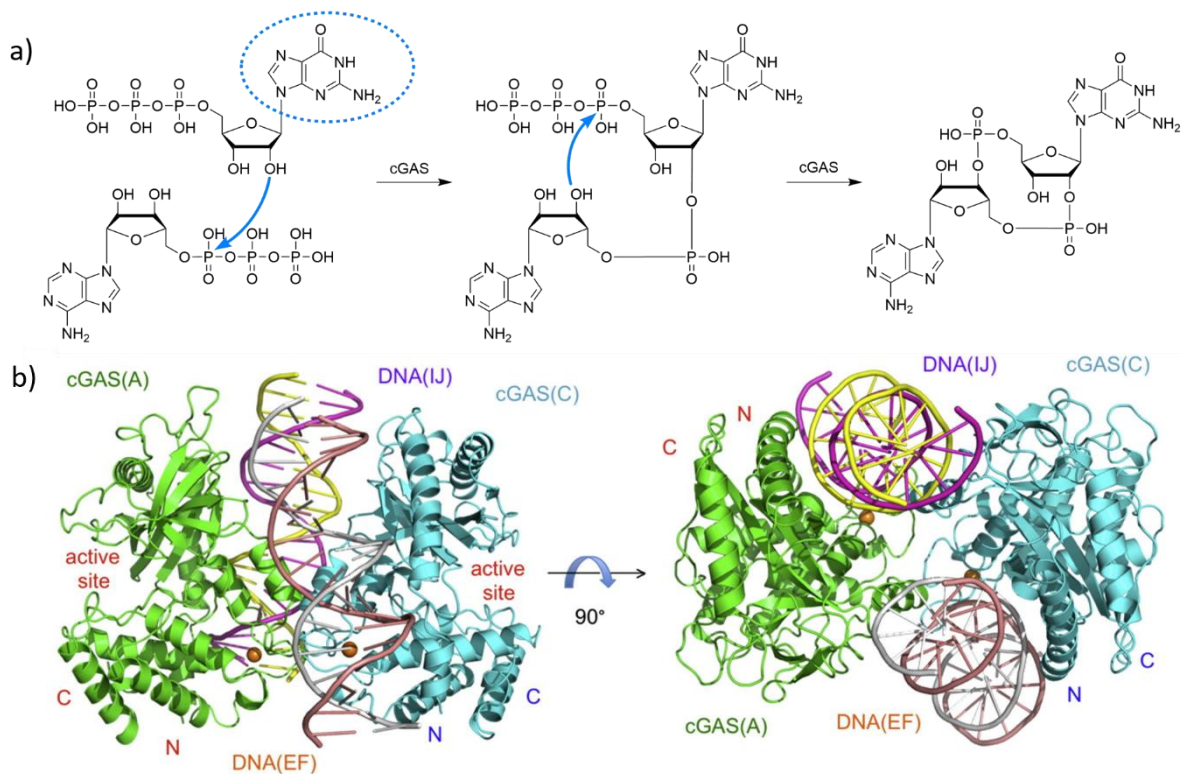
Figure 4: Synthesis of cGAMP and cGAS bound DNA. a) Two step reaction of cGAMP synthesis. 2'OH of GTP attacks ATP releasing a pyrophosphate and forming a linear dinucleotide pppGp(2'-5')A. In the second step, 3'OH of ATP attacks the phosphate of GTP, releasing another pyrophosphate, resulting in 2',3'-cGAMP. b) Crystal structure of DNA bound cGAS in a 2:2 ratio. From Li *et al* [28].

4

As a second messenger to the cGAS-STING pathway, cGAMP travels through the cytosol and binds to the adaptor protein STING, which is located on the endoplasmic reticulum (ER) membrane[38]. Inactive STING is settled in the ER as dimers. The N-terminus of STING spans the ER membrane four times, whereas the ligand binding domain (LBD) on the C-terminus pointing towards the cytosol forms a V-shape with another LBD of a neighbouring STING[39–41]. The C-terminus tail (CTT) resides also in the cytosol. When cGAMP binds, the CTTs function as a lid and close the opening of the V-shaped LBD dimer to trap cGAMP[40]. Between the ER-luminal and the cytosolic part of STING resides a connector helix. After cGAMP binds and the lid closes, the cytosolic part of the dimers undergo a 90° rotational shift, allowing STING dimers to interact with one-another via the connector helices and promoting oligomerisation[42,43]. This STING oligomerisation is the initiator of the transport of STING from ER to the Golgi apparatus.
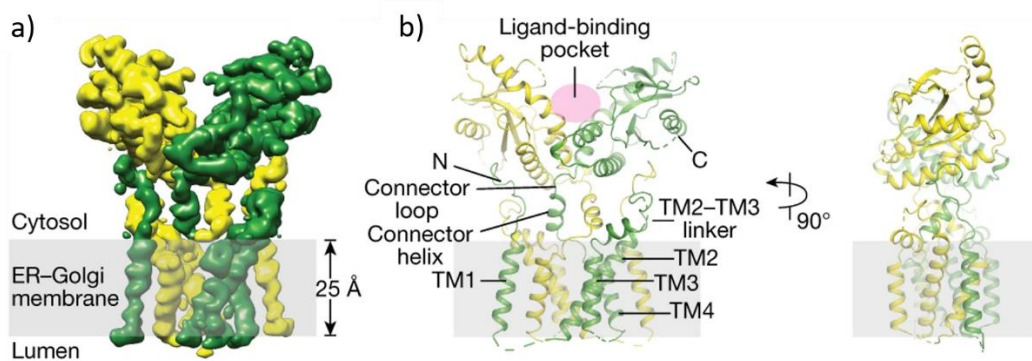
Figure 5: Structure of human STING upon ligand binding. a) Two STING monomers, shown in yellow and green, form a dimer. Membrane and cytosolic regions are annotated. b) The ligand binding pocket is indicated in the STING dimer (left). The 90° turn of the connector helices upon ligand binding is shown (right). Figure from Shang *et al* [42].

After STING is activated by cGAMP it moves through the endoplasmic-reticulum-Golgi intermediate compartment (ERGIC) and arrives at the Golgi. The transport to the Golgi relies on coat protein complex II (COPII) vesicles and ADP-ribosylation factor (ARF) GTPases[44]. During the transport to the Golgi, TBK1 is recruited. These bind to the TBK1-binding motif on the CTT of STING (purple CTT region in Figure 6)[45,46]. Additionally at the Golgi state, palmitoylation of STING at Cys88 and Cys91 is required for and linked to TBK1 binding[47,48]. The recruited TBK1s undergo trans-phosphorylation (Step 1 on Figure 6)[49]. The phosphorylated TBK1 (pTBK1) phosphorylates a neighbouring STING-CTT on its Ser366, which serves as a docking site for the transcription regulator IRF3 (Step 2 on Figure 6)[50]. IRF3 is then recruited and binds to the CTT (green CTT region in Figure 6). There, it is phosphorylated by pTBK1 forming pIRF3 (Step 3 on Figure 6)[50]. Two pIRF3s dimerise to become transcriptionally active. These dimers travel to the nucleus to induce type I IFN production. STING residing in the Golgi is recycled and carried back to the ER by the mediation of coat protein complex I (COPI). Alternatively, it can be transported to an endolysosome to be degraded[51].
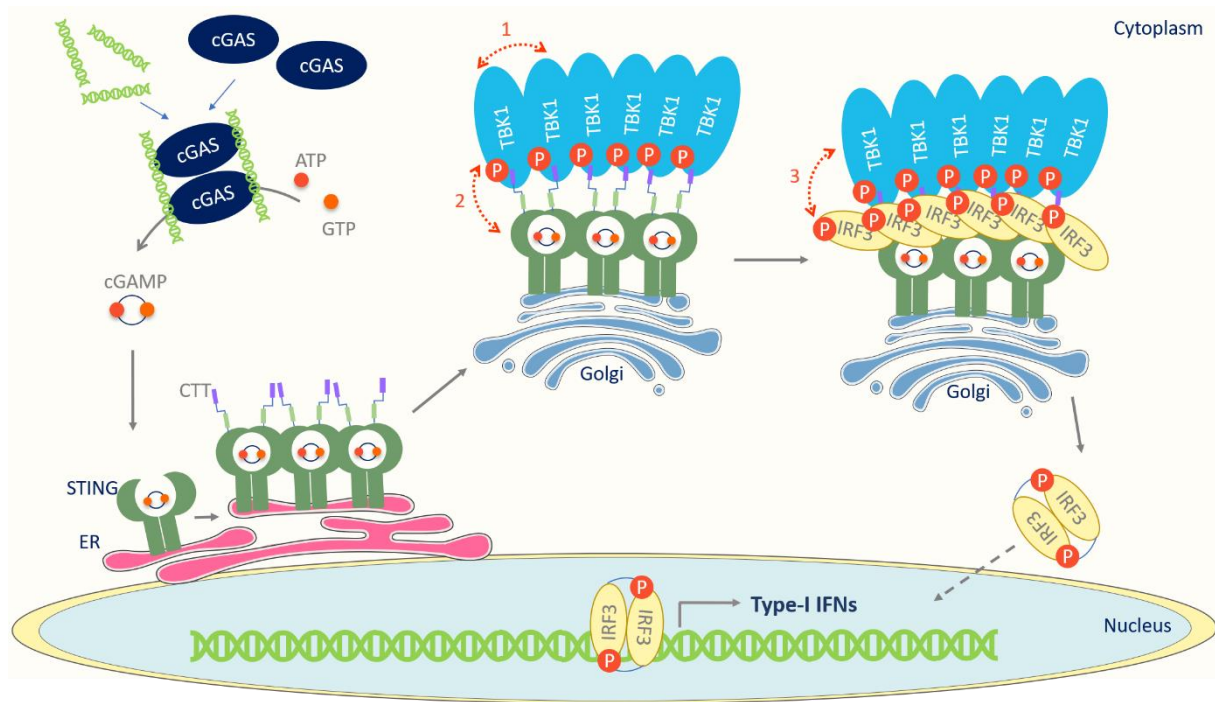
Figure 6: The cGAS-STING Pathway. cGAS binds dsDNA, forming a DNA ladder. ATP and GTP is converted to 2',3'-cGAMP by cGAS which binds STING residing in the endoplasmic reticulum (ER). Upon binding, the lid of STING closes with the C-terminal (CTT) protruding out, purple domain=TBK1 docking site, green domain=IRF3 docking site. Closed STING travels to the Golgi via ERGIC (not shown). TBK1 binds, self-phosphorylates (1) and phosphorylates STING (2). IRF3 is recruited and phosphorylated by TBK1 (3), forming dimers. Phosphorylated IRF3 dimers travel to the nucleus to activate transcription. Phosphorylation shown in circular red "P" and red dotted arrows.

The activation of IRF3 dimers is the best understood process of the cGAS-STING pathway. However, it is not only IRF3 dimers which can be transcriptionally activated by cGAS-STING. NF-κB can also become activated by STING, both in a TBK1 dependent and independent manner (Figure 7). In fact, in lower organisms, a STING-CTT independent activation of NF-κB is the primary transcriptional regulator[52]. In mammals, TBK1 can activate but is not necessarily required for NF-κB activation[53,54]. TBK1 can also be replaced by IKKε in certain contexts and cell types (Figure 7)[55]. Interestingly, the non-canonical NF-κB pathway can also be activated by STING and serve as a negative regulator to STING[56,57]. Upon viral infection, STING also activates STAT6 through TBK1, which in turn induces an antiviral response on the transcriptional level (Figure 7)[58].
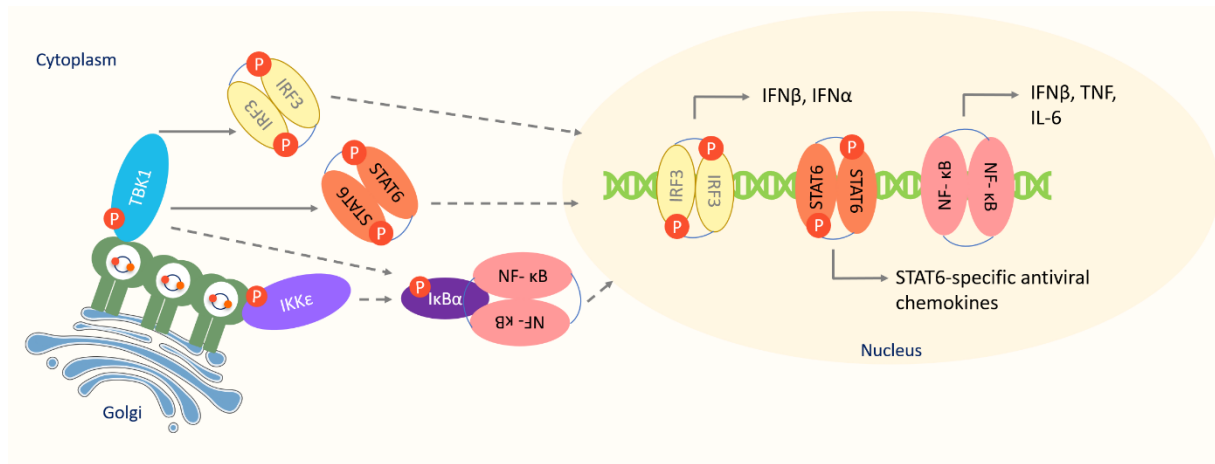
Figure 7: STING induced transcriptions. STING activates different transcription factors. From top to bottom and left to right: phosphorylated IRF3 dimers inducing a type I IFN response, phosphorylated STAT6 dimers inducing an anti-viral response, NF-κB activated by TBK1 or IKKε inducing a response by various cytokines.

1.4 Stimuli and Specific Responses of the cGAS-STING Pathway

The cGAS-STING pathway is activated by either exogenous-pathogen associated DNA invasion or endogenous DNA which has escaped membrane bound compartments such as mitochondria, micronuclei or the nucleus. Other types of cyclic dinucleotides (CDNs) released from a bacterial infection can also stimulate STING directly. The source of cytosolic DNA as well as the cell type and molecular environment determine the response of the cGAS-STING pathway along the transcriptionally activated gene sets.
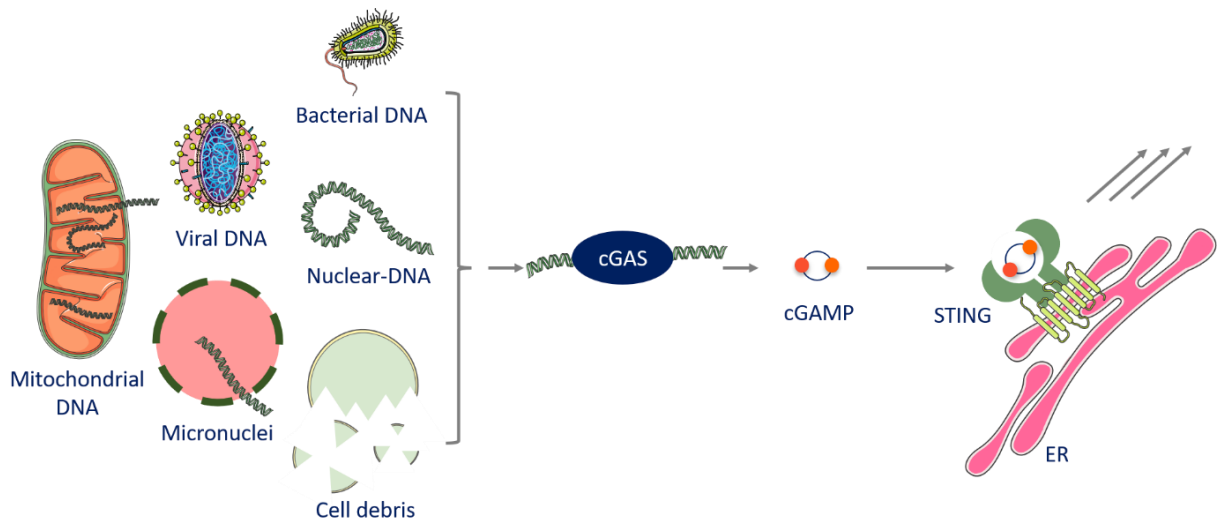
Figure 8: Sources of DNA Initiating the cGAS-STING Pathway.

1.4.1 Extrinsic Stimuli

dsDNA released by viral as well as bacterial infection is detected by cGAS either in the cytosol or in the nucleus. cGAS protects the cell from infection of many viruses including herpes simplex I and vaccinia virus[59]. Retroviral infections such as HIV are also recognised by cGAS, but in the nucleus instead of the cytoplasm where most RNA viruses replicate their genetic material[60,61]. The defence provided by cGAS against retroviruses is a more complex process

involving various host proteins and ribonucleoproteins. Furthermore, the ability of cGAS to detect DNA:RNA hybrids suggests alternative mechanisms of RNA virus detection[62]. Upon viral infection STAT6 is phosphorylated by TBK1 following STING activation and induces the transcription of antiviral cytokines and chemokines[58].

Intracellular bacteria also release their genetic material inside the cell and preferably replicate in the cytosol. Besides bacterial DNA, bacterial CDNs are also released to the host cytosol. The cGAS-STING pathway can be activated by both stimuli. Among the most important intracellular bacteria which induce IFN response through cGAS-STING are *Mycobacterium tuberculosis* and *Listeria monocytogenes*[63,64]. After recognition of *M. tuberculosis* in the cell, STING activates an autophagy response besides IFN production[65]. *L. monocytogenes* activates STING also with its c-di-AMP besides its genetic material[66].

1.4.2 Intrinsic Stimuli

A crucial stimulus of the cGAS-STING pathway is self-dsDNA. There are several ways of self-dsDNA to gain access into the cytosol. Upon increased cell death in the environment, cell debris and exosomes containing dsDNA can be picked up from neighbouring cells. Within the cell, DNA can leak through the membranes of mitochondria, nucleus and micronuclei.

Mitochondrial DNA (mtDNA) may gain access to the cytosol via apoptosis. During apoptosis, mitochondrial outer membrane permeabilization (MOMP) causes the pores on the outer membrane of mitochondria to widen (Figure 9). It also allows the inner membrane of the mitochondria to extrude and permeabilise, thus releasing cytochrome *c* as well as mtDNA to the cytosol. Cytochrome *c* activates caspases, which besides their apoptotic signalling also inhibit cGAS from detecting mtDNA[67]. However, upon mitochondrial stress mtDNA can be released without cytochrome *c*, leading to a caspase-independent inflammation mediated through cGAS-STING signalling[68]. Also upon mitochondrial stress, mtDNA binding protein TFAM (transcription factor A, mitochondrial) is downregulated, which results in formation of poorly packaged mtDNA prone to leak into the cytosol[69]. Bacterial and viral infections on the other hand, can also promote mtDNA release (Figure 9)[70–73]. These processes enhance innate immune signalling of cGAS-STING by mtDNA.
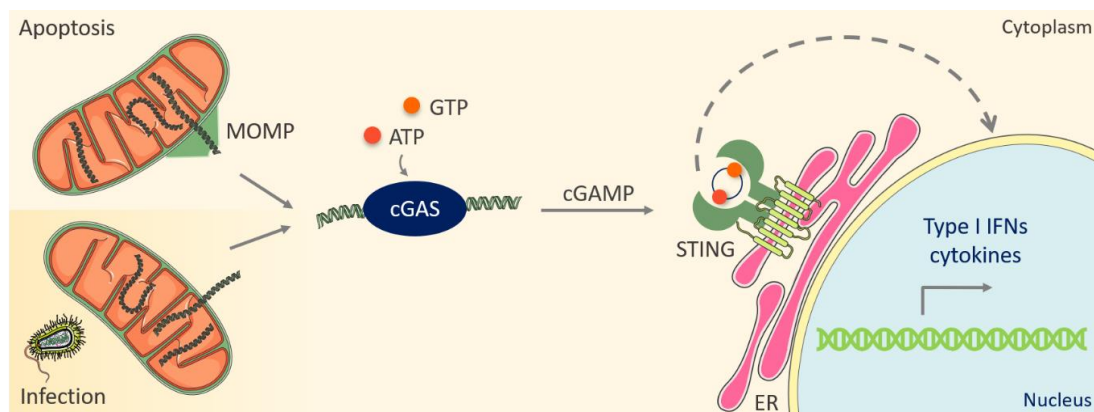
Figure 9: mtDNA release inducing cGAS-STING pathway. Apoptosis induced mtDNA release via Mitochondrial Outer Membrane Permeabilisation (MOMP) and infection is depicted.

Introduction

There are many ways in which genomic DNA (gDNA) can leak into the cytosol where it interacts with cGAS. Replicative stress caused by unrepaired DNA breaks induced by malfunctioning enzymes, oncogenes, or external factors such as UV irradiation may lead to error-prone segregation allowing chromosomal fragments to leak or form micronuclei (Figure 10)[74]. On the other hand, certain molecular pathways may destabilise the nuclear envelope directly, allowing DNA release to the cytosol[75]. The mechanisms of how gDNA is released to the cytosol and their downstream effects will be described in the following.

Many errors occur during DNA replication which are repaired by finely tuned mechanisms in the nucleus. Upon malfunctioning of a repair enzyme, double- or single-stranded DNA breaks remain present during replication resulting in pieces of the genetic material to be cleaved and released. For example, SAMHD1 (sterile alpha motif and HD domain-containing protein 1), a dNTPase known for protecting against viral infections, helps with the restart of the replication when the replication fork is stalled. In SAMHD1-deficient cells, gDNA accumulates in the cytosol activating cGAS-STING[76]. This process causes a continuous inflammatory phenotype. SAMHD1 mutations are for instance linked to the auto-inflammatory disease Aicardi-Goutières syndrome[77].

Unrepaired DNA lesions can potentially cause micronuclei formation. Micronuclei consist of genetic material wrapped in their own relatively unstable nuclear envelope. After a while their nuclear envelope collapse and the genetic material is released[78]. Micronuclei derived dsDNA is detected by cGAS providing an alarm system by inducing IFN-I signalling (Figure 10)[79]. Chromosomal instabilities (CIN) and mis-segregation cause micronuclei formation and are strongly linked to tumours. The activation of cGAS-STING in cancers is further described in section 1.7.
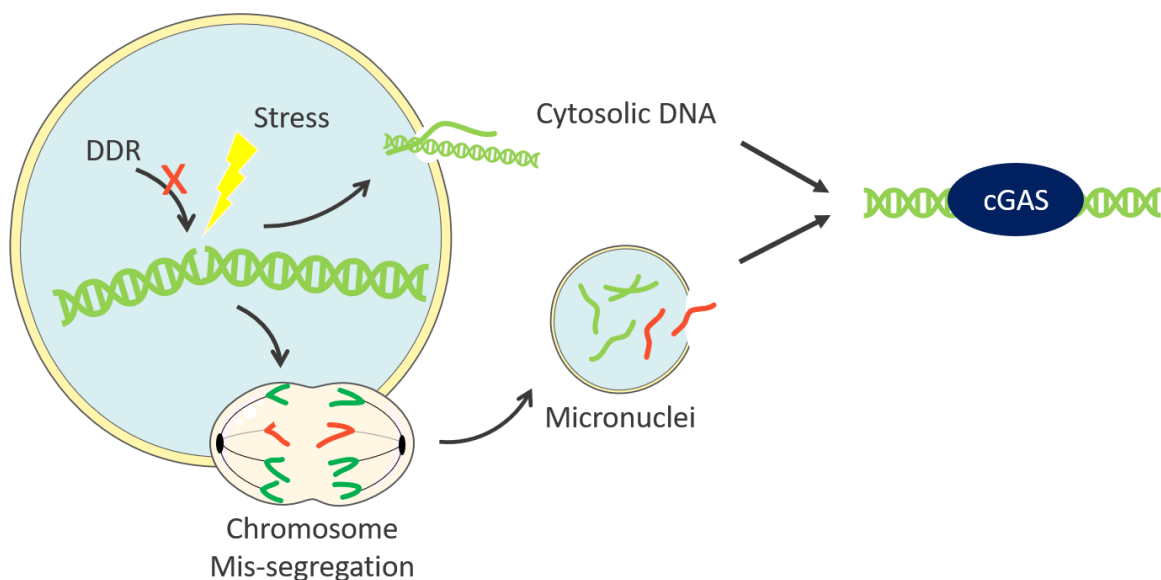
Figure 10: DNA damage leading to micronuclei formation and cGAS-STING activation. Stress and unfunctional DNA Damage Response (DDR) leads to chromosome mis-segregation and micronuclei formation, as well as DNA leakage into the cytosol. Upon micronuclei envelope rupture, more DNA is released, activating the cGAS-STING pathway.

Introduction

Senescence

Senescence is a cell cycle arrest, which allows metabolic activity but prevents the cell from replicating[80]. Cells entering senescence express a number of paracrine molecules which lead the cell into the senescence-associated secretory phenotype (SASP)[81]. The SASP elements consist of various molecules and enzymes including inflammatory cytokines, chemokines, growth factors, and proteases[81]. These molecules have the potential to alter the tissue environment and induce suppression or promotion of tumours[82]. Senescence mainly occurs in an age-dependent manner and is therefore linked to age-related diseases[83–85].

In cells which senesce, the nuclear envelope destabilises by the downregulation of the nuclear membrane component Lamin B1, allowing chromatin to protrude into the cytosol[75]. Cytosolic chromatin fragments (CCFs) thus mount up and activate cGAS[86,87]. cGAS is then stimulated continuously, allowing IRF3 and NF-κB induction leading to inflammatory responses by the expression of SASP elements[87]. DNases are downregulated in senescent cells, which allow cytosolic DNA to persist[88]. The main contribution of cGAS-STING to senescence is to promote the production of SASP elements after sensing cytosolic DNA[87,89].

Cells which are in the state of cell cycle arrest can be eliminated through pro-inflammatory SASP components which recruit immune cells[90–92]. This applies when the SASP is short-lived. However, longer lasting SASP results in increased genetic instabilities leading to inflammation-related disorders, tumour formation, and aging (Figure 11)[89]. The stimulant, cell type, and age are factors to determine the relationship between senescence, its duration and tumour development[93]. The importance of cGAS-STING regulation in senescent cells and therapeutic approaches will be described in section 1.8.
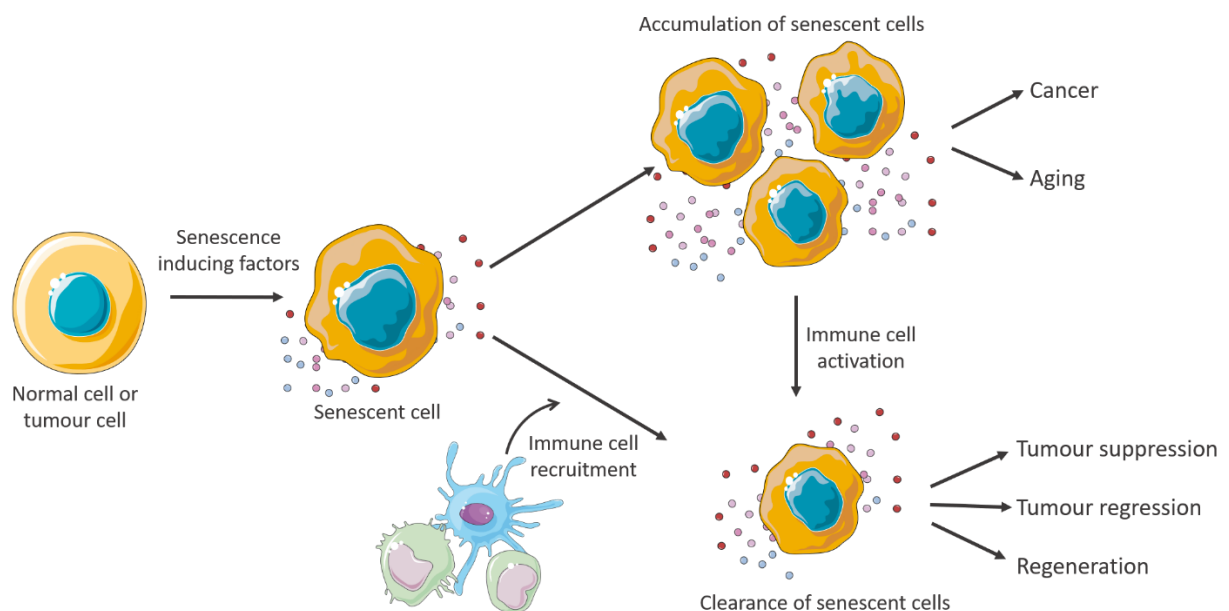
Figure 11: Long-term and short-term senescence and its outcomes. Circular molecules represent the SASP elements.

1.5 Regulation of the cGAS-STING Pathway

The cGAS-STING pathway is regulated at each step of the signalling cascade (Figure 12). DNA in the cytosol is usually degraded by 3-prime repair exonuclease I (TREX-I or DNase III) before it is sensed by cGAS[94,95]. Activated cGAS is attenuated by the Akt protein kinase which prevents an over-stimulation of cGAS upon recognition of self-DNA and viral DNA[96]. cGAMP can be degraded to decrease the signalling strength and spread of the signal. Ectonucleotide Pyrophosphatase/Phosphodiesterase 1 (ENPP1) is the so far known main degrading enzyme of cGAMP[97,98]. Acting only in the extracellular space, it cleaves phosphodiester and pyrophosphate bonds of nucleotides, thus expanding its site of action. Another known group of enzymes degrading cGAMP are poxins from the poxvirus family[99]. Upon a poxvirus infection, it is believed that poxins function mainly to prevent the spread of cGAMP to other cells by newly packaged viruses, instead of preventing an IFN signal in the currently transfected cell.

cGAMP can be released to the exterior of the cell and propagate the signal. One way of transfer to bystander cells is through gap junctions made of connexin, directly connecting the cytosols of two cells[100]. This way, upon a viral infection, the neighbouring cells can also activate their immune pathways. Gap junctions may also connect two different cells types, allowing expanded reach of the cGAMP signalling[101]. Also in viral infections, the newly packaged virus can contain cGAMP, which on the next cell invasion can be released directly to the cytosol of the new cell[102]. To date, several cGAMP transporters are identified. Two folate channel receptors SLC19A1, SLC46A2, and LRRC8 which is a heteromeric volume-regulated anion channel are examples discovered so far. These are expressed in different levels in different cell types[103–105].

STING is retained in the ER by Ca^{2+} sensor Stromal Interaction Molecule (STIM1) which associates with STING in steady-state conditions[106]. The transfer of STING from ER to Golgi is tightly regulated by several proteins. STING ER Exit Protein (STEEP) is essential for STING to detach from the ER[107]. On the other hand, STING trafficking from the ER can be inhibited by Nucleotide-binding by Leucine-rich Repeat Containing protein 3 (NLRC3)[108]. STING signalling is attenuated by disassembly of the oligomer and by the degradation of STING after it exits the ER. STING needs to be trafficked to endolysosomes for lysosomal degradation[109]. Alternatively, ubiquitination of STING by the E3 ligase RNF5 also leads to its degradation[110].
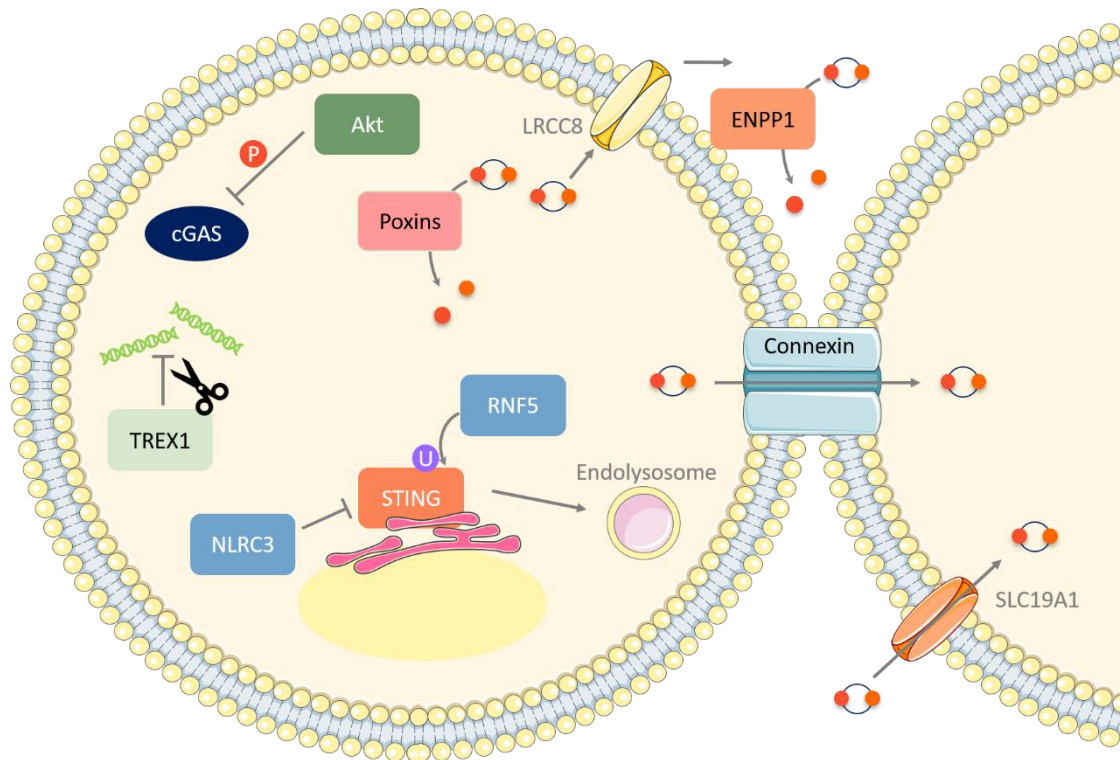
Figure 12: cGAS-STING signal attenuation, cGAMP degradation and transfer.

1.6 cGAS-STING and Autophagy

Another downstream event of the cGAS-STING pathway is autophagy[44]. For its direct activation towards autophagosome formation, cGAMP bound STING is only required to be moved to the ERGIC where it interacts with ARF GTPases[44,111]. Association with TBK1 is not necessary. The STING containing ERGIC complex leads to LC3 lipidation, which initiates autophagosome formation[44]. Autophagosome formation was suggested to be the earliest role of cGAS-STING. It allows the removal of viruses and abnormal proteins after an infection (Figure 13)[44]. STING-induced autophagy plays an essential role as an anti-tumour mechanism as well. As soon as DNA instabilities are detected by cGAS, a cell-death autophagy response is activated before the cell can replicate[112]. If the autophagy pathway is escaped by the cell, it begins to develop an unstable tumorigenic character. Lastly, autophagy also regulates STING signalling by directing both STING and cytosolic DNA towards lysosomal degradation (Figure 13)[44,46].
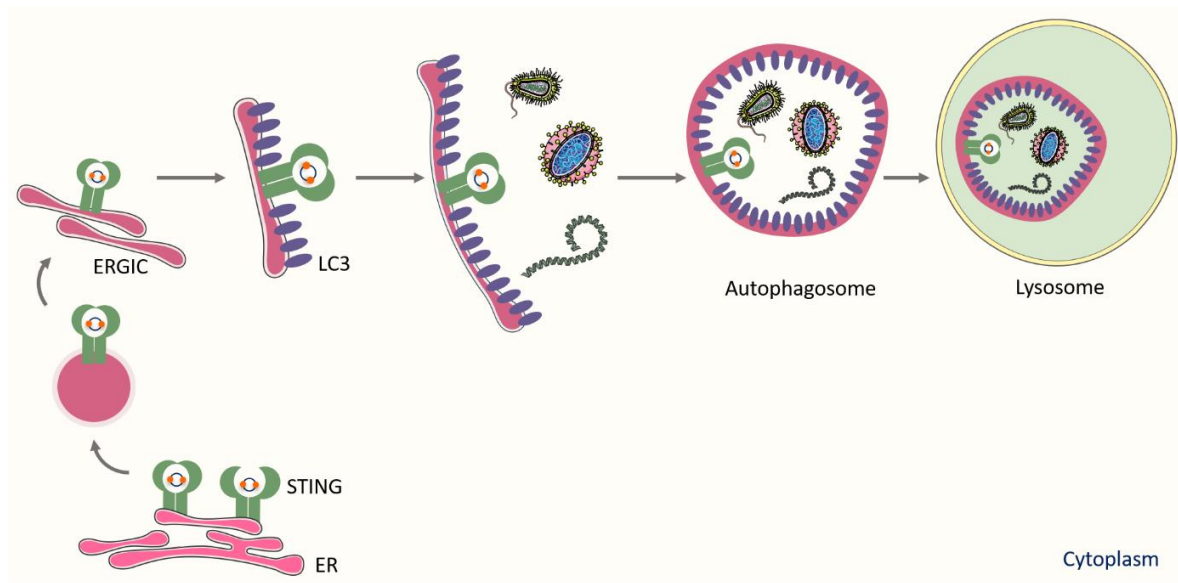
Figure 13: STING and Autophagy. After STING activation by cGAMP, autophagy from the ERGIC stage is shown. LC3 lipidation (purple) leads to autophagosome formation. Along the STING protein and cGAMP, DNA, bacteria, and viruses are carried to the lysosomal degradation.

1.7 Cancer Immunity Cycle and cGAS-STING in Cancer

When tumours start to form, unnatural and tumour specific molecules are produced, named neoantigens. These are released and captured by antigen presenting cells, thus activating T cells. These T cells recognise the tumour cells which present the specific neoantigen and attack the tumour. The destruction of cancerous cells results in release of more antigens. Hence, more T cells are activated and drawn to the area, resulting in the eradication of the tumour. This process is called the cancer immunity cycle and is regulated heavily by cGAS-STING signalling (Figure 14)[113,114].
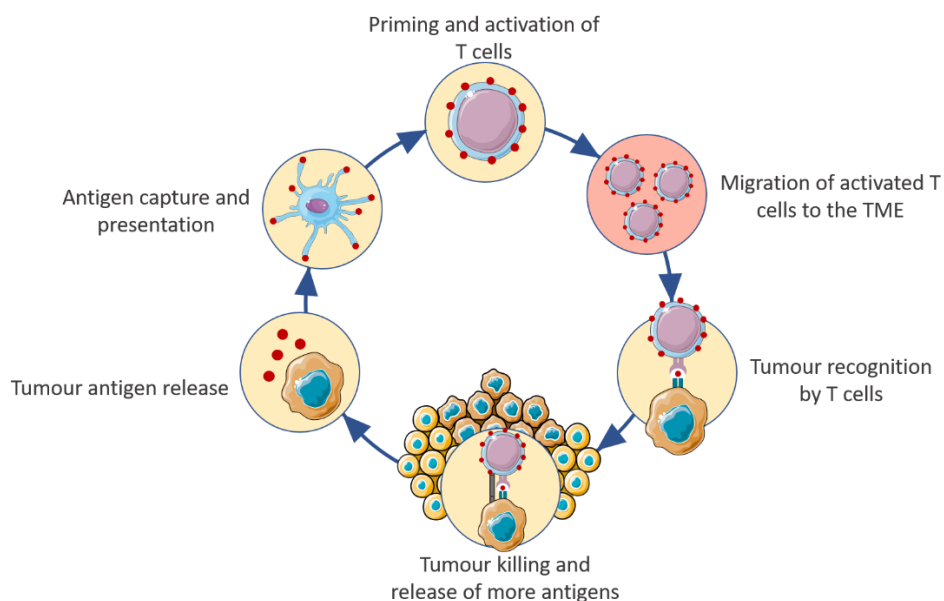
Figure 14: Cancer Immunity Cycle.

Introduction

CD8α+ dendritic cells (DCs) mature through IFN-I production and promote antitumour T cell responses[115]. DCs prime and activate CD8+ T cells through cross-presentation of tumoral antigens (Figure 15)[116]. Therefore, the IFN-I production in DCs is crucial for the anti-cancer response by T cells[117]. The STING pathway is the essential innate immune pathway responsible for both DC maturation and T cell activation[118]. In the cytosol of DCs, tumour-derived DNA is found which activates IFN-I production through the cGAS-STING pathway[119]. This DNA is responsible for not only IFN-I production, but also expression of costimulatory molecules, cytokines, and chemokines[118]. It is yet to be discovered how and in which cancers tumour-derived DNA ends up in the cytosol of DCs. cGAMP as a second messenger is however, already known to be shuttled out from tumour cells as an intercellular messenger to the tumour microenvironment (TME)[120]. When cGAMP is applied to DCs, it is taken up and enhances antitumour activity[121]. This mechanism in the TME allows DCs to mature and facilitates CD8+ T cell maturation and infiltration[122].
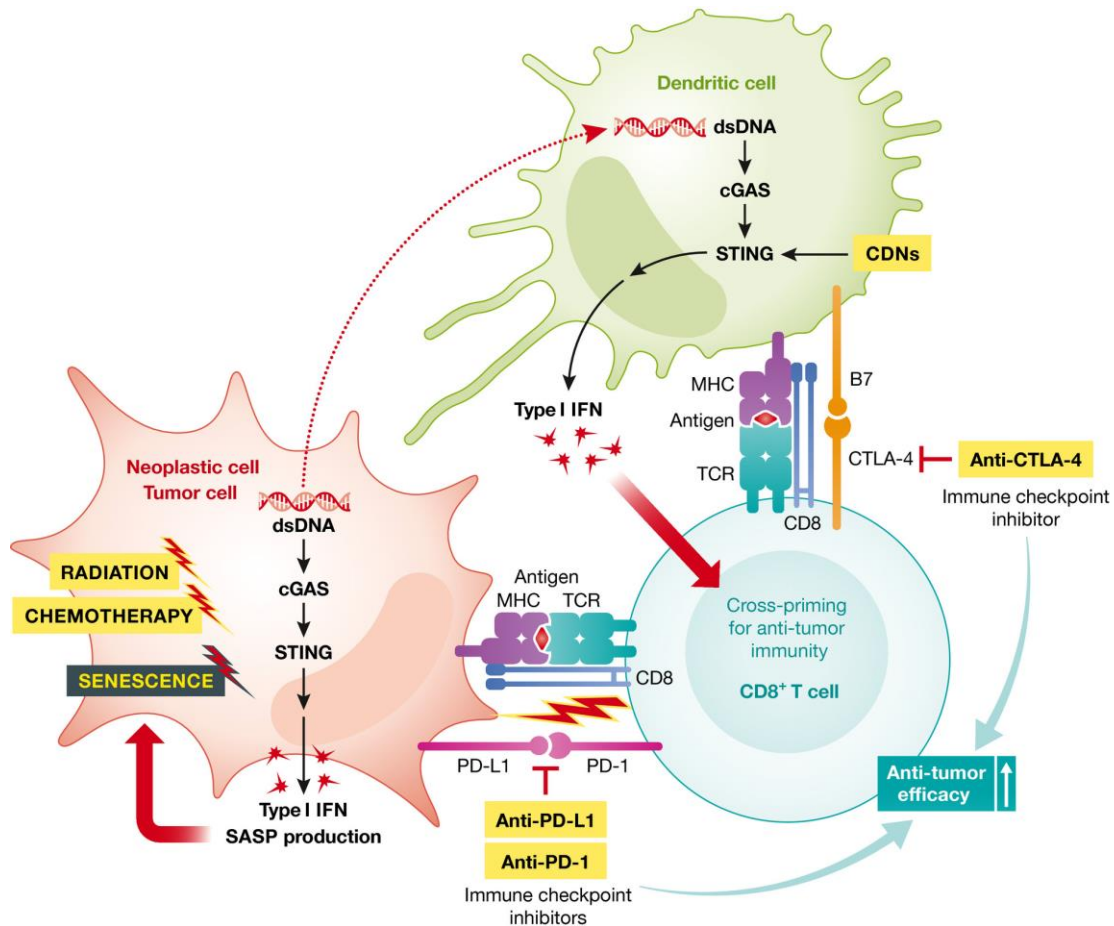
Figure 15: Role of cGAS-STING in tumours and dendritic cells for tumour suppression. Radiation, chemotherapy, and senescence lead to DNA leakage into the cytosol. Cytosolic DNA in tumour cell activates the cGAS-STING pathway, thus induces the production of type I IFNs and SASP elements. Tumour-derived DNA is sensed by dendritic cells in which it activates the cGAS-STING pathway. The production of type I IFNs leads to maturation and cross-priming, thus activation of CD8+ T cells. The tumour is recognised and attacked by activated CD8+ T cells. Immune checkpoint pathways PD-L1/PD-1 and B7/CTLA-4 negatively regulate CD8+ T cell activity. Checkpoint inhibitors acting on PD-L1/PD-1 and CTLA-4 are shown. Figure from *Khoo et al* [123].

Besides the cancer immunity cycle the cGAS-STING pathway can be activated in tumour cells and immune cells of both the innate and adaptive immune system. In tumour cells, cGAS-STING signalling results in immune recognition of tumours through inflammation[124]. Expression of pro-inflammatory cytokines and other SASP elements are also induced. The transcription profile of the SASP elements depends on the stimuli, cell type and context as mentioned earlier. Both the activated innate immune cells or adaptive immune cells of the cancer immunity cycle can clear the tumour cells. Differentiation, maturation and migration of dendritic cells and macrophages is induced by type I IFN production[125–128]. As a part of the innate immune cell subset, natural killer (NK) cells are an abundant cytotoxic lymphocyte ready for antitumour activity. The tumour-derived cGAMP indirectly activates NK cells despite the lack of intrinsic STING activation[129]. Hence, the cGAS-STING pathway reflects a more aggressive defence mechanism on cancer cells through NK cells.

cGAMP in the TME can be taken up by immune cells directly from the extracellular environment through cGAMP transporters. SLC19A1, also known as Reduced Folate Carrier 1 (RFC1), is the first identified cGAMP transporter, greatly responsible in monocytes to respond to extracellular cGAMP[103,130]. In THP-1 monocytes, SLC19A1 is responsible for 50% of the uptake of extracellular cGAMP *in vitro*.[103] Other identified cGAMP transporters are the LRRC8A/E heteromeric channels, which are volume-regulated anion channels (VRAC)[105]. Compared to SLC19A1 transporters, which are expressed in monocytes, LRRC8A/E are expressed in vasculature cell lineages and endothelial cells[131]. More recently, the SLC46A2, another transporter of cGAMP was discovered and it was argued that in both monocytes and macrophages, SLC46A2 is the main cGAMP importer[104]. Not much is yet known regarding the uptake of cGAMP by DCs.

The cGAS-STING pathway is already utilised for anti-cancer therapies. One of the most widely used therapies is radiotherapy[132]. It was found later that the cGAS-STING pathway is playing two roles for radiotherapy to function. First, the damaged DNA is sensed by cGAS, inducing production of IFNs in the tumour[74]. Second, the detection of tumour derived DNA or cGAMP in surrounding immune cells, such as DCs, is leading to their activation[118,119,133]. In certain chemotherapy drugs the effect is observed directly dependent on cGAS-STING activation[134,135]. Among those drugs are topoisomerase inhibitors, checkpoint kinase inhibitors and several DNA crosslinking agents[135–137]. These findings raised the question if the cGAS-STING pathway could be utilised for cancer therapies in a more direct manner. When natural as well as synthetically modified cGAMP was injected into tumours, a regression of the tumour was observed through IFN production in several cancers[138–140]. The cGAS-STING pathway activity is observed in various stages of cancer and the cancer immunity cycle, which may provide for immune enhancement at different stages.

High levels of cGAS-STING activation can also lead the cells to pro-tumorigenic cascades. In cancer cells, micronuclei form frequently due to increased chromosomal instabilities (CIN). Upon rupture of these micronuclei, DNA is released and activates the cGAS-STING pathway[79,141]. When STING is constantly activated in chromosomally unstable cancer cells, it

can drive the cell to the non-canonical NF-κB pathway, thereby activating metastasis inducing genes[56]. The preference of STING inducing metastasis instead of its anti-tumour pathways is linked to the high CIN rate[56]. In cells with high levels of CIN, an increase of ENPP1 is also observed[142]. ENPP1 degrades cGAMP to prevent activation of neighbouring immune cells, as mentioned above[142]. The degradation of cGAMP contributes to the generation of the pro-tumour metabolite adenosine[142,143]. Cells with high levels of CIN therefore escape immune surveillance via high expression levels of ENPP1, allowing the tumour cells to proceed with metastatic activity. Expression of pro-inflammatory genes are linked to the expression of cGAS and STING in several cancers, including pancreatic cancer, melanoma, prostate cancer, and several breast cancers[89]. In cells of the adaptive immune system, high levels of STING signalling causes cell death. STING is stimulated more intensely in T cells compared to macrophages and DCs[144]. The intensity of the signal is increased in T cells, due to the slower degradation rate of STING after signalling. The high stimulation rate of the cGAS-STING cascade thus may lead to apoptosis in T cells[144].

1.8 Aging and the cGAS-STING Pathway

Aging is an event powered by the raise of the basal inflammation level in the body. Cells which have proliferated for a while and become more error-prone or impaired in self-care mechanisms lead to various inflammatory responses also called "inflammaging". Senescence is tightly associated with inflammaging and links cGAS-STING to the event[84]. Aged cells become more susceptible to metabolic alterations induced by therapy, hypoxia or oncogenes leading to age-related cancer[145]. This is mainly due to the high levels of produced SASP elements and a long-lasting senescent state. For example, oncogenic Ras induced senescence makes use of abundant SASP elements to alter the cells in the tissue environment, promoting them towards cancerous behaviour[146]. The structure of the tissue can be loosened, allowing facilitated tumour cell infiltration[82,146]. Besides metastasis, vascularization may be enabled as well[147,148].

Due to its strong connection to senescence, cGAS-STING is proposed as a therapeutic target for age-related diseases[149]. The presence of senescent cells are proved to induce dysfunctions which can be alleviated with senolytic and senomorphic agents[150]. These are developed as anti-cancer drugs as well as for age-related diseases[151–154]. The main objective of senolytics in aged cells is to eliminate senescent cells to inhibit the chronic inflammation, whereas senomorphics target the inhibition of SASP production. Having a pivotal role on SASP production, inhibition of the cGAS-STING signalling could slow down aging and the development of age-related diseases.

1.9 The cGAS-STING Pathway in Disease

Errors in the regulation of cytoplasmic DNA and the cGAS-STING pathway can cause autoimmune diseases (Figure 16). One of the most known examples is the Aicardi-Goutieres Syndrome (AGS), resulting in developmental defects from birth on. Here, several nucleases are deficient such as Trex-I (DNase III) which leads to accumulation of dsDNA in the cytosol, thus causing constant stimulation of the cGAS-STING pathway[155]. Mutations in *DNase2* gene result in loss of DNase II endonuclease activity which was found to reflect heavily on embryonic and post-natal phenotypes in a cGAS-STING-dependent manner[156]. These diseases were proven to be overcome by inhibition of cGAS-STING[95,157].

Another directly STING-related disease is the STING-associated vasculopathy with onset of infancy (SAVI). Gain-of-function mutations on STING cause constitutive STING activation, leading to excess IFN-I signalling[158]. On a later step of the cGAS-STING pathway, is the ER-Golgi transport. Here, when the COPα protein (subunit of COPI) is impaired, transport of STING back to the ER malfunctions. STING signalling continues resulting in COPA syndrome[159–161]. When STING inhibitors are applied, the effects of COPA disease are found to be ceased.

In amyotrophic lateral sclerosis (ALS), TDP-43, a nuclear DNA/RNA binding protein, accumulates in the cytosol and reaches mitochondria, releasing mtDNA[162]. The mtDNA is sensed by cGAS, resulting in IFN-I and NF-κB production. Therefore, inhibition of STING poses a potential ALS remedy[162]. In Parkinson's disease the E3 ubiquitin ligase parkin and ubiquitin kinase PINK1 mutations cause mtDNA release and accumulation in the cytosol as well[163]. cGAS-STING inhibition may therefore help in diseases linked to mitochondrial rupture.
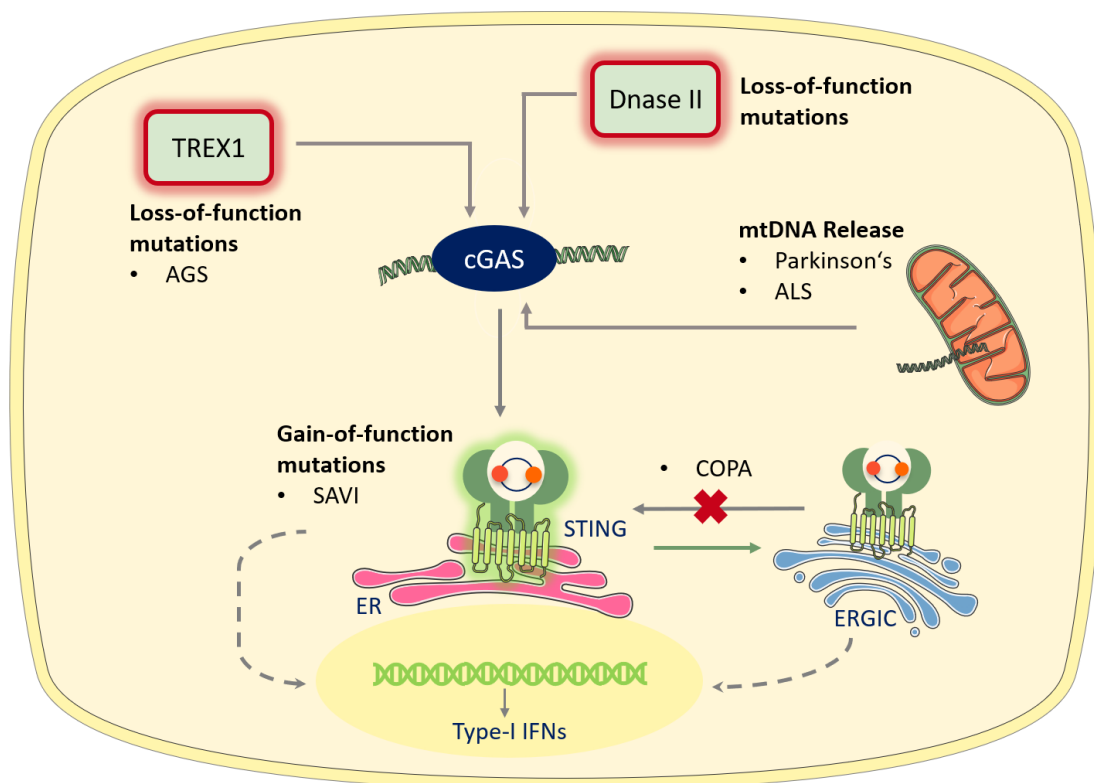
Figure 16: Diseases linked to cGAS-STING overstimulation.

1.10 Activators and inhibitors of STING

Having numerous essential roles in immunology, disease and cancer, the cGAS-STING pathway shows great potential as a target for therapeutic applications. Activators and inhibitors to both cGAS and STING are being developed for this matter. STING is a great target due to its ability to bind several naturally occurring CDNs, as well as synthetically modified CDNs. STING activators and inhibitors will be discussed next.

1.10.1 Activators

In order to activate the cGAS-STING pathway, various activators have been investigated in form of nanovaccines, antibody-drug conjugates, bacterial vectors and ENPP1 inhibitors[164]. However, the most successful activators entering clinical trials are cyclic dinucleotides and non-nucleotide small molecule activators. STING activators are being assessed in combination with existing therapies rather than as monotherapies. The increase of IFN-I production and number of activated T-cells are usually taken as a measure for both innate and adaptive immune strengthening.

The formerly most prominent non-CDN STING agonist DMXAA, was retracted from clinical trials after it failed to improve therapy in phase III clinical trials (Figure 17)[165]. It was discovered that the binding to human STING (hSTING) was significantly reduced compared to mouse STING (mSTING)[166]. Nevertheless, this unsuccessful trial focused the research for a more detailed analysis of ligand-binding mechanism of STING. Structural binding studies revealed that the hSTING lid structure is more porous compared to mSTING, from which DMXAA probably escaped. It was discovered that the agonist needs to be bulkier and have more interactions in the ligand binding domain (LBD), for a STING agonist to bind and stabilise in the hSTING LBD.

One of the earliest known modified CDNs to enter clinical trials is ADU-S100, which contains two adenosine nucleotides linked via a 2'-5' and a 3'-5' phosphorothioatediester linkage (Figure 17). Several trials were pioneered in combination with anti-PD-1 treatments, however despite promising initial results none of them resulted so far in a major success[164]. Another prominent drug in clinical trials is BI-STING (Böhringer-Ingelheim). It is described as a natural STING ligand mimicking agent[167]. The first trials in murine tumours are shown to have dose-dependent anti-tumour activity, increase of cytokines and a resistance for tumour growth[167]. The ongoing clinical trials were designed intratumourally and both as a monotherapy and in combination with an anti-PD-1 monoclonal antibody[168]. Another STING agonist in clinical trials is BMS-986301 (Bristol-Myers Squibb), which was investigated in a CT26 murine tumour model. When BMS-986301 was applied with anti-PD1 it increased tumour regression up to 80%[169].
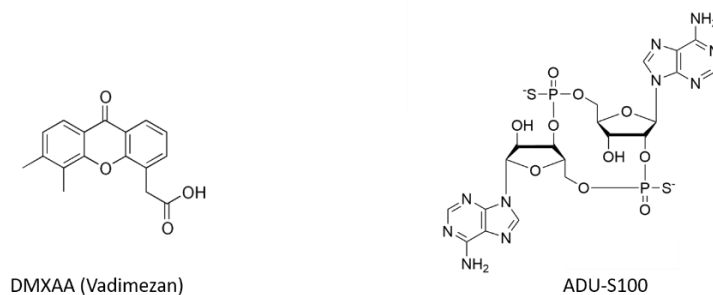
Figure 17: Examples of STING activators.

There are several challenges STING agonist therapies would face. Specifically in high CIN tumours, the activation of STING via an agonist would not be the appropriate therapeutic for the patient. A STING signal attenuating agent would rather eliminate the cancerous phenotype of those cells.

1.10.2 Inhibitors

The inhibition of STING may serve for the diseases such as AGS and SAVI, derived from STING overactivation. The use of STING inhibitors can be extended to several types of cancers as well as metastatic cancers. Moreover, STING inhibitors may provide treatment for aging and senescence, acting as senomorphic drugs. The development of inhibitors so far relies on two mechanisms. One of them is the permanent occupation of the ligand binding domain (LBD) as a STING antagonist, the other one is the inhibition of the palmitoylation process. Tetrahydroisoquinolines are a competitive binder to the C-terminal domain of STING. An identified candidate tested in THP-1 cells shows a successful inhibition of IFNβ[170]. Another successful agonist is Astin C, which binds to the LBD and blocks IRF3 recruitment[171]. In terms of palmitoylation inhibitors, compounds which bind to either Cys88 or Cys91 of STING connector helix are identified. Modified nitrofurans and 3-acylamino indole derivative H-151 were identified to bind Cys91 of STING with a covalent bond, showing inhibitory effects of TBK1 binding[172]. Nitro fatty acid nitrooleic acid was shown to inhibit almost all of the pTBK1 in SAVI patients' fibroblasts by alkylating both Cys88 and Cys91[173]. A more prominent small molecule inhibitor of STING is SN011, which comparatively to H-151 eliminated the overactivity induced by the gain-of-function mutations in SAVI patients[174]. SN011 however, binds to the LBD of STING instead of acting on the palmitoylation sites. The binding affinity to STING is higher compared to cGAMP[174].
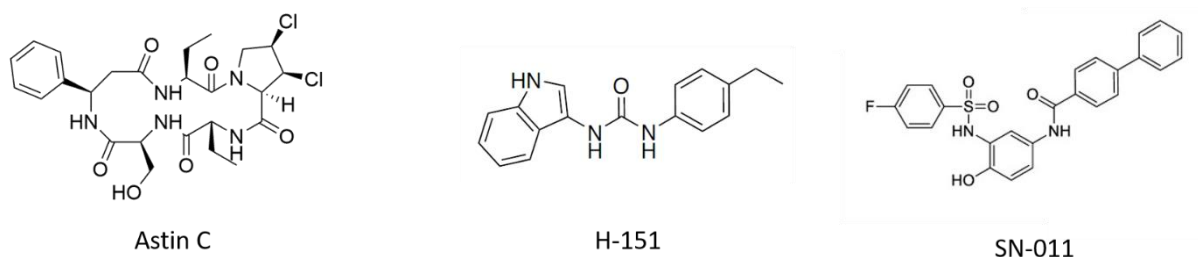
Figure 18: Examples of investigated STING inhibitors.

2 Aim of the Project

The function of the cGAS-STING pathway is to detect cytosolic dsDNA and provide an immune response through type I interferons. This pathway can be activated in many contexts and induces diseases, tumour formation and aging. The cGAS-STING pathway is therefore a promising therapeutic target for immune-linked events and diseases.

In search for more effective cyclic dinucleotides interacting with STING, the group of *Carell* has designed and synthesized agonists and antagonists for STING. The goal of this thesis was to examine the potential of those compounds compared to natural cGAMP using biochemical and cellular assays. In the first part of this thesis, agonists for STING are investigated. 2',3'-dideoxy-cGAMP, 2',3'-dideoxy-cAAMP, and 3',2'-dideoxy-cGAMP are first evaluated in THP-1 monocytic cells. A luciferase reporter system for interferon production is used for this matter. The promising candidates are then exposed to known cGAMP degrading enzymes, ENPP1 and poxins, in order to determine their stability. Enzymatic assays are conducted in a time-dependent manner to follow the degradation rate of the compounds. Furthermore, a prodrug strategy using S-acyl-2-thioethyl (SATE) linkers on the phosphodiester linkage of 2',3'-dideoxy-cAAMP are examined. These compounds are also evaluated to test their biological activity in THP-1 monocytic cells. An alternative prodrug approach using a photocleavable moiety on the ribose alcohols in addition to the SATE linkers is tested.

In the second part of this thesis, an antagonist for STING is evaluated. It was developed by the group of *Carell* using the PROTAC (PRoteolysis TArgeting Chimera) approach with 2',3'-cGAMP as a STING recruiter. THP-1 monocytic cells are exposed to the antagonist to determine its optimal effective time and concentration. The level of STING degradation is observed via western blotting. The potential of all evaluated strategies is discussed.

3 Results and Discussion

Part I: Agonists for STING

3.1 Evaluation of cGAMP Analogues

The development of new drugs targeting the cGAS-STING pathway has become increasingly important in the recent years[175,176]. Small molecules have entered clinical trials and are being investigated in combinatorial immunotherapy approaches. Due to their structural similarities to natural cGAMP, the development of modified cyclic dinucleotides shows great promise. Our group has published a new synthetic approach towards cyclic dinucleotides based on phosphoramidite chemistry. These compounds contain the characteristic 2',3'-phosphodiester bond and are derived from natural cGAMP and c-di-AMP. In terms of drug design, the aim was to improve drug uptake by masking the negative charge at the phosphates. In this section, the dideoxy compounds are presented. 2',3'-dideoxy-cGAMP was synthesized by *A.Pappa*, which is the DNA equivalent of natural cGAMP (2',3'-cGAMP, Figure 19). 2',3'-dideoxy-cAAMP and 3',2'-dideoxy-cGAMP were synthesized by *S. Stazzoni* and *F. Hernichel* (Figure 19). To conduct biological experiments with very low amount of compound, the extinction coefficients of corresponding RNA dinucleotides were adopted for the CDNs and the concentration of the compounds were calculated before each experiment.

	2',3'-cGAMP	2',3'-dideoxy-cGAMP	2',3'-dideoxy-cAAMP	3',2'-dideoxy-cGAMP
Ext. Co.	25050	25050	27000	25050
λ	256	256	259	256
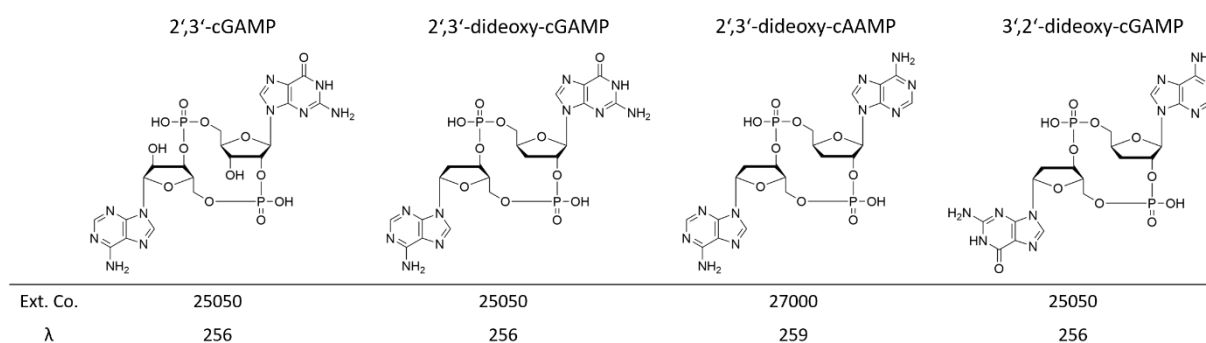
Figure 19: cGAMP analogues synthesized by the chemists of the Carell group.

3.1.1 Response Curves

Monocytes are known to express cGAS-STING endogenously and constitute with 4-11% of circulating leukocytes the third most abundant group of immune cells in the peripheral blood in human beings[177]. They take part in anti-cancer and anti-viral responses, hence are able to address the potential of our CDNs in those two contexts[178,179]. In order to test the synthesized CDNs, THP-1 Dual[TM] cells were chosen for their monocyte-like properties[180]. The THP-1 Dual[TM] cells (provided by Invivogen) are specifically designed to report interferon and NF-κB production. They carry a Lucia luciferase reporter gene which resides downstream of the interferon-stimulated ISG54 promoter. Quantities of expressed luciferase directly correlate to amounts of interferon produced in the cell. In order to quantify the luciferase, QUANTI-Luc[TM] (provided by Invivogen) containing the luciferase substrate coelenterazine, is added to a defined amount of cell medium resulting in a light signal. This signal is measured with a

luminometer (Tecan Genios Pro) providing Relative Light Units (RLUs). The RLUs of each measurement are normalised to the medium background, resulting in a direct read-out of ISG54 promoter activity (Figure 20).
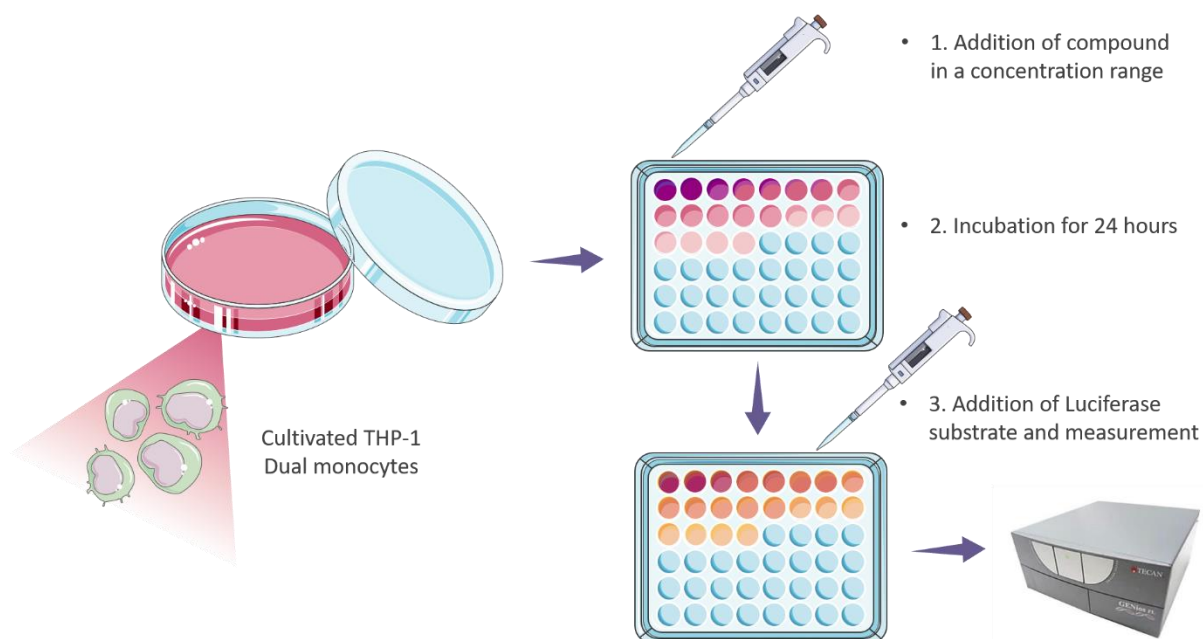
Figure 20: Experimental set up of EC$_{50}$ measurements.

The dose-response curves of the individual CDNs were recorded and compared by their half maximal effective concentration (EC$_{50}$). This is a common measure to compare drug candidates inducing the same response in a certain cell type which stably expresses the target protein. To calculate the EC$_{50}$, a sigmoidal dose response curve must be generated. The dose response curve needs to ideally reach a plateau to ensure the maximum stimulation is reached. For this purpose, cells were split into equal parts and incubated with increasing amounts of the CDN for a defined time after which the response was measured by addition of the luciferase substrate. In order to compare response values from different biological replicates and CDNs, the values were normalised within each data set, setting the highest dose response as 100%. The curve was fitted using the Hill equation, where the inflection point of the curve corresponds to the EC$_{50}$ value. The calculations and analysis were made with the GraphPad Prism software.

In our series of EC$_{50}$ experiments, the cells were incubated with the compound for 24 hours. The EC$_{50}$ of natural cGAMP was verified in our system. Concentration ranges added to the cells were adjusted according to the expected activity of the compounds. These were determined by trials of randomly selected concentrations, not too far from the EC$_{50}$ of natural cGAMP. The tested concentrations ranged from 10 nM to 300 µM, except for the least active compound 3',2'-dideoxy-cGAMP for which concentrations up to 600 µM were used. For each compound, the highest concentration used was also added to the THP-1 Dual^{TM} STING KO (knock-out) cells to observe if any IFN was produced in a STING-independent manner (Figure 22). After incubation for 24 hours the substrate of the luciferase QUANTI-Luc^{TM} was added to the

medium of the cells, following the manufacturers guidelines, and luminescence was measured in a plate reader. The response curves of the CDNs are presented in Figure 21.
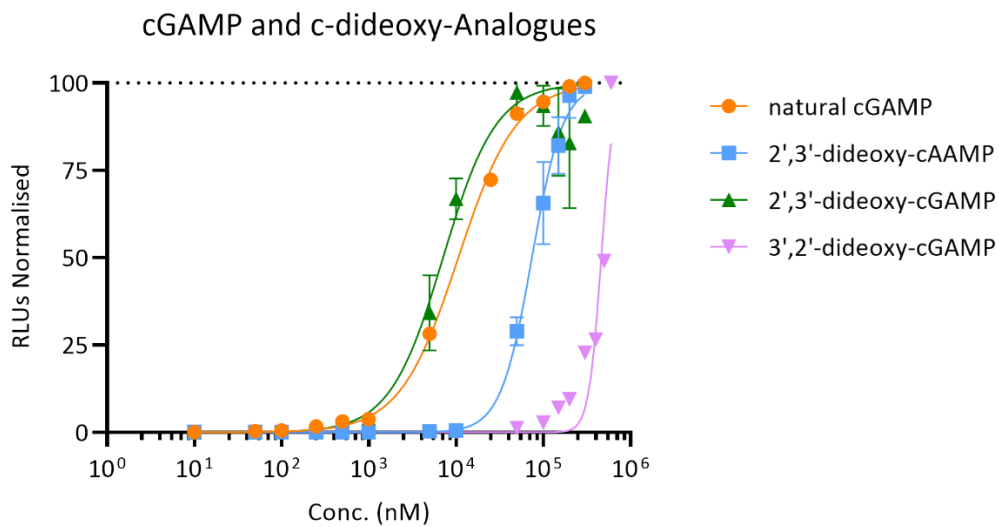
Figure 21: EC$_{50}$ curves of cyclic-dideoxy analogues. 2',3'-dideoxy-cGAMP (green) has an EC$_{50}$ of 7.4 ± 1.65 µM. 2',3'-dideoxy-cAAMP (blue) has an EC$_{50}$ of 74.37 ± 4.55 µM (n=3). 3',2'-dideoxy-cAGMP (purple) needs higher concentrations to provide a EC$_{50}$ value (n=1). The EC$_{50}$ of cGAMP (orange) was measured as 10.6 µM (n=1).

The data show that the dideoxy version of cGAMP has a very similar activation rate compared to natural cGAMP. This provides an insight to the degree of importance of the -OH groups positioned on 2' and 3' of the ribose in terms of activating STING. Another analogue with promising results is 2',3'-dideoxy-cAAMP with an EC$_{50}$ value of 74.4 µM. The EC$_{50}$ value of 3',2'-dideoxy-cGAMP could not be calculated, due to its inefficiency in activating STING. Even at the highest concentration the response did not reach the plateau needed for the accurate calculation of an EC$_{50}$ value.
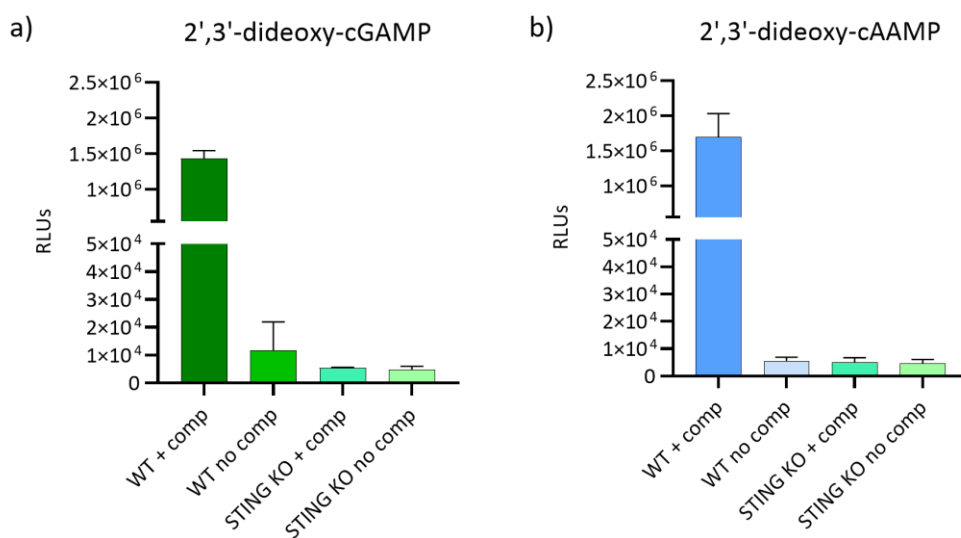
Figure 22: Interferon production in THP-1 Dual WT and THP-1 Dual STING KO with cGAMP analogues (comp).

The compounds 2',3'-dideoxy-cGAMP and 2',3'-dideoxy-cAAMP were given in concentrations of 300 µM to THP-1 WT and THP-1 STING KO cells (Figure 22). No production of IFN was observed in STING KO cells incubated with both CDNs. Thus, it can be concluded that the readouts are only obtained via STING activated interferon production.

3.1.2 Stability Assays

The two most promising compounds, 2',3'-dideoxy-cGAMP and 2',3'-dideoxy-cAAMP, were selected to examine their stability against the known cGAMP degrading enzymes ENPP1 and poxins.

Stability Against ENPP1:

ENPP1 is a type II transmembrane glycoprotein with its active site on the surface of the cell membrane, rendering it an ecto-enzyme[181]. The two main functions of this enzyme were found to be its phosphodiesterase activity and its nucleotide pyrophosphatase activity[182]. ENPPs are known for their role in purinergic signalling and control of bone mineralization[183, 184]. In 2014, Li et al. found out that ENPP1 is capable of degrading cGAMP and is the primary 2',3'-cGAMP degrading enzyme in cultured cells[97]. Further analysis show that ENPP1 specifically hydrolyses 2',3'-cGAMP, but not 3',3'-cGAMP due to its phosphorus atom of the 3'-5' phosphodiester linkage hindering access to the catalytic threonine residue[185,186] (Figure 23). Even though ENPPs are described as membrane-bound proteins, they have also been found in bodily fluids of mammals, including human plasma, both soluble and active in water[187,188].
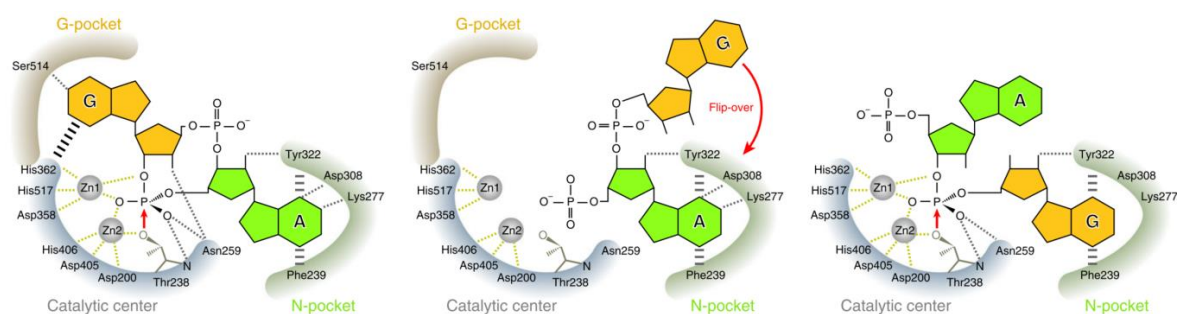
Figure 23: Suggested mechanism of ENPP1 catalysing 2',3'-cGAMP degradation. Adapted from Kato *et al*[186].

ENPP1 is one of two reported cGAMP degrading enzymes. Therefore, the susceptivity of 2',3'-linked cGAMP and their analogues need to be assessed against ENPP1 degradation. To assess the stability of the synthesized cGAMP analogues against ENPP1, the compounds 2',3'-dideoxy-cGAMP and 2',3'-dideoxy-cAAMP were incubated with ENPP1 containing human serum (Figure 25). The reaction buffer was adopted from Eaglesham et al, which contains the zinc ions necessary for the catalytic cleavage[99]. The samples were collected over a time course of 0h, 1h, 3h, 6h, 12h, and 24h and were purified with phenol-chloroform extraction twice to be analysed by high resolution mass spectrometry by *M. Wagner* and *F. Hernichel*. As a control, natural cGAMP containing samples were processed and analysed in identical conditions. The results were compared to samples incubated with natural cGAMP (Figure 25).

Additionally, samples were prepared with heat inactivated (HI, 30 minutes at 56°C) human serum for denaturation of ENPP1, to monitor spontaneous decomposition. For the heat inactivation of the serum, a widely used freely available protocol by manufacturers was followed (i.e., Thermo Fischer). The presence of ENPP1 in human serum is shown in Figure 24.
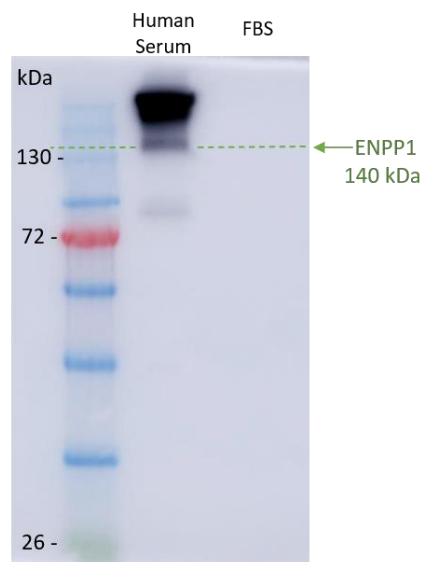
Figure 24: Western blotting of ENPP1 in human serum versus Fetal Bovine Serum (FBS).
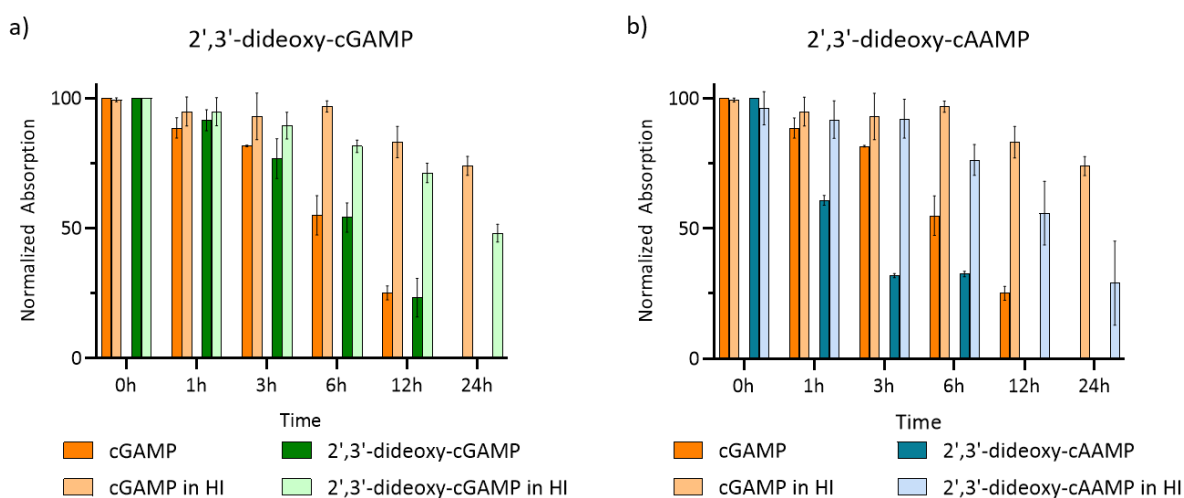
Figure 25: Analogues stability against ENPP1. 2',3'-dideoxy-cGAMP (a) and 2',3'-dideoxy-cAAMP (b) incubated in human serum and heat inactivated human serum for indicated time. Plotted against natural cGAMP in the same conditions.

As seen in Figure 25a, natural cGAMP and 2',3'-dideoxy-cGAMP have almost identical behaviour against ENPP1 in human serum. No improvement was observed upon the removal of the -OH groups from the sugar moiety. The HI human serum shows denaturation of the compound after longer incubation period, which might be explained by partially active ENPP1, unidentified degrading enzymes, or spontaneous decomposition of the compound. On the

other hand, 2',3'-dideoxy-cAAMP was observed to be even less stable compared to natural cGAMP (Figure 25b).

Stability Against Poxins:

Another group of enzymes known to cleave natural cGAMP are poxvirus immune nucleases, collectively called poxins[99]. These were discovered due to hypothesis that DNA viruses must circumvent the cGAS-STING pathway to reproduce in the cytosol with receiving minimum immune response from the cell[189]. In the poxvirus family, there are already known DNA sensing inhibitors working on IRF-3 or TBK-1[190–192]. However, recent discoveries revealed a family of enzymes, inhibiting DNA-sensing before STING is activated[193]. Poxins work on 2',3'-cGAMP hydrolysing specifically the 3'-5' linkage by rotating the adenine base, thus repositioning and nucleophilically activating the 2'-OH (Figure 26)[99]. The specificity towards 2',3'-cGAMP and the stabilization of its negatively charged phosphates is a conserved characteristic among all poxin proteins[193].
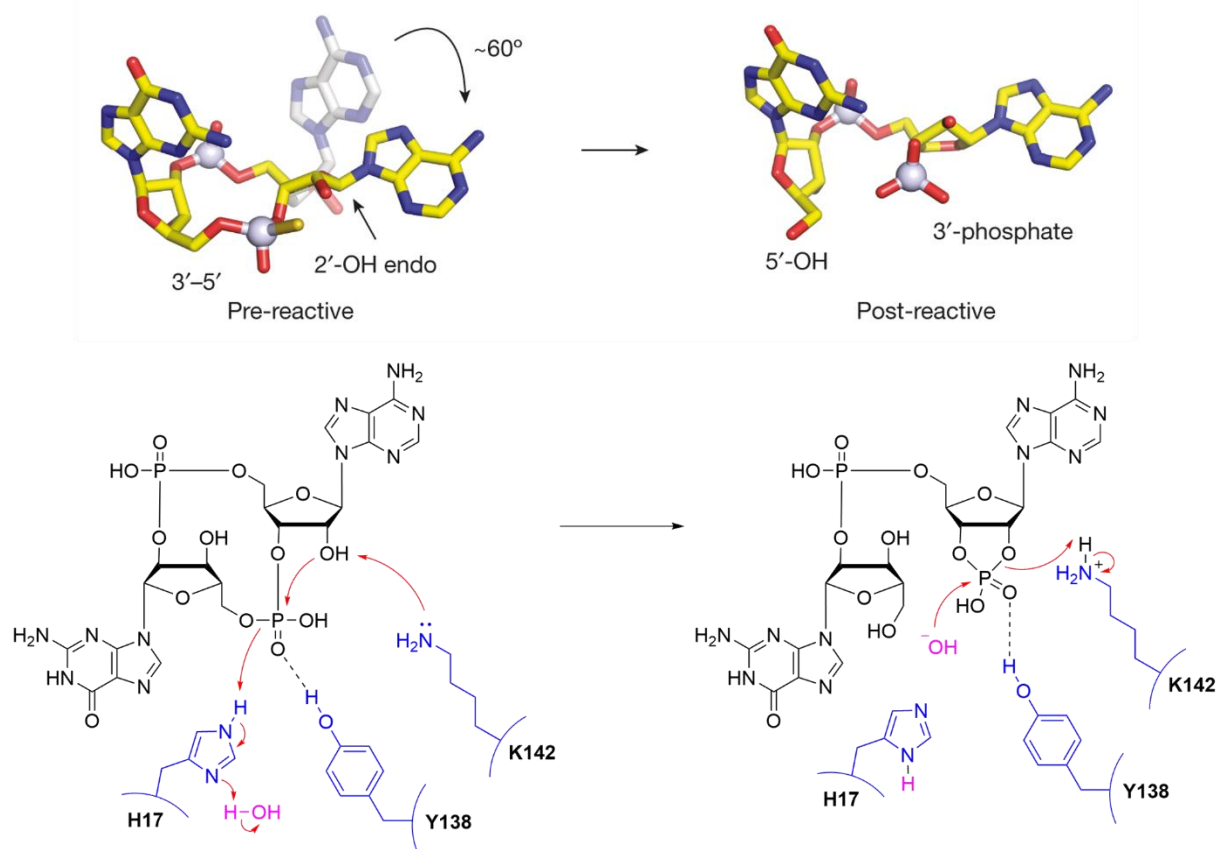
Figure 26: Structural mechanism of poxins degrading 2',3'-cGAMP. Adapted from Eaglesham *et al* [99].

To further characterise the stability of our compounds, both 2',3'-dideoxy-cGAMP and 2',3'-dideoxy-cAAMP were evaluated against poxin degradation. BHK21 cells were cultured and exposed to vaccinia virus (VACV). The cells were transfected with 10 million PFUs of VACV and incubated for 1 hour followed by a post-transfection incubation of 14 hours. The lysates were prepared in a suitable reaction and lysis buffer adapted from Eaglesham et al[99]. Proteins were quantified and distributed in equal amounts per sample. 2',3'-dideoxy-cGAMP and

2',3'-dideoxy-cAAMP were incubated with the lysates separately and samples were collected at time points of 0h, 0.5h, 1h, 3h, and 24h. The reaction was stopped by addition of phenol and chloroform. The steps starting from cell culturing with viral particles up to addition of phenol and chloroform were performed by *S. Bauernfried*. Further extraction and purification with chloroform were performed to ensure purity. The samples were submitted in the high resolution mass spectrometry by *M. Wagner* and analysed by *F. Hernichel* and *A.Pappa*. Natural cGAMP was used as a control and was processed in the same conditions (Figure 27).
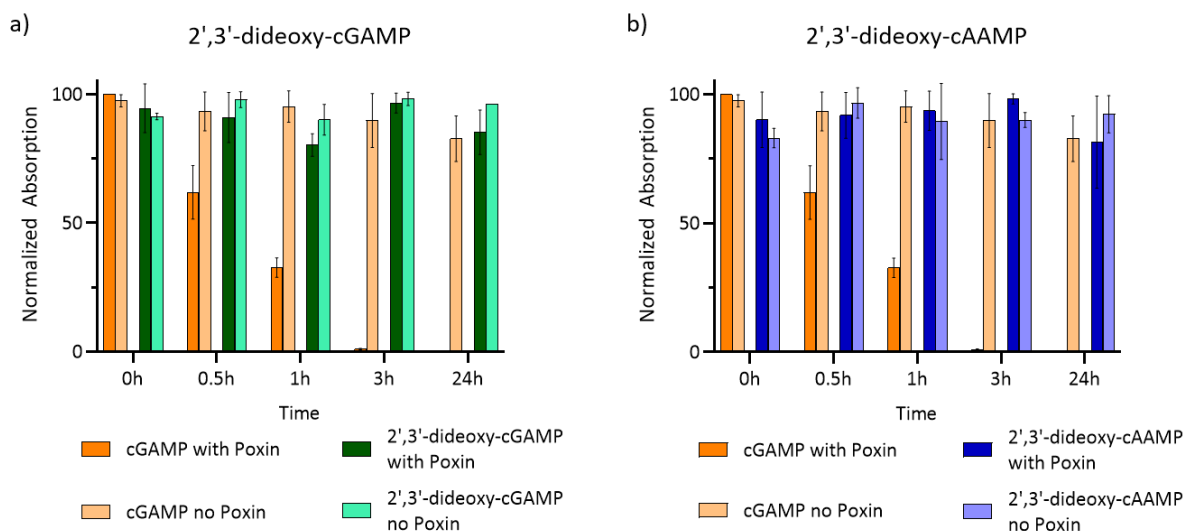
Figure 27: Analogues stability against Poxins. 2',3'-dideoxy-cGAMP (a) and 2',3'-dideoxy-cAAMP (b) incubated in poxin containing lysate and poxin-free lysate for indicated time. Plotted against natural cGAMP in the same conditions.

As shown in Figure 27, both tested compounds show improved stability against poxin degradation compared to natural cGAMP (Figure 27 orange columns). Natural cGAMP is degraded within three hours of incubation, whereas both 2',3'-dideoxy-cGAMP and 2',3'-dideoxy-cAAMP are still intact after 24 hours of incubation with poxins. The lack of the ribose-OH groups in those analogues correspond to the significant increase of stability against poxins.

3.1.3 Conclusion and Outlook

Two promising agonists were identified by their promising EC_{50} values. 2',3'-dideoxy-cGAMP showed an EC_{50} value of 7.4 µM whereas 2',3'-dideoxy-cAAMP showed an EC_{50} value of 74 µM. Both tested compounds have comparable effectivity to natural cGAMP according to the dose-response curves. They also show similar behaviour to natural cGAMP in stability towards ENPP1 degradation. The degradation profile of 2',3'-dideoxy-cGAMP is very close to the natural cGAMP, whereas 2',3'-dideoxy-cAAMP is slightly faster degraded. There seems to be no additional stability against ENPP1 or any other possible cGAMP-degrading enzyme residing in the serum. Therefore, we can conclude that the circulation of the compounds in human serum will have a limited effective time and that the natural behaviour of the compounds is

very similar to natural cGAMP itself. Intra-tumoral injection could however show high effectivity compared to intravenous injection, since the compound would be exposed to the extra-cellular environment for significantly reduced time spans. The potential of these compounds as well as the interaction with ENPP1 or other possible degradation factors in the serum should be explored further.

Both tested compounds were more stable compared to natural cGAMP and show little to no degradation upon poxin exposure. These results confirmed our hypothesis since poxins need the 2'-OH group of adenosines to attack and cleave the CDN, which the tested CDNs lack. The increased stability of both analogues is a very promising result in terms of use in anti-viral contexts. There are more than 350 types of poxins in mammalian viruses, insects, and insect viruses[193]. A poxin resistant analogue of natural cGAMP could bring advantages for boosting the immune system against a novel variant of poxvirus infection or alongside an antiviral drug against a poxvirus.

In fact, smallpox may still be a threat even though it was declared eradicated in 1980 by the World Health Organization due to increased vaccinations worldwide[194]. Concerns are that it may arise from forgotten stocks, global warming melting of the permafrost, or even as a bioweapon[195,196]. Having one of the highest mortality rates shows how relevant research regarding poxins still is. Besides the existing preventive vaccine, a drug called Tecovirimat (TPOXX) was recently approved by the US FDA (Figure 28)[197]. Our poxin resistant analogues carry a great potential fighting a possible smallpox infection. They may work as a combinatorial drug to TPOXX to improve effectivity by enhancing the antiviral response in cells where TPOXX is not highly active. Candidate drugs currently in clinical trials may also benefit from an enhanced antiviral reaction provided by our poxin-resistant cGAMP analogues. Since the working mechanism of the tested cGAMP analogues are not interfering with the reproduction pathway of the newly produced viruses for which the antiviral drugs are usually targeted to, including TPOXX, they could perform as a combinatorial drug to many antiviral drugs without interfering with their mechanisms.
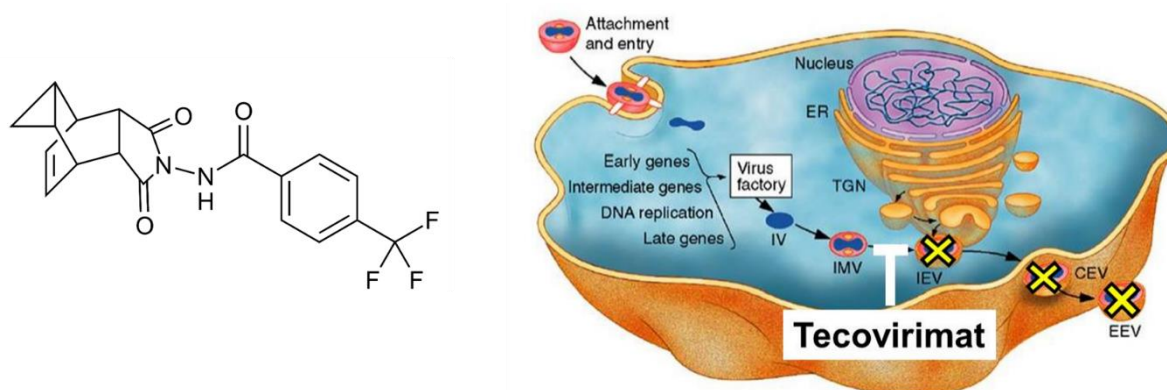
Figure 28: Tecovirimat (TPOXX) chemical structure and mechanism of action. Adapted from *SIGA Technologies Inc*.

3.2 Prodrugs of 2',3'-dideoxy-cAAMP

When a drug is developed chemically, its biochemical qualities are rather unknown and potential problems can be encountered in biological studies. Especially important for efficient drug delivery are compound solubility and lipid membrane permeability. Depending on the characteristics of the drug, these features need to be improved regarding the site of action. Prodrugs are biologically inactive compounds which need to undergo a chemical or enzymatic modification *in vivo* in order to become biologically active. Designing a prodrug is usually a necessity to improve aqueous solubility, oral absorption, metabolic stability, brain penetration, or to avoid toxic effects of an existing drug[198]. The prodrug approach has proven its benefits in the last decades and 12% of the US-approved drugs successful in clinical trials between 2008-2017 are characterised as prodrugs[199]. One of the biggest challenges in drug delivery is crossing the cell membrane to get into the cell interior. If the compound is hydrophilic and has a good aqueous solubility it may encounter the hydrophobic lipid membrane as a barrier (Figure 29). The most widely used family of prodrugs for increasing permeability are esters[200]. Ester bonds can be hydrolysed by esterases residing in the body, once the prodrug is administered[201]. More specifically carboxylesters are one of the most common charge-masking groups which are cleaved off by carboxylesterases. The family of carboxylesterases is ubiquitous and easily accessible in the human body[202]. One example of a prodrug using a carboxylester as their promoiety is the anti-cancer topoisomerase inhibitor prodrug CPT-11 (irinotecan)[203].
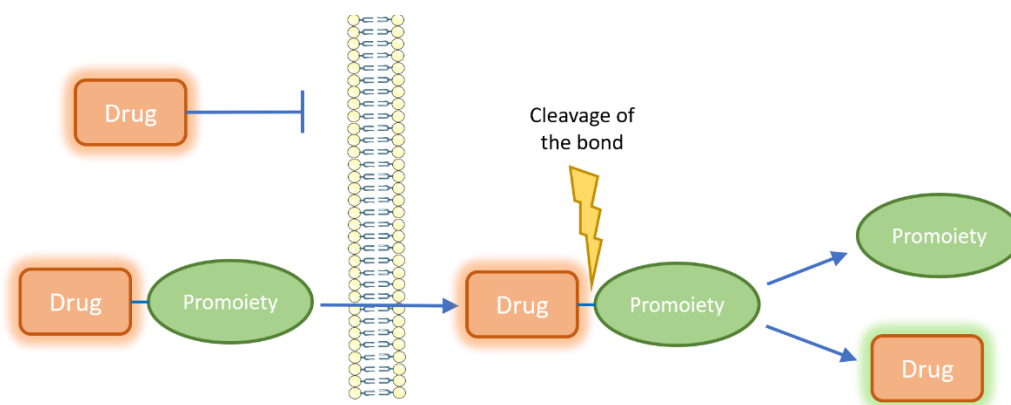
Figure 29: Principle of a prodrug for cell membrane permeability.

3.2.1 Strategy of the SATE Prodrug

SATE linkers have been introduced as phosphate masking groups on mononucleotide drugs, resulting in pronucleotides (or protides)[204]. As an example, the anti-HIV drug zidovudine was enhanced for oral absorption and cell permeability by phenyl-SATE[205]. In case of the 2',3'-dideoxy-cAAMP, even though the EC_{50} was measured to be about 74 µM, the charged phosphate groups are predicted to limit the permeability across the lipid bilayer. A prodrug strategy was developed by *S. Stazzoni* using a S-Acyl-2-thioethyl (SATE) moiety positioned on the phosphate group as promoiety to reversibly mask the negatively charged phosphates (Figure 30a). The SATE promoiety is a thioester, which is cleaved off under physiological

condition by a two-step esterase reaction (Figure 30b). Once the thioester is removed, intramolecular nucleophilic attack of the thiol group leads to the formation of thiirane, thus releasing the free phosphate 2',3'-dideoxy-cAAMP. The SATE promoiety was designed containing an alkyne bearing acyl chain to allow late-stage modification via CuAAC click chemistry, for targeting or transport enhancement. With the possibility of late-stage modification, the designed prodrug can be diversified for more specific purposes.
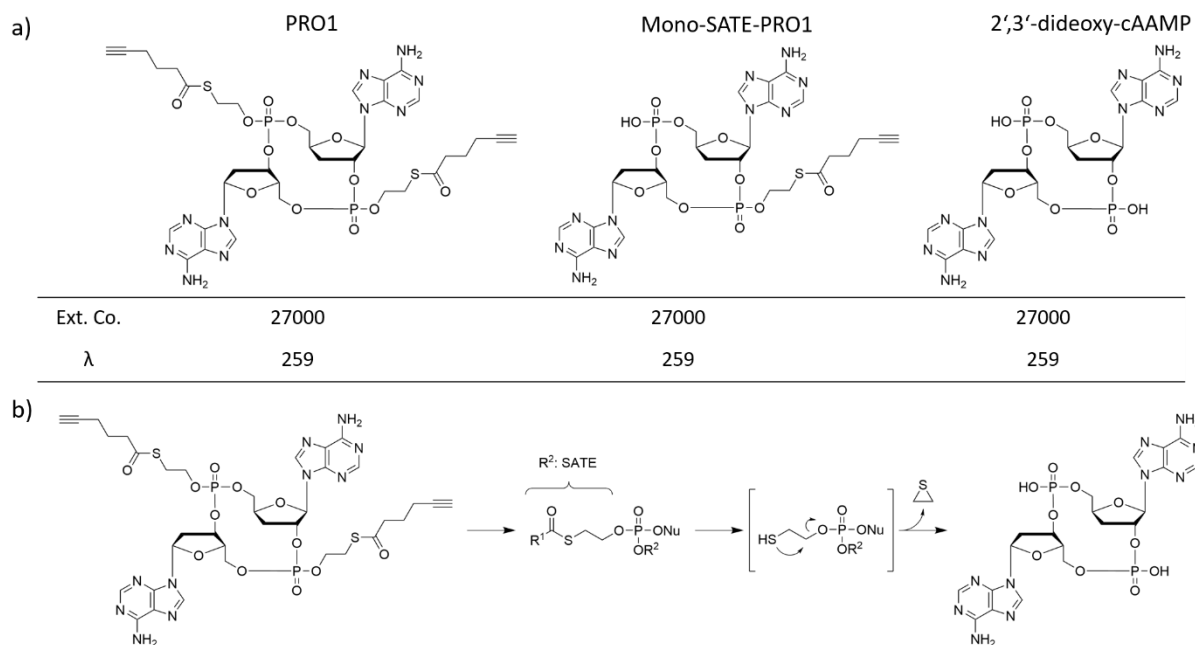
Figure 30: 2',3'-dideoxy-cAAMP prodrugs, 2',3'-cAAMP, and PRO1 synthesis. a) PRO1 containing SATE linkers on both phosphates, synthesis developed by *S. Stazzoni*. Mono-SATE-PRO1, having the SATE linker on the 2'-phosphate, synthesized by *S. Veth*. 2',3'-cAAMP synthesiezed by *S. Veth*. b) PRO1 conversion to 2',3'-dideoxy-cAAMP.

The enhancement of the cell permeability by the SATE promoiety is expected to increase its effectivity, along the principle of the prodrug strategy. The 2',3'-dideoxy-cAAMP has two phosphates which can be masked. The SATE-modified 2',3'-dideoxy-cAAMP was called PRO1. *S. Veth* has synthesized a Mono-SATE-PRO1 in which only one SATE was used (Figure 30a). Furthermore, he synthesized the 2',3'-cAAMP for direct comparison of the interferon activation to observe if the presence of the 2' and 3' -OH groups on the sugar moiety result in a significant alteration.

In order to have the prodrug strategy working, the ester bonds of the promoiety need to be cleaved off when the prodrug enters the cytosol. Human carboxylesterases can catalyse the reaction of many esters, including thioesters[206]. The human carboxylesterase 1 (CES1) has a serine residue in its catalytic pocket, which divides the pocket into two spaces. One of those pockets prefers specifically smaller acyl groups, whereas the other can accept bulkier groups, which allows CES1 to have a wide range of ligands[207,208]. The working mechanism is conserved in all serine hydrolases. First the His-468-base-activated Ser-221 attacks the carbonyl carbon of the substrate. With this the thiol, amine, or alcohol is released. Then a water molecule

performs a nucleophilic attack on the acyl-enzyme complex, thereby restoring the carboxyl esterase to its original state and releasing a carboxylic acid (Figure 31)[202].
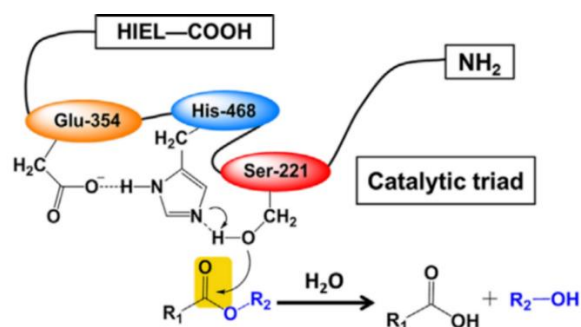
Figure 31: Human carboxylesterase 1 catalytic function. Adapted from *Wang et al* [206].

The proof of concept was provided with an *in vitro* assay performed and reported by *S. Stazzoni*. The prodrug was incubated with human carboxylesterase 1c (hCES1c) over a time course ranging up to 36 hours in a 0.1 M HEPES buffer at 37°C. The digested mix was analysed via HPLC, proving that mono-cleavage of the SATE moiety starts already after 1 hour of incubation, producing first Mono-SATE-PRO1. Then second SATE moiety was cleaved after 3 hours, producing the free active compound 2',3'-dideoxy-cAAMP. More details are to be found in chapter 3.8.1 in the thesis of *S. Stazzoni*[209].

3.2.2 Response Curves

After the proof of the prodrug concept, PRO1 and Mono-SATE-PRO1 were both added to THP-1 Dual^{TM} cells to assess the degree of enhancement of their EC_{50} values. PRO1 was added in concentrations ranging from 0.1 nM to 5 µM, whereas Mono-SATE-PRO1 was added from 0.1 nM to 100 µM. Concentrations were reduced relative to the previous experiments due to expected increase in performance of the prodrug compounds. After 24 hours of incubation the luciferase substrate was added and relative light units (RLUs) were measured using a plate reader.
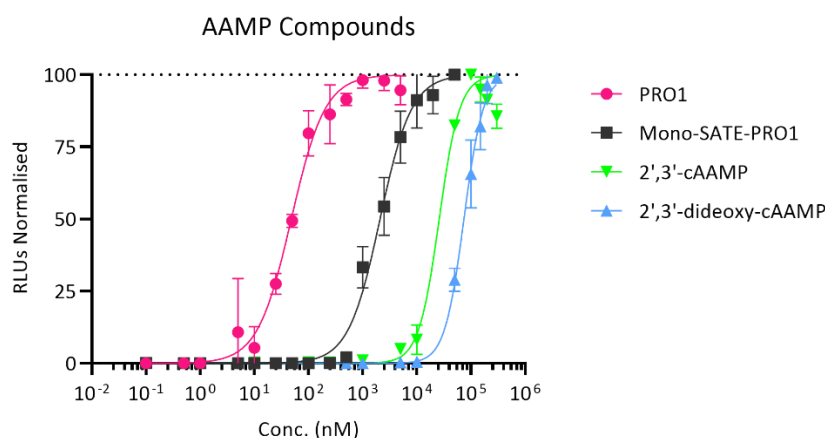
Figure 32: EC50s of AAMP Compounds and Prodrugs. The PRO1 has an EC_{50} of 48,9 ± 7.7 nM (pink). The Mono-SATE-PRO1 has an EC_{50} of 2.1 ± 0.26 µM (black). The 2',3'-cAAMP has an EC_{50} of 26.6 ± 4.9 µM (green). The 2',3'-dideoxy-cAAMP has an EC_{50} value of 74.4 ± 4.6 µM (blue).

The EC_{50} of PRO1 was calculated to be around 49 nM, whereas the EC_{50} of Mono-SATE-PRO1 was approximately 2 μM (Figure 32). With only one phosphate group masked by the SATE linker, the Mono-SATE-PRO1 was able to increase the EC_{50} of the unprotected derivative about 40-fold. The masking of both phosphate groups in PRO1 improved the EC_{50} by another factor of 40 by which the EC_{50} dropped to a two-digit nanomolar range. This provides an insight of the efficacy of the SATE linkers, first by masking the charged phosphates and then releasing the drug via carboxylesterase cleavage inside the cell. The SATE linkers provide a great enhancement to the 2',3'-dideoxy-cAAMP, which can be utilized in many contexts where production of interferons is desired.

As a side product of the SATE cleavage of PRO1 and Mono-SATE-PRO1, thiirane is released in the cytoplasm. Thiirane derivatives are potentially cytotoxic compounds, inhibiting the matrix metalloproteinase MMP-2 and MMP-9[210]. However, these derivatives were found to require the presence of phenoxy-phenyl to execute their inhibitory functions[211]. Therefore, it may be speculated that the toxicity of thiirane released from PRO1 is fairly low.

To observe if there are any STING-independent interferon activation induced by the side product after the SATE linker is cleaved off, Mono-SATE-PRO1 was added to both THP-1 WT and STING KO cells and the interferon response was measured with the luminescence assay (Figure 33). There has been no change observed between the compound administered and non-administered STING KO IFN-I production. Hence, it can be concluded that the SATE linker does not create additional IFN production igniting an immune reaction, and the IFN-I production results from STING signalling only.
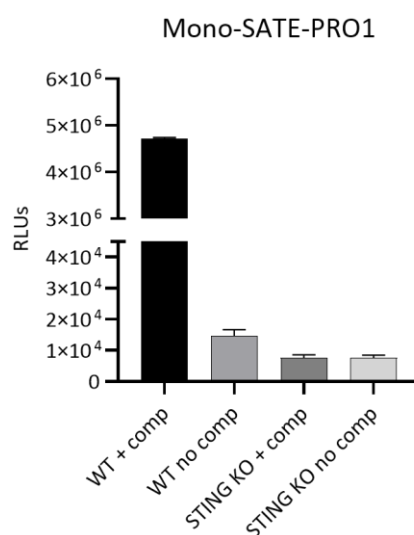
Figure 33: Interferon production in THP-1 Dual WT and THP-1 Dual STING KO with Mono-SATE-PRO1 (comp).

3.2.3 Conclusion and Outlook

Prodrug versions of 2',3'-dideoxy-cAAMP were prepared by the chemists of the *Carell* group. These were tested in the same manner as initially described cGAMP analogues in THP-1 cells and were found to be highly active in inducing IFN production. The introduction of the SATE linkers on both phosphate groups improved the EC_{50} from 74 µM to 49 nM. The SATE-induced increase in lipophilicity can also be utilised for oral availability. Several ester-prodrugs were developed to allow oral intake of existing drugs, such as ampicillin, candesartan, and Olmesartan[212]. In these cases, the access of the esterase to the cleavage point was enhanced by introducing a spontaneously cleaving linker. This accelerated the cleaving rate of the esterase, hence activation of the drug. Even though the efficacy of the 2',3'-dideoxy-cAAMP was significantly improved by the SATE linkers, different linker lengths may be tested for even higher rates of activation.

Targeting specifically tumours is an important aspect for immunotherapeutic drugs, since the increase of immune response in healthy tissue is undesirable. Hence, the clickable sites of PRO1 may also aid target selection. Due to metabolic changes in cancer cells, tumours develop low pH extracellular environments[213]. The change in pH was used already for concentrating active drugs to the specific area[214–217]. A similar approach could be considered for improving PRO1 targeting and release in cancer cell environment.

Furthermore, it has been revealed that SLC19A1 is partially responsible for cGAMP uptake in monocytes and other immune cells[130]. SLC19A1 knock-out monocytes could be used to provide further insight about the PRO1 uptake strategy of the cells. If the majority of PRO1 is taken up via the receptors instead of diffusion through the lipid bilayer, clicked moieties with a large size could potentially block the entry of PRO1. Hence, further investigation on the uptake would elicit more directed strategies.

3.3 Photocleavable Prodrug of 2',3'-dideoxy-cAAMP

Photocleavable protecting groups (PPG) allow control over the location and time a compound is wished to be released. The first application for a photocleavable group on a nucleoside was designed for cAMP release[218]. The phosphate groups were masked by *o*-nitrobenzyl esters to allow cell permeability. Later on, the PPG strategy expanded to further biomolecules in various fields and inorganic compounds. Some criteria have been established about the design of a PPG. For instance, absorbable wavelength above 300 nm is required to avoid photodamage to the biological system. High yields upon short periods of activation are desired as well as low background activity before the release to avoid unwanted side effects. Solubility in the targeted medium and non-toxic as well as colourless by-products to avoid damage and competitive absorbance are additional desirable properties of PPGs[219]. Even though these factors need to be considered, one PPG system design might not be able to tackle all of the before mentioned challenges.

o-Nitobenzyl and *o*-nitrophenyl derivatives are currently the most widely used PPGs[220,221]. Some of their known disadvantages are a low absorbance at higher wavelengths, thus requiring more energetic and therefore more damage-inducing short wavelength irradiation. Also, releasing potentially toxic byproducts is a commonly encountered disadvantage. However, they can be derivatised with a large sequence of functional groups including thiols, carboxylic acids, and phosphates and provide a simple synthesis, consistent activation rates in various contexts and precise spatio-temporal control.

As shown in Figure 32 in section 3.2.2 the EC_{50} of 2',3'-cAAMP is almost 3-fold lower than that of its deoxy version 2',3'-dideoxy-cAAMP. Also, since natural cGAMP is an RNA CDN, introducing the OH groups in the synthesized analogues would bring them closer to naturally occurring circumstances. However, synthetic challenges make it unlikely for a ribose PRO1 to exist. Since the phosphotriester moieties and the -OH groups are in close proximity, the final compounds are unstable due to the susceptibility of the triesters to intramolecular nuclephilic attack by the neighbouring -OH. To overcome this challenge, *S. Veth* has developed a strategy with PPGs on the 2'-OH and 3'-OH using a *o*-nitrophenyl-ethoxy-methyl moiety shown in Figure 34. The compound is named PC-PRO1.
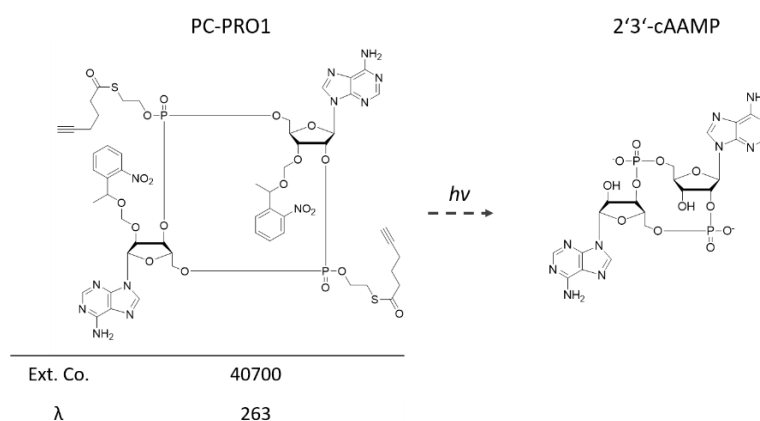
Figure 34: Structure of PC-PRO1 and desired end product 2',3'-cAAMP. Designed and synthesized by *S. Veth*.

3.3.1 Strategy of the Photocleavable Prodrug

The proposed mechanism of action for PC-PRO1 is shown in Figure 35. The SATE linkers would provide lipophilicity and facilitate crossing the cell membrane. After PC-PRO1 enters the cell, esterases would cleave off the SATE linkers. Only then a light exposure can release the active compound in a stable manner. Therefore, the timing of the light exposure following the administration of the compound is critical.
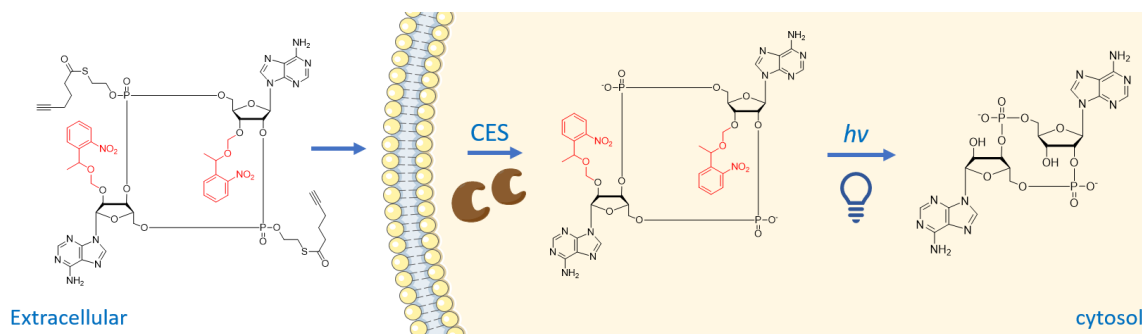
Figure 35: PC-PRO1 working mechanism. PC-PRO1 crosses the cell membrane. The SATE linkers get cleaved off by carboxylesterases (CES). Light is shine on the system to induce photocleaving. 2',3'-cAAMP is released.

After the successful synthesis of the compound, the extinction coefficient was measured by *S. Veth* to proceed with the evaluation studies. In order to determine the efficiency of the photocleaving and the most effective light wavelength, an experimental set up was prepared allowing relative quantification by HPLC analysis. 10 nmol of PC-PRO1 in phenol-red-free test medium for THP-1 cells were divided in a cell culture plate to expand the exposure surface of the sample. The samples were exposed to UV light in a time dependent manner using two different lamps with 312nm and 365nm wavelength per sample to determine the optimum wavelength. The samples were collected at various time points to be extracted for the HPLC analysis; however, this step created some challenges. The usually known and applied extraction method with an ice cold 1:1 solution of H_2O and acetonitrile caused inconsistencies among samples due to irregular phase-separation. After trials with phenol-chloroform extraction led to the same issue, a 1:1 solution of ethylacetate and acetonitrile was used which yielded consistent levels of phase separation, hence comparable outcomes.

The starting compound PC-PRO1 was observed to decrease relatively faster with 312nm light, compared to 365nm light (Figure 36). At 312nm, the starting material was almost completely converted after 20 minutes. However, at 365nm, after 3 minutes the release of the product came to a halt. A maximum of 13% of PC-PRO1 was processed. Regarding these results, a photocleaving under 312 nm wavelength light is necessary. To assess the possibility of applying the same system on cells, viability assays were conducted on THP-1 monocytic cells.
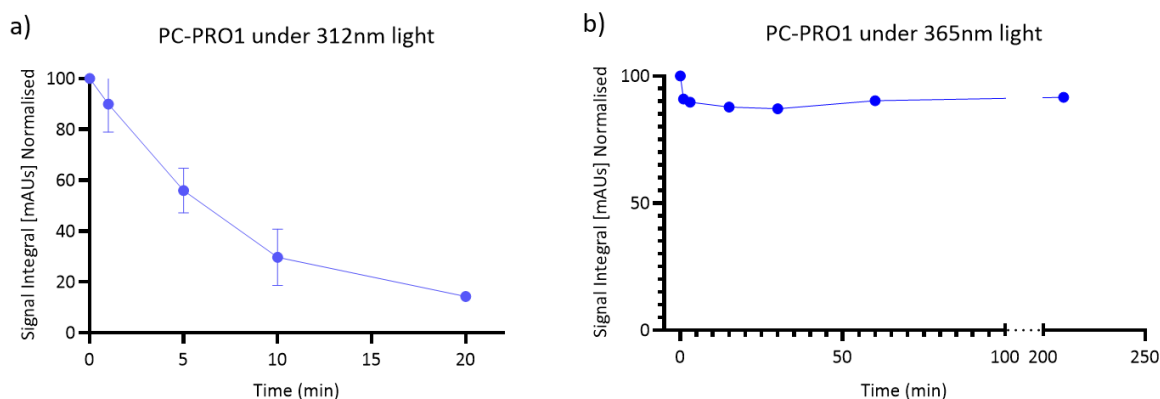
Figure 36: PC-PRO1 in analytical RP-HPLC after light exposure. a) 312nm light on samples over 20 minutes with a power of 26.2 nJ/cm². b) 365 nm light on samples over 210 minutes with a power of 2.54 nJ/cm².

3.3.2 Response and Viability Assays

For the viability test, THP-1 Dual™ cells were introduced to the phenol-red-free test medium, and were distributed on the identical cell culture plate to replicate the light exposure. An MTT assay was performed to quantify viability of the cells by measuring absorbance of the sample, without the addition of the PC-PRO1. As seen in Figure 37, cells exposed to 312nm light already started dying in minute 1 and more than half of the cells lost viability in minute 3. As a comparison, when exposed to 365 nm light, the cells seem not to be affected as much.
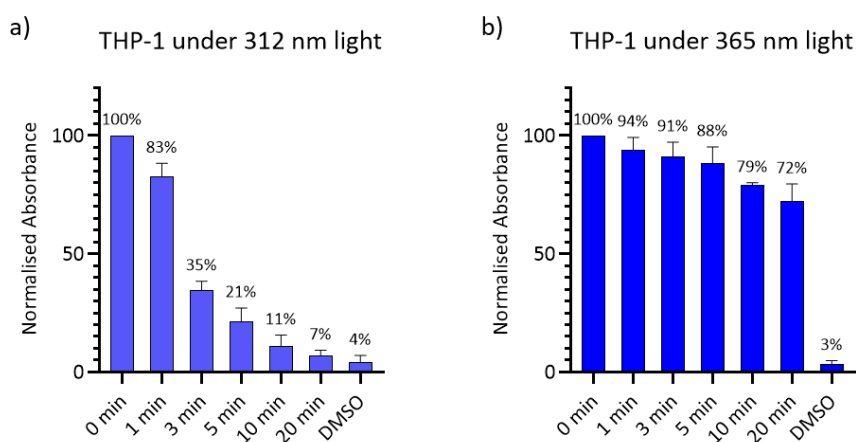
Figure 37: Viability assays of THP-1 after light exposure. a) 312nm light on samples over 20 minutes with a power of 26.2 nJ/cm². b) 365 nm light is exposed over 20 minutes with a power of 2.54 nJ/cm². 10% DMSO serves as a negative control for both sample sets, n=3.

From the data of the photocleaving-efficiency experiment and the viability assays, it can be concluded that the given conditions will not lead to a desirable outcome when PC-PRO1 is introduced to THP-1 cells. At 365 nm wavelength even though the cells remain viable, the photocleavable groups of PC-PRO1 were observed to be cleaved inefficiently (Figure 36). At 312 nm light the efficiency of the cleavage of the protecting groups was increased, however the cells responded badly by dying (Figure 37). To observe the combination of PC-PRO1 and light exposure on THP-1 monocytic cells, PC-PRO1 was added to the cells with an end concentration of 100 nM and the cells were exposed to 312nm and 365 nm light in two

separate time course experiments, as shown in Figure 38. In these samples, the response induced by the photocleaved PC-PRO1 was measured by the interferon response via the QUANTI-Luc[TM] reagent. PRO1 was used as positive control. Unfortunately, no interferon signalling was observed in samples with PC-PRO1 and light treatment in both wavelengths.
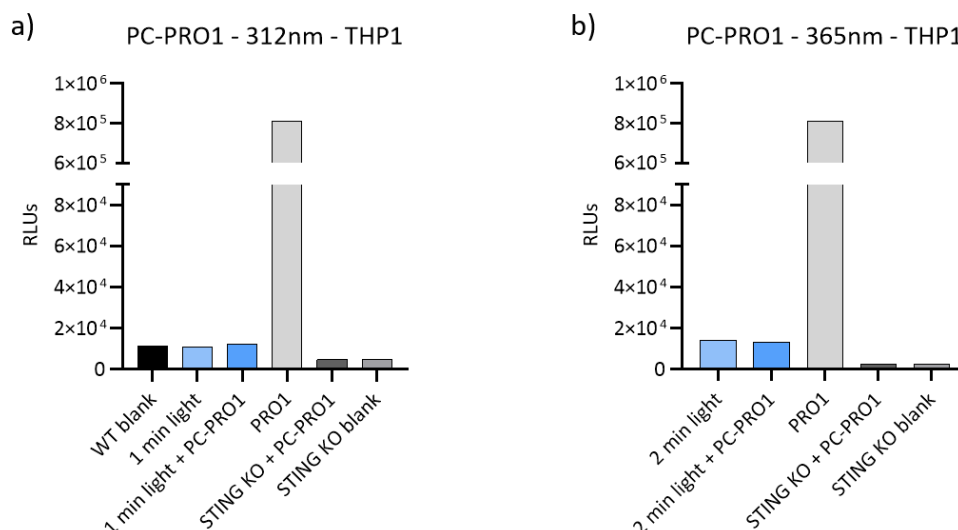
Figure 38: PC-PRO1 feeding on THP-1 Dual[TM] cells with light exposure. a) 6h incubation with 100 nM PC-PRO1 before 1 min 312nm light exposure, followed by 18h post-incubation. b) 1h incubation with 100 nM PC-PRO1 before 2 min 365nm light exposure, followed by 23h post-incubation. Samples were measured for IFN response via the QUANTI-Luc[TM] reagent. n=1 in each data set.

3.3.3 Conclusion and Outlook

In this section, a photocleavable prodrug was evaluated for application on cells. The PC-PRO1 was found to be photocleaved at 312 nm light, however the THP-1 monocytic cells were observed to lose viability in the application period. No IFN production was observed to be induced upon addition of the compound on THP-1 monocytic cells.

A potential improvement factor for the compound to work on cells is the light source. Another lamp with an emission wavelength between 312 nm and 365 nm could be used. More importantly the power of the lamp could be increased and pulsating light with exposure times in millisecond range could be employed. The light source of the 365 nm light used in these experiments only has a power of 2.54 nJ/cm^2 which is very low compared to applied light in published research[222]. A more robust improvement would be to use a more red-shifted approach. Two-photon infrared excitation is less-damaging and provides a higher three-dimensional resolution with a deepened penetration[223,224]. *o*-Nitrobenzyl derivatives were observed to be excited both by one-photon and two-photon excitation[225]. In *o*-nitrobenzyl containing hydrogels for example, cell compatibility was achieved when two-photon excitation was applied, instead of UV light[226]. Even though the cost and availability of excitation sources for two-photon light are limiting factors, it could be considered to apply two-photon excitation on PC-PRO1 containing cells relying on future enhancement of the application.

Part II: Antagonist of STING

3.4 Evaluation of a STING Inhibitor

It was described that cGAS-STING overactivity leads to auto-immune diseases, in certain contexts to cancer development, and more prominently induces aging and age-related diseases. The basal innate immune response of aged cells makes this molecular pathway available for intervention with therapeutics for age-related events. Small molecule drugs have been developed for targeting the cGAS-STING pathway, specifically binding covalently to STING and blocking the ligand binding domain (LBD) to prevent access of cGAMP. In the last years, a new strategy had been developed for targeted protein inhibition and degradation called the PROTAC strategy.

3.4.1 The PROTAC Strategy

<u>P</u>roteolysis <u>T</u>argeting <u>C</u>himeras (PROTACs) are bifunctional molecules, containing a moiety which recruits and binds to a target protein, and another linker-bound moiety which hijacks the ubiquitin-proteasome system to degrade the targeted protein[227] (Figure 39). The PROTAC approach is distinct in terms of the functioning mechanism. Instead of using inhibitors on disease causing proteins, a reduction of the protein level is achieved. Enzymes, transcription factors, and regulatory proteins are some of the many proteins to be downregulated by a PROTAC, which are described as Protein of Interest (POI)[228]. PROTAC efficiency depends on selection of all subunits, as well as linker length, type, linking site, and stability of the ternary complex.

PROTACs are specifically in the spotlight for cancer treatment. Many diseases are prone to gain resistance towards an applied therapy and the diseases reoccur. One of the PROTACs under clinical trials is the androgen receptor-targeting ARV-110 for metastatic castration-resistant prostate cancer, another one being ARV-471 for advanced or metastatic ER+/Her2 breast cancer[229]. With the PROTAC approach, undruggable proteins can also be targeted. Proteins lacking a catalytic site are a challenge to target by an inhibitor. Signal Transducer and Activator of Transcription 3 (STAT3) is such an example, for which successful degradation was achieved by a PROTAC design bearing an analogue of lenalidomide for the E3 ligase recruitment, resulting in tumour regression in a mouse model[230]. A PROTAC targeting the cGAS-STING pathway might provide for the same purpose in metastatic cancers, however from a more upstream position of the cascade.

The ubiquitin-proteasome system (UPS) is involved in many regulatory and response pathways in the cell. The mechanism can be divided into two steps (Figure 39). First, the target protein is ubiquitinated, then the proteasome complex degrades the protein in question, releasing the reusable ubiquitin. The ubiquitylation is organised by E1, the ubiquitin activating enzyme, E2, which is the carrier of ubiquitin bringing ubiquitin to the site, and E3 ligase, which transfers the ubiquitin to the target protein[231].
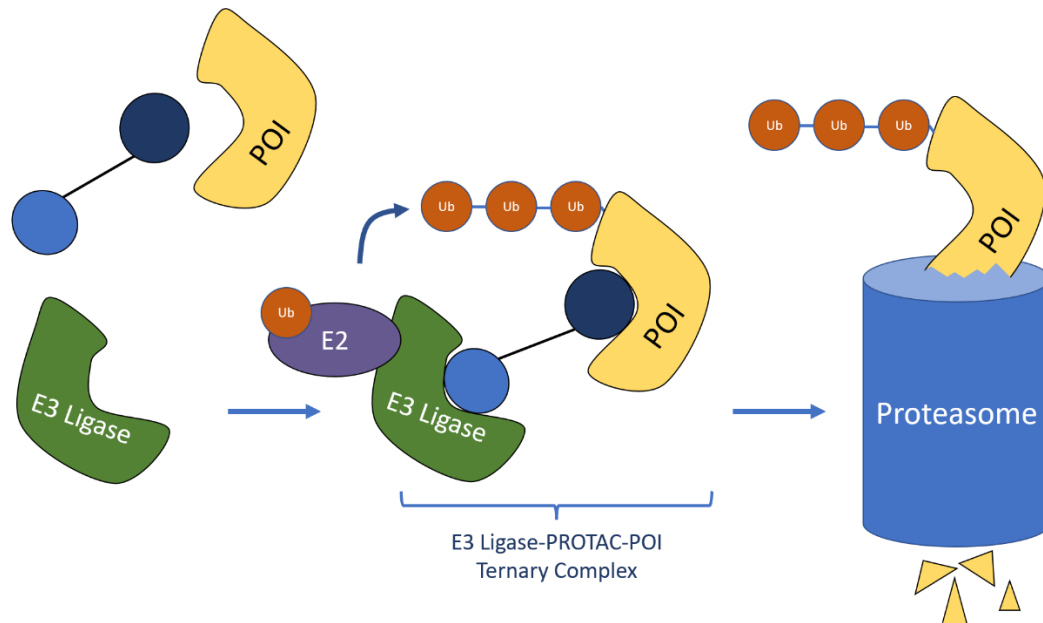
Figure 39: PROTAC working mechanism. The linked two blue circular units represent the PROTAC, the light blue circle being the E3 ligase recruiter, the dark blue being the target protein recruiter. POI stands for Protein of Interest. The PROTAC binds to the POI and the E3 Ligase as one unit. This ternary complex is described as the stable E3 ligase-PROTAC-POI formation which allows ubiquitination of the POI. The ubiquitinated POI is then degraded by the proteasome system.

There are more than 600 E3 ligases in humans, working not only on degradation, but also on signalling and interaction of proteins[232]. E3 ligases bind to their targets by protein-protein interactions, non-protein molecules which mediate the binding, or by a binding-motif which recruits accessible targets[233]. One of the most widely used E3 ligase recruited in PROTAC strategies is cereblon (CRBN)[234]. Cereblon's modulator thalidomide, and its less toxic derivatives lenalidomide and pomalidomide, are drugs initially produced for multiple myeloma and B-cell related diseases[235,236]. For the PROTAC strategy, these small molecules work successfully as recruiters of CRBN, hence triggering the UPS system. Using a cGAMP derivative as a recruiting moiety for STING, a PROTAC was designed by *G. Ganazzoli*. A pomalidomide was selected as a CRBN recruiter and was bound to the STING recruiter consisting of a natural cGAMP with a polyethylene glycol (PEG)-linker via click chemistry (Figure 40).

PROTAC1   STING Recruiter

Ext. Co.	28651,5	25050
λ	257	256
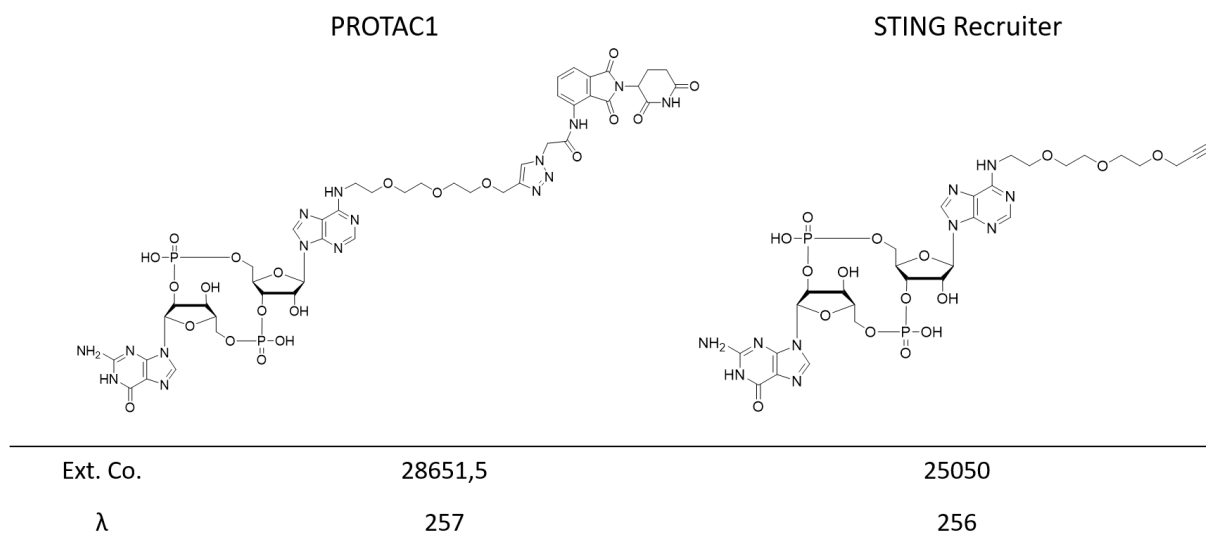
Figure 40: Structures of PROTAC1 and the STING recruiter. PROTAC1 designed with the CRBN recruiter pomalidomide. Both designed and synthesized by *G.Ganazzoli*.

To study if the STING recruiter is able to bind STING, THP-1 Dual^{TM} cells were incubated with different concentrations of the STING recruiter for 24 hours. Ligand binding of STING is expected to induce a conformational change, which is expected to induce activation of STING. Hence, IFN production of THP-1 monocytic cells were measured after the incubation by the reporter system also used for EC$_{50}$ measurements earlier with the RLUs as a read-out. A STING activation was observed at high concentrations of the STING recruiter, such as 100µM and above (Figure 41). This provided an insight about the functionality of the designed STING recruiter and also demonstrated the delivery of this unit without any need of transporter reagent. The high concentration applied was only specifically selected for the STING recruiter, which will be modified when the full PROTAC1 is in use. Studies were continued with the full compound PROTAC1.
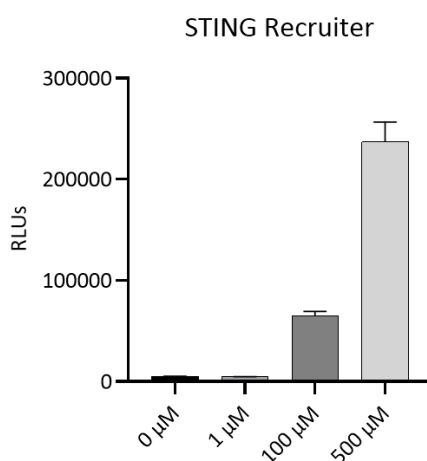
Figure 41: STING recruiter binds to STING.

3.4.2 Response Assays

The ternary complex (E3-PROTAC-POI) formation and stability is the rate determining step for the successful degradation of the protein of interest. In this regard, the determination of the testing concentration is crucial. If too concentrated compound is added, the action can be silenced by binary complexes employing separate PROTACs, an event called the "hook effect" (Figure 42). In most cases this is known to happen starting from 1-10 µM range[237].
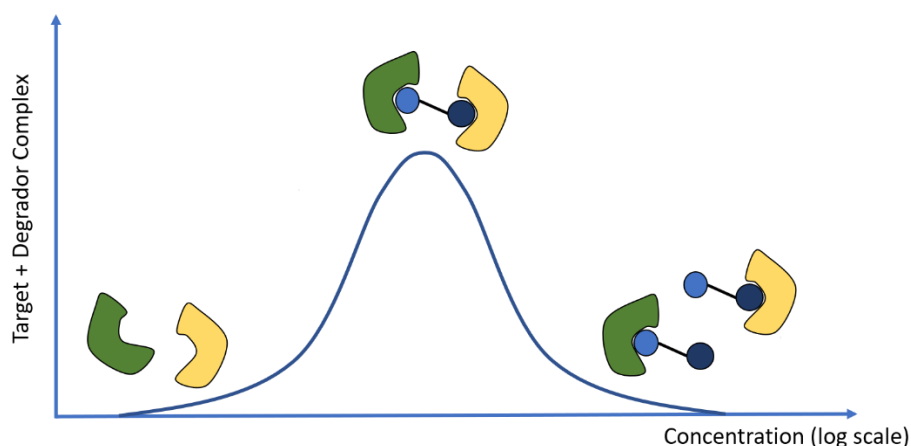
Figure 42: The Hook effect.

In order to observe a possible degradation of STING by PROTAC1, THP-1 monocytic cells were treated with PROTAC1 and STING levels were analysed by western blotting, along with CoxIV providing as loading control. A range of concentrations from 5 nM to 100 nM were added to the cells in medium without any transfection reagent. After 16 hours of incubation, the samples were collected and proteins were extracted. Equal amounts of total protein were loaded as determined by BCA assay before each gel run and blotting. The samples were separated on an SDS-PAGE gel, which was followed by a wet blot on nitrocellular membrane. After the blocking with milk powder the membrane was cut through horizontally along 26 kDa to separate the larger STING from CoxIV. STING and CoxIV were targeted with appropriate primary and secondary antibodies for detection and imaging.

The blot already indicates in a visible level, a degradation of STING compared to CoxIV control around 25 nM and 50 nM (Figure 43). When the bands are integrated for their degree of intensity, a numerical representation is obtained all normalised to the corresponding CoxIV band intensities. These numbers are only representatives of the possible outcome, for a more reliable value biological replicates must be produced. Nevertheless, the ideal working concentration of the PROTAC1 seems to be in a two-digit nanomolar range, which indicate a successful uptake by the cells without the use of any transfection reagent and a proof of concept of PROTAC1 efficiency on STING.
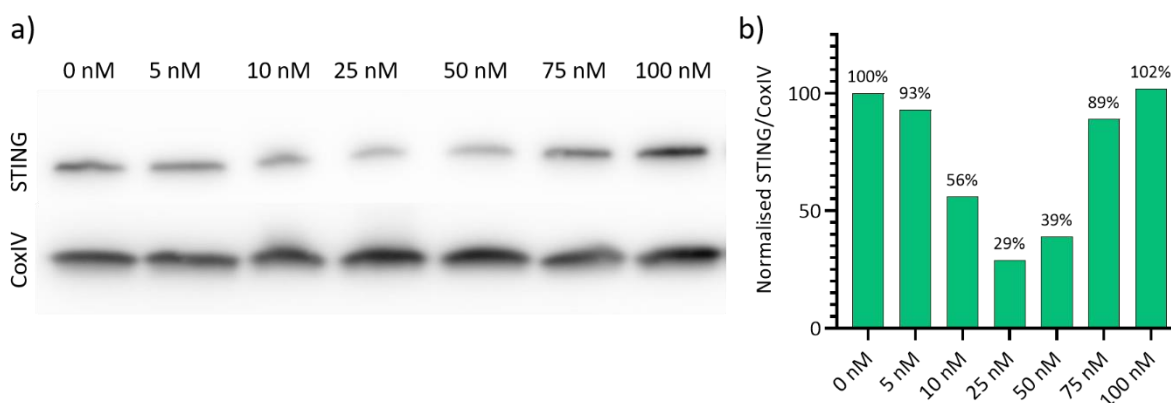
Figure 43: Concentration dependent STING degradation in THP-1 monocytic cells by PROTAC1.

The time needed for PROTAC1 entry and STING degradation are unknown factors, as well as the speed of STING recovery in the cells. To find out about the ideal time of incubation, 35 nM PROTAC1 was incubated for 4, 16 and 24 hours with THP-1 monocytic cells, followed by western blotting. Once again, the band intensities were quantified to provide numerical representations for this blot. Already after 4 hours a decrease of STING levels was observed. At 16 hours the STING levels reduced even more. The 24-hour time point was not observed with great success due to the lack of quality of the blotting.
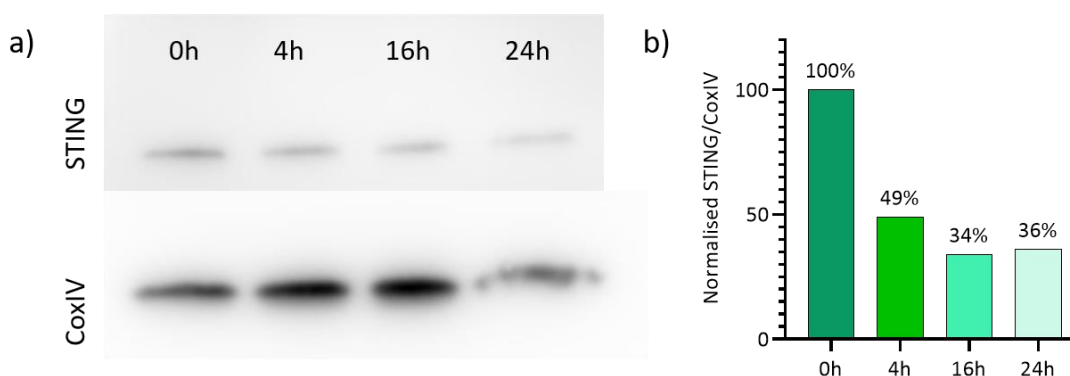
Figure 44: STING degradation in THP-1 monocytic cells by PROTAC1 over a time course.

3.4.3 Conclusion and Outlook

Overall, this section provides an insight of the great potentials for the PROTAC1. Both the structural design with the subunits of PROTAC1 and the PROTAC approach itself show very promising outcomes. STING degradation is proven to be enhanced by a PROTAC approach compared to known small molecule inhbitors[172,174]. Replicates of shown results need to be reproduced. Studies for toxicity and viability of the cells, changes of the interferon counts over longer periods, and the uptake efficiency of the PROTAC1 could be further studied. Moreover, the half-maximal inhibitory concentration (IC_{50}) needs to be calculated with more biological replicates. Small molecule STING inhibitors were developed for various purposes[170–174,238]. In

general, these inhibitors display an IC_{50} in the µM range and show room for improvement in terms of their pharmacokinetic qualities.

With a molecular weight at 1200 Da, the PROTAC1 belongs to the "beyond the rule of 5 (bRo5)" group of drugs[239,240]. The rule of 5 (Ro5), also called Lipinski's rule of 5, is used to describe drug-like properties of a compound which would determine its oral availability. One of the rules is concerning the molecular weight of the drug, which is described as preferable if it is below 500 Da. Up to this date, many applicable drugs exceeded this factor[239]. 50% of orally available drugs belong to bRo5, which indicates advancements for bigger molecules[240]. To make the PROTAC1 orally available might require some advancements concerning its pharmacokinetics. Since the linker of the STING recruiter contains a clickable site, different linker lengths, E3 ligase recruiters, and their combinations can be easily clicked to the STING recruiter. The approach to find the best combination of linker and recruiter, utilising click chemistry was adapted before to screen for stable ternary complexes and their relation to biological effectivity in terms of PROTAC development[241]. Taking advantage of the intense amount of research in this field, the choice of the E3 ligase recruiter can be diversified as well as the length of the linker.

4 Materials and Methods

Cell Culture THP1-Dual[TM] Cells:

THP1-Dual[TM] (Invivogen thpd-nfis) and THP1-Dual KO-STING[TM] (Invivogen thpd-kostg) cells were cultivated at 37°C in water saturated, 5% CO_2-enriched atmosphere (Heracell 150 CO_2 incubator) and handled under sterile conditions. The cells were cultured according to manufacturer's guidelines. RPMI 1640 (Sigma-Aldrich R0883) supplied with 20% (v/v) fetal bovine serum (FBS) (for ESC, Pan Biotech), 2 mM L-alanyl-L-glutamine (Sigma-Aldrich G8541), 1% (v/v) penicillin-streptomycin (Sigma-Aldrich P0781), 25 mM HEPES (Sigma-Aldrich H0887), 100 µg/mL Normocin[TM] (Invivogen ant-nr-1) was used as initial growth medium. After the recovery of the cells the FBS concentration was lowered to 10% (v/v) and 10 µg/mL of Blasticidin (Invivogen ant-bl) and 100 µg/mL of Zeocin[TM] (Invivogen ant-zn) were added freshly to the growth medium to maintain selection pressure when cells were passaged. The cells were kept between 0.4×10^6 cells/mL and 2×10^6 cells/mL, while the medium was changed every two days. The cells were cultured at tissue culture flasks (T25 and T75, Greiner/Sigma-Aldrich) laid horizontally to ensure for sufficient surface for gas exchange.

EC_{50} Measurements:

For the measurement of the activity of each STING agonist, around 0.125×10^6 cells and a range of concentrations from 0.1 nM up to 600µM of each compound were transferred in a well in 200 µL of total volume of test medium (growth medium without Blasticidin, Zeocin[TM], and Normocin[TM]) in 96-well plates. The concentration of each compound was measured before addition to the cells and was adjusted in serial dilutions with cell media. The compounds were added at a maximum volume of 10 µL on the cells to avoid fluctuations of the end concentration. The cells were incubated with the compounds for 24 hours. Media without any cells was used for background signal as well as untreated cells as negative control. After 24 hours, 20 µL of medium pipetted from the top of the wells was transferred in a well-plate with white opaque 96-wells (VWR Nunc), in technical duplicates or triplicates, and the luminescence signal was measured by a plate reader (TECAN Genious Pro) using luminescence measurement parameters according to Invivogen recommended protocols via the QUANTI-Luc[TM] reagent (Invivogen rep-qlc1). Accordingly, 25 µL of QUANTI-Luc[TM] was injected per well by the machine and the plate was shaken 2-5 seconds before each read-out for luminescence.

Stability in Human Serum:

The stability of the STING agonists against ENPP1 degradation were tested using human serum (Sigma-Aldrich H4522). 1 nmole of each agonist and natural cGAMP were incubated with 20 µL human serum and 50 µL reaction buffer, consisting of 20 mM Tris-HCl (pH 7.5), 1% NP-40, 150 mM KCl, 2 mM $MgCl_2$, 2 mM $CaCl_2$, 200 µM $ZnCl_2$, and a protease inhibitor, topped up to 100 µL end volume with ddH_2O (adapted from Eaglesham et al[99]). This reaction was set up for each individual time point, 0h, 1h,3h, 6h, 12h, 24h in the same tube. Each time point, 100 µL sample was collected to another tube in which the volume was topped up with ice-cold ddH_2O to 750 µL. The small molecule components of the reaction mix were extracted via addition of equal volumes of ice-cold acetonitrile. The mixture was incubated on ice for 15-20 minutes

and was centrifuged at 4°C at 14000 rpm for 10 minutes. The supernatant was transferred to a clean tube and was lyophilised. The dry product was resuspended in room-temperature ddH$_2$O and was extracted one more time with equal volumes of ice-cold acetonitrile to ensure the purity of the soluble pool. After lyophilisation the product was prepared for high resolution mass spectroscopy analysis.

Stability Against Poxins:

Vaccina virus (strain Western Reserve) treated BHK21 cell lysates were kindly provided by *S. Bauernfried* from the group of *Prof. Veit Hornung*. The cells were infected with 10 million PFU of VACV WR for 1 hour. After the infection, 14 hours post-incubation was provided before lysis and protein quantification. The lysis was done with 4mL 1% NP-40, 20 mM HEPES-NaOH pH 7.5, 150 mM NaCl, 1 mM TCEP-KOH for 15 minutes, following a 10-minute centrifugation at 1000g. The supernatant was collected for protein quantification. Continuing in S2 conditions, 450 ng of total protein lysate was incubated at 37°C in 150 µL reaction buffer containing 50 nM HEPES-KOH pH: 7.5, 35 nM KCl, 1 mM DTT (adapted from Eaglesham *et al*[99]) along with 5 µM compound. The reaction was prepared for time points 0h, 30 minutes, 1h, 3h, and 24h in the same tube. For each time point, 150 µL sample was ^{c}ollected to another tube and the reaction was stopped by the addition of 150 µL Roti-Phenol (phenol/chloroform/isoamyl alcohol; 25/24/1). The mixture was vortexed, spun down, and snap frozen to be stored at -80°C until further handling. The samples were then thawed on ice and the upper layer was transferred to a new tube and washed with equi-volume chloroform. The sample was vortexed at least 10 seconds and centrifuged for 1 minute at 14000 rpm. The upper layer was transferred into a clean tube and this process was repeated 2 more times. The last centrifugation step was 5 minutes to ensure complete separation of layers. The upper layer was taken to be lyophilised. The dry sample was then dissolved in 150 µL room temperature ddH$_2$O and the phenol chloroform extraction was repeated, to ensure a purification of the small molecules before submission to the high resolution mass spectroscopy.

Viability Assay:

For the viability assay, a standard MTT assay was used. 50.000 THP-1 Dual cells were aliquoted per well in 100 µL colourless test media (RPMI 1640 without phenol-red was used, Sigma Aldrich R8755). The cells were treated with light. For the viability test of 312 nm and 365 nm, light was shine for 0 min, 1 min, 3 min, 5 min, 10 min, and 20 min on three technical replicates, followed by a 24 h incubation. An untreated cell sample served as a positive control, whereas media without cells was taken for background measurements. As a negative control, DMSO was added on the cells with an end concentration of 10% to ensure cell death. The MTT reagent was added on the cells with an end concentration of 0.45-0.5 mg/mL (5 mg/mL MTT stock prepared in PBS), followed by an incubation of 3.5 hours. During this incubation time formazan crystals should form. 100 µL of solubilization solution (40% v/v DMF in 2% v/v glacial acetic acid with 16% w/v SDS) was added on the cells and crystals were dissolved by pipetting, avoiding bubble formation in the media. To ensure that there were no bubbles left, the cell

plate was spun down shortly. Absorbance was measured by a plate reader (Tecan Genius Pro) at 590 nm. The absorbance values were normalised by the untreated sample taken as 100% viable, whereas media containing no cells was taken 0% viable. The viability of the cells were calculated accordingly.

Cell Culture for PROTAC1:

1 million cells were cultured in 1,5 mL test media in 24-well plates. PROTAC1 was added on the cells with end-concentrations ranging from 0 nM to 100 nM. The concentration of added PROTAC1 was measured before each experiment and the volumes were adjusted by serial dilutions with test media, not to exceed 10 µL. After 16h of incubation for concentration optimisation and 4h, 16h, and 24h incubation for the incubation-time optimisation the cells were harvested.

Cell Harvest and Lysis:

Cells were harvested in about 150-250 g force for 3-4 minutes. The medium was discarded, the pellet was resuspended once in PBS and the cells were pelleted again. The PBS was discarded. Onto the pellet, 200 µL ice cold, freshly prepared RIPA buffer (50 mM Tris-HCl pH=8.0, 150 mM NaCl, 1% (w/v) NP-40, 0.5 % (w/v) Na-deoxycholate, 0.1 (w/v) % SDS, 1 mM PMSF) was added. The samples were put on a vertical shaker for 15 minutes at 4°C, then were centrifuged 10 minutes at 14000 rpm again at 4°C. The supernatant was transferred to a fresh tube.

Protein Quantification and Sample Preparation:

The samples were kept on ice at all times. They were diluted in ddH$_2$O if they were suspected to be too concentrated. The Pierce BCA Protein Assay Kit (Thermo Fischer Scientific, 23225) was used for quantifying protein amounts. The samples were then aliquoted for 20-30 µg of protein per condition, depending on the amount of protein in hand. The samples were incubated with 4x Laemmli Sample Buffer (250 mM Tris base pH=6.8, 20% (v/v) glycerol, 4% (w/v) SDS, 10% (v/v) beta-mercaptoethanol, 0.05% (w/v) bromophenol blue, in 25 mL ddH$_2$O end volume) for 5 mins at 95°C. At this step of sample preparation, the volume of the samples was not exceeding the maximum volume of the SDS-PAGE gel wells prepared.

SDS-PAGE Gel Preparation and Western Blotting:

SDS-PAGE gel was poured with a 10% Acrylamide resolving gel (7.9 mL ddH$_2$O, 6.7 mL Rotiphorese®Gel 30, 5mL of 1.5 M Tris pH=8.8, 200 µL of 10% SDS, 200 µL of 10% Ammonium persulfate in water, 20 µL TEMED, recipe for 4 gels) and a 5% Acrylamide stacking gel (5.5 mL ddH$_2$O, 1.3 mL Rotiphorese®Gel 30, 1 mL of 1 M Tris pH=6.8, 80 µL of 10% SDS, 80 µL of 10% Ammonium persulfate in water, 8 µL TEMED, reicpe for 8 mL). The samples were brought to room temperature and loaded on the gel, along with 7 µL of Colour Prestained Protein Standard, Broad Range (11-245 kDa, New England Biolabs P7719S) as reference. The gel was run in 1x SDS Running Buffer (25 mM Tris, 192 mM glycine, 0.1% (w/v) SDS) for 1 hour at 150 V. Afterwards, the gel was prepared and equilibrated in the cooled Towbin blotting buffer (25 mM Tris, 192 mM Glycine, 20% (v/v) methanol, 0.038% (w/v) SDS) along with sponges and the Whatman® gel blotting papers (Grade GB005, WHA10426981). A PVDF membrane

(Amersham™ Hybond®, pore size 0.45 μm) was used for blotting, which was activated in pure methanol for 1 minute before it was also equilibrated in the Towbin blotting buffer. The sandwich was assembled for western blotting (wet electro transfer) and was run for 90 minutes at 90 V at 4°C. After the transfer was completed, the PVDF membrane was first blocked for 1 hour with 5% (w/v) milk powder in TBS-T (20 mM Tris pH=7.5, 150 nM NaCl, 0.1 % (v/v) Tween-20) at room temperature. Afterwards, the membrane was cut along a horizontal line through the 26 kDa mark. The primary antibodies were applied separately in 5% (w/v) milk powder in TBS-T for 1 hour in room temperature, in the recommended ratios by the supplier, covering the membrane. The membrane was then washed three times for 10 minutes each with TBS-T to clear it from unbound primary antibodies. The secondary antibodies were applied as well in 5% (w/v) milk powder in TBS-T for 1 hour in room temperature, in the recommended ratios by the supplier. The membrane was then washed two times with TBS-T for 10 minutes each and one time with TBS (TBS-T without tween) for 15 minutes, to be then imaged with SuperSignal West Pico Chemiluminescent Substrate (Thermo Fischer Scientific 340077) in an Amersham Imager 680, in different manual modes depending on the intensities of the bands. All incubations after western blotting were done in a horizontal shaker to ensure equal distribution of the applied solutions and antibodies.

Antibodies:

STING antibody (Cell Signalling D2P2F #13647, rabbit monoclonal IgG): western blotting 1:2000

CoxIV antibody (Cell Signalling 3E11 #4850, rabbit monoclonal IgG): western blotting 1:2000

HRP-conjugated anti-rabbit IgG (Sigma-Aldrich A0545): western blotting 1:5000

ENPP1 antibody (Cell Signalling Human Specific #2070, rabbit monoclonal IgG): western blotting 1:1000

5 Published Work

5.1 "Chemical Synthesis of the Fluorescent, Cyclic Dinucleotides cthGAMP"

Simon Veth*, Adrian Fuchs*, Dilara Özdemir*, Dr. Clemens Dialer, Dr. David Jan Drexler, Fabian Knechtel, Dr. Gregor Witte, Prof. Karl-Peter Hopfner, Prof. Thomas Carell[*] and Dr. Evelyn Ploetz[*]

*: These authors contributed equally to this work.

Introduction and Summary

The cGAS-STING pathway detects cytosolic DNA and induces an innate immune response through the production of type I interferons. Due to the role of the cGAS-STING pathway in many disease-related processes including cancer and age-related diseases, therapeutic approaches are being developed with the focus on this pathway. Specifically, the step after the catalysis of cGAMP from an ATP and GTP provides an opportunity to interfere with the pathway by the development of modified cGAMP analogues. For assay development, a fluorescence-labelled cGAMP analogue would provide the opportunity for direct observations.

In this research article the chemical synthesis of two fluorescent cGAMP analogues is described which is adaptable to large scale synthesis. These analogues carry the thG base previously developed by the group of Yitzhak Tor[242]. The binding to murine and human STING of 2',3'-cthGAMP was measured and indicated stronger binding properties to human STING. The uptake of 2',3'-cthGAMP by THP-1 monocytic cells was successfully observed by two-photon imaging, inducing morphological changes and decreased brightness. Phasor analyses revealed cellular uptake by life-time imaging measurements upon 2',3'-cthGAMP addition. Furthermore, an increase of interferon production was observed upon 2',3'-cthGAMP transfection into THP-1 monocytic cells, providing proof of function at the cellular level.

Declaration of Contribution

In this work, I was responsible for the preparation and treatment of the cell samples. I optimised the preparation protocol of the samples for the fluorescence microscopy imaging. I treated the THP-1 cells in culture with the corresponding compound and immobilised the cells on PDL coated slides, followed by fixing and mounting of the samples. I transfected the THP-1 cells with the corresponding compounds and measured the increase of interferon production.

Authorization

Chemical Synthesis of the Fluorescent, Cyclic Dinucleotides cthGAMP

Simon Veth+,[a] Adrian Fuchs+,[a] Dilara Özdemir+,[a] Clemens Dialer,[a] David Jan Drexler,[b] Fabian Knechtel,[a] Gregor Witte,[b] Karl-Peter Hopfner,[b] Thomas Carell,*[a] and Evelyn Ploetz*[a]

The cGAS-STING pathway is known for its role in sensing cytosolic DNA introduced by a viral infection, bacterial invasion or tumorigenesis. Free DNA is recognized by the cyclic GMP-AMP synthase (cGAS) catalyzing the production of 2′,3′-cyclic guanosine monophosphate-adenosine monophosphate (2′,3′-cGAMP) in mammals. This cyclic dinucleotide acts as a second messenger, activating the stimulator of interferon genes (STING) that finally triggers the transcription of interferon genes and inflammatory cytokines. Due to the therapeutic potential of this pathway, both the production and the detection of cGAMP via fluorescent moieties for assay development is of great importance. Here, we introduce the paralleled synthetic access to the intrinsically fluorescent, cyclic dinucleotides 2′3′-cthGAMP and 3′3′-cthGAMP based on phosphoramidite and phosphate chemistry, adaptable for large scale synthesis. We examine their binding properties to murine and human STING and confirm biological activity including interferon induction by 2′3′-cthGAMP in THP-1 monocytes. Two-photon imaging revealed successful cellular uptake of 2′3′-cthGAMP in THP-1 cells.

Introduction

The innate immune system of eukaryotes is one of the first defense lines against invading pathogens.[1] To detect pathogens, the discrimination of molecular patterns from "self" (host) and "nonself" (e.g., microorganisms) is a fundamental process and relies on an array of pattern recognition receptors (PRRs). These PRRs are cell surface or intracellular receptors that distinguish pathogen-associated molecular patterns (PAMPs) from endogenous host patterns.[2] In addition to PAMPs, some PRRs recognize damage-associated molecular patterns (DAMPs) such as host-derived signals of cellular stress.[3] During the last decade, a cyclic dinucleotide (CDN) 2′,3′-cyclic guanosine mono-phosphate-adenosine monophosphate (2′3′-cGAMP, **1**) was identified to be crucially involved in transmitting innate immune system signaling (Figure 1a).[4]
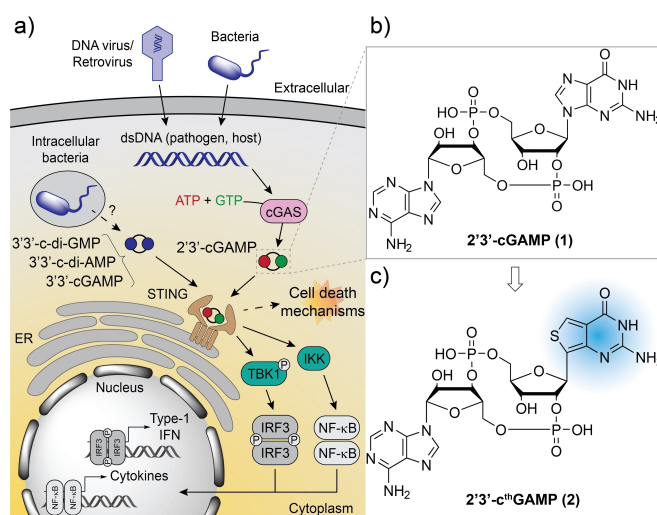
Figure 1. Biological role of CDNs. a) Molecular activation and regulation of the cGAS-cGAMP-STING pathway leading to interferon activation, inflammatory response and potential cell death. b) Structure of the CDN 2′3′-cGAMP. c) Chemical structure of the fluorescent analogue 2′3′-cthGAMP (**2**).

[a] S. Veth,+ A. Fuchs,+ D. Özdemir,+ Dr. C. Dialer, F. Knechtel, Prof. T. Carell, Dr. E. Ploetz
     Department of Chemistry and Center for NanoScience (CeNS)
     Ludwig-Maximilians-Universität München
     Butenandtstr. 5–13, 81377 Munich (Germany)
     E-mail: thomas.carell@cup.uni-muenchen.de
             evelyn.ploetz@cup.uni-muenchen.de
[b] Dr. D. J. Drexler, Dr. G. Witte, Prof. K.-P. Hopfner
     Gene Center and Department of Biochemistry
     Ludwig-Maximilians-Universität München
     Feodor-Lynen-Straße 25, 81377 Munich (Germany)
[+] These authors contributed equally to this work.

CDNs are found in vertebrates and prokaryotes alike and play an important role as second messengers.[5] While the CDNs from bacterial origin (e.g., 3′3′-c-di-GMP, 3′3′-c-di-AMP, 3′3′-cGAMP) are based on two canonical 3′-5′ phosphodiester bonds,[6] the only CDN found in mammalian cells possesses a mixed 2′-5′ and 3′-5′ phosphodiester linkage (2′3′-cGAMP).[4]

2′3′-cGAMP plays a crucial role in the cyclic GMP-AMP synthase (cGAS)-stimulator of interferon genes (STING) pathway, which has emerged as a critical mechanism for coupling the sensing of double-stranded DNA (dsDNA) in the cytosol to the induction of innate immune defense programs. cGAS, an

ChemBioChem

Research Article
doi.org/10.1002/cbic.202200005

Chemistry
Europe
European Chemical
Societies Publishing

enzyme belonging to the family of DNA sensors, recognizes a broad repertoire of DNA species of both foreign (e.g., pathogens) and self-origin.[7] Upon binding to dsDNA in the cytosol, cGAS from bacteria are sensed by STING at the endoplasmic reticulum (ER),[8] triggering a signaling cascade by recruiting the kinases TBK1 and IKK, which results in the activation of interferon regulatory factor 3 (IRF3) and NF-κB.[9] IRF3 and NF-κB consecutively induce the expression of type-1 interferons (IFN), inflammatory cytokines and other interferon-stimulated genes (ISGs),[10] leading to a DNA-driven immune response. Depending on signaling strength, STING also results in the activation of other cellular processes such as apoptosis and necroptosis.[11]

The modification of CDNs with fluorescently active moieties holds great promises for the development of novel activity assays and emissive probes for following these key compounds *in vivo*, in order to deepen our fundamental understanding on the life cycle of CDNs, including biosynthesis, distribution, and degradation or recycling. For instance, a fluorescently labeled ATP analogue based on 2-aminopurine (2AP) was used in the cGAS-catalyzed formation of a fluorescent CDN (fGAMP) to characterize the length-dependency of cGAS activity.[12]

Depending on the desired application a drawback of many emissive nucleoside analogues, including the most prevalently used 2AP, could be their significant quenching upon incorporation into oligonucleotides and CDNs.[13] The group of Yitzhak Tor developed a highly emissive RNA alphabet (thA, thG, thU, thC) with unparalleled structural isomorphicity to the native purine and pyrimidine bases derived from thieno[3,4-*d*]-pyrimidine as the heterocyclic nucleus. Besides excellent structural isomorphicity, good quantum yield ($\phi = 0.46$) and long excited-state lifetime (14.8 ns) were reported for thG in H_2O. Moreover, thG was found to show strong visible emission compared to 2AP even if "sandwiched" by two potential quenching guanosine residues in an oligonucleotide.[14]

In 2019, the enzymatic synthesis of a 2'3'-CDN bearing the thG base (2'3'-cthGAMP, **2**; Scheme 1) among 32 other CDNs was published focusing on the substrate specificity of cGAS derived from human, mouse and chicken as well as immunostimulatory properties in human peripheral blood mononuclear cells (PBMCs).[15] One year later, the enzymatic synthesis of thG-modified derivatives of bacterial 3'3'-c-di-GMP (3'3'-c-di-thGMP and 3'3'-c-thGGMP) were reported, highlighting their application in enzymatic assays and ability to induce a type-1 IFN response in THP-1 cells.[16] Cell experiments require large scales of the fluorescent, structural isomorph cGAMP mimics, which are hard to achieve by enzymatic pathways. To date, the organic synthesis of these compounds, as well as their application for cellular assays and fluorescent characterization *in vivo*, are missing.

Herein, we report the paralleled synthetic access to the cyclic dinucleotides 2'3'-cthGAMP and 3'3'-cthGAMP (Scheme 1) based on phosphoramidite and phosphate chemistry, suited for large scale synthesis. We highlight the differences in affinity of these CDNs to human and murine STING and focus on the scope and limitations of 2'3'-cthGAMP for *in vivo* studies in THP-1 cells using two-photon excitation microscopy.

Results and Discussion

Synthesis

The paralleled synthesis of 2'3'-cthGAMP (**2**) and 3'3'-cthGAMP (**3**) is depicted in Scheme 1. Starting from the 5'-dimethoxytrityl (DMTr)- and dimethylformamidino (dmf)-protected thG nucleoside **4** (for synthetic details see Shin et al.),[14] TBS-protection did yield a regioisomeric mixture of the 3'-OTBS (**5**) and 2'-OTBS (**6**) protected nucleosides. Following a modified procedure from Ching et al.,[17] these were converted to the corresponding phosphoramidites using commercially available 2-cyanoethyl *N,N,N',N'*-tetraisopropylphosphorodiamidite and pyridinium trifluoroacetate. The resulting 2'- and 3'-phosphoramidites were not isolated but instead the diisopropylamine functionality was directly displaced by allyl alcohol with the aid of 5-(benzylthio)-1*H*-tetrazole (BTT) activator followed by the *t*-BuOOH-mediated oxidation of the P(III)- to the P(V)-species and DMTr-deprotection in 3% dichloroacetic acid (DCA). In total, the four-step reaction sequence allowed to generate the allyl- and cyanoethyl-protected 2'-phosphate (**7**) and 3'-phosphate (**8**) in 56% yield. In a similar reaction sequence, commercially available DMT-2'-O-TBS-rA(Bz) phosphoramidite was then coupled to the free 5' OH groups of **7** and **8** with the aid of BTT activator, followed by oxidation and DMTr deprotection as described before. The resulting linear coupled dinucleotides were isolated in moderate yields, possessing the desired 2'3'- (**9**) and 3'3'- (**10**) connectivity. The deprotection of the allyl group with sodium iodide in refluxing acetone gave the alkoxides, which were cyclized using *N*-methylimidazole as nucleophilic catalyst, 2,4,6-triisopropylbenzenesulfonyl chloride (TPSCl) as condensing agent and molecular sieves (4 Å) as moisture scavenger to yield **11** and **12** in 49% yield over two steps. To minimize the formation of undesired side products by dimer formation, the cyclization reaction was carried out in dilute conditions (4 mM referred to starting material) to promote the intramolecular reaction. Treatment of **11** and **12** with a 1:1 mixture of ammonium hydroxide and methanol followed by triethylammonium fluoride resulted in the deprotection of the nucleobase protecting groups (dmf, Bz), β-cyanoethyl and silyl groups. After precipitation in cold acetone the resulting crude product was purified by reverse-phase HPLCs to separate and purify 2'3'-cthGAMP (**2**) and 3'3'-cthGAMP (**3**) in 13% yield for each CDN. The correct phosphodiester connectivity was NMR spectroscopically verified by ^{1}H-^{31}P-HMBC measurements (see Supporting Information).

Biochemical characterization

With both target compounds in hands, we focused on evaluating their binding properties to murine and human STING. At first, we employed differential scanning fluorimetry (DSF) to determine the binding affinity of synthetic and natural CDNs to STING proteins by evaluating the difference in melting temperature of the STING protein with and without ligand (Supporting Figure S5.1). While 2'3'-cthGAMP shows reduced

ChemBioChem

Research Article
doi.org/10.1002/cbic.202200005

**Chemistry
Europe**
European Chemical
Societies Publishing
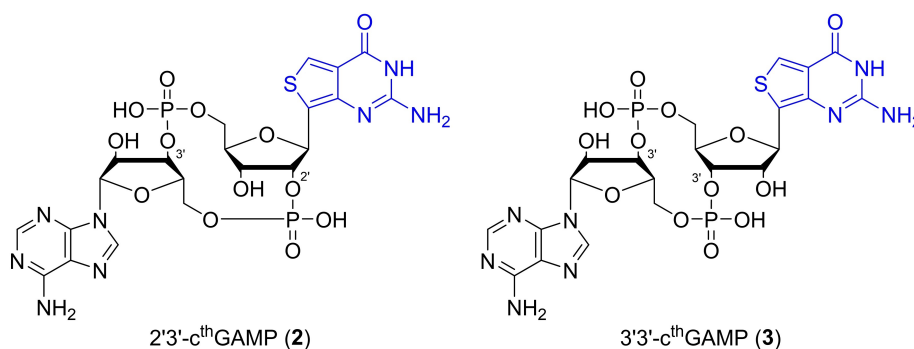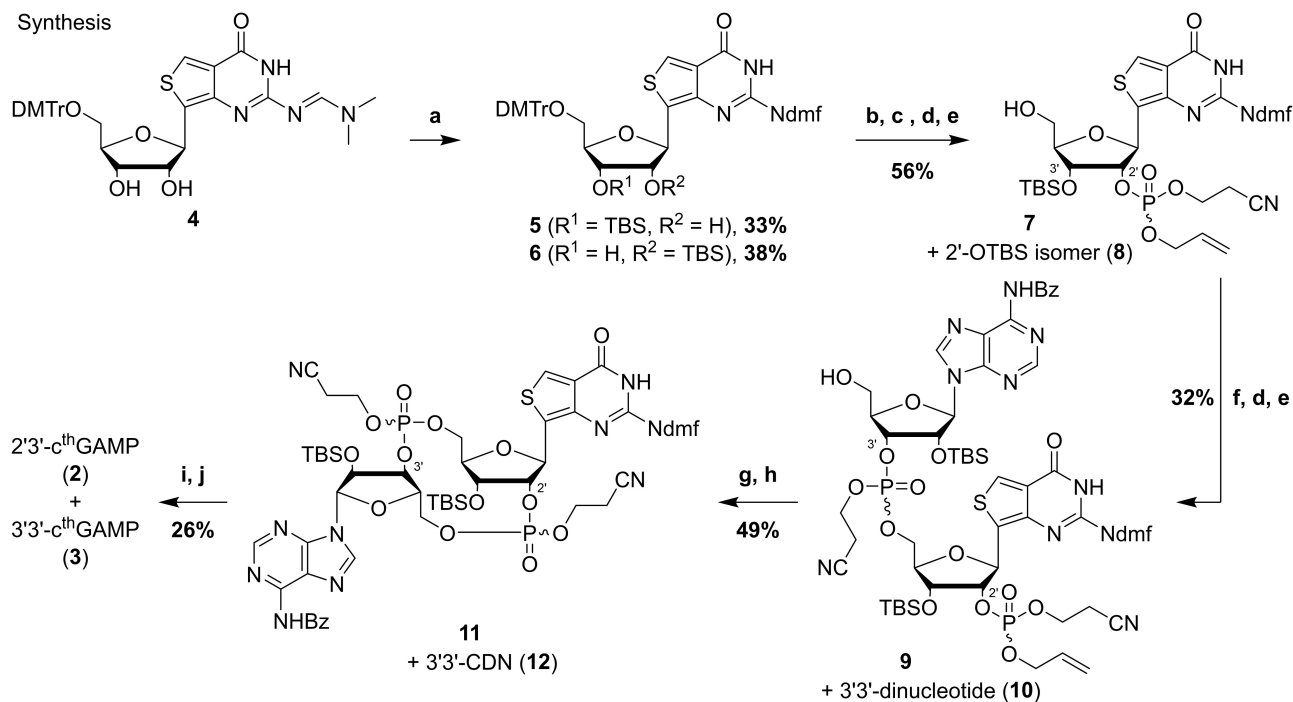
Scheme 1. Paralleled synthesis of 2'3'-cthGAMP and 3'3'-cthGAMP. Products 2'3'-cthGAMP (**2**) and 3'3'-cthGAMP (**3**) and synthetic overview. a) TBSCl, imidazole, pyridine; b) 2-cyanoethyl *N,N,N',N'*-tetraisopropylphosphorodiamidite, pyridinium trifluoroacetate, MeCN; c) BTT, allyl alcohol; d) *t*-BuOOH, then NaHSO₃; e) 3% DCA in DCM; f) DMT-2'-O-TBS-rA(Bz) phosphoramidite, BTT, MeCN; g) NaI, acetone; h) TPSCl, N–Me-imidazole, THF; i) NH₄OH, MeOH; j) NEt₃·3HF, THF, then HPLC.

binding-affinity compared to natural 2'3'-cGAMP, the thermal shift assays revealed, that 3'3'-cthGAMP (**3**) does not possess favorable binding affinity to neither murine nor human STING. As a consequence, we focused on the characterization and application of 2'3'-cthGAMP (**2**) in the later part of this publication.

Using isothermal titration calorimetry (ITC; Figure 2), we found that 2'3'-cthGAMP (**2**) is a less potent binder than natural 2'3'-cGAMP ($k_D = \sim 4$ nM).[18] It shows a 120- and 4000-fold reduced affinity to murine STING (mSTING; $k_D = 455$ nm) and human STING (hSTING; $k_D = 15$ μm). The thermodynamic parameters highlight, that the binding of 2'3'-cthGAMP to both receptors is exergonic ($\Delta G_{mSTING} = -36.3$ kJ/mol, $\Delta G_{hSTING} = -27.9$ kJ/mol), however with opposite trend for enthalpy and entropy: binding to mSTING is favorable in terms of entropy ($-T\Delta S_{mSTING} = -59.3$ kJ/mol) and endothermic ($\Delta H_{mSTING} = 23.4$ kJ/mol). In contrast, binding to hSTING was found to be
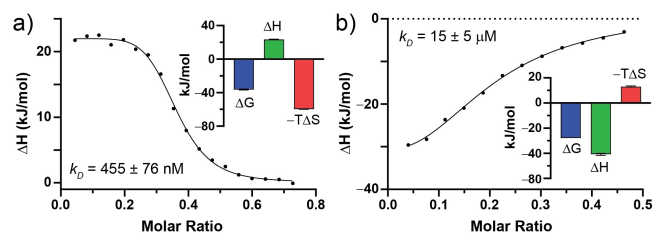
Figure 2. Binding to STING as measured by ITC. ITC curves and thermodynamic parameters for 2'3'-cthGAMP (**2**) bound to a) murine STING and b) human STING.

exothermic ($\Delta H_{hSTING} = -40.8$ kJ/mol) but entropically unfavorable ($-T\Delta S_{hSTING} = 13.1$ kJ/mol). Unlike the endothermic binding process of natural 2'3'-cGAMP to hSTING,[18] the data suggests that binding of 2'3'-cthGAMP might not trigger a full conforma-

ChemBioChem

Research Article
doi.org/10.1002/cbic.202200005

Chemistry
Europe
European Chemical
Societies Publishing

tional change in STING and, hence, a stabilized enclosure of the ligand. This observation would be in line with the reduced affinity of the synthetic compound.

Despite its reduced affinity, we set out next to investigate, whether binding of 2'3'-cthGAMP still activates STING signaling and consecutively interferon production. For this, we monitored the expression of the reporter gene Lucia luciferase in THP-1 Dual^{TM} wild type (THP-1 monocytes) cells, which is under the control of the ISG54 promoter in conjunction with five IRF-stimulated response elements. Secretion of luciferase and hence activation of the IFN pathway was quantified by monitoring its luminescence in response to 2'3'-cGAMP and 2'3'-cthGAMP after transfection. 2'3'-cthGAMP showed a ~5-fold reduced but significant IRF activation compared to the natural compound (Supporting Information Figure S2).

Uptake in THP-1 cells

Having verified the biological potency of 2'3'-cthGAMP, we continued with THP-1 monocyte cells and monitored the uptake and effect on immune cells by following the fluorescent signature of the synthetic molecule *in vivo*. As reported, the 2'3'-cthGAMP features a broad absorption in the UV below 360 nm with a maximum around 315 nm (Figure 3a). Being excited at 310 nm, a blue photoluminescence was observed. The emission spectrum has a width of more than 200 nm, starting around 380 nm upwards with an emission maximum around 470 nm (Figure 3a). Since excitation sources in the UV and blue spectral range cause high background when being used for imaging cells due to scattering and autofluorescence, we employed two-photon imaging[19] using a pulsed laser excitation at 774 nm (Supporting Information Figure S5.3a–b). The fluorescence emission of 2'3'-cthGAMP (**2**) in water between 400–650 nm clearly showed a quadratic dependence on the exciting laser power (Supporting Information Figure S5.3c) confirming the nonlinear nature of the two-photon excitation.

Figure 3b (upper panels) shows the emitted autofluorescence of two THP-1 Dual^{TM} cell lines, wild type (wt) and STING knock-out (STING KO), after two-photon excitation in the spectral range between 417 and 477 nm. Upon the addition of 2'3'-cthGAMP (**2**) to THP-1 wt cells, we expected an increase in overall brightness due to the intrinsic fluorescence of the compound. Instead, we observed a significant change in cell morphology combined with a strong decrease in emission (Figure 3c, upper panel, N = 91/129). In contrast, THP-1 STING-KO cells (Figure 3b, lower panel), which do not enter the consecutive immune response cascade, showed no morphological changes but only a slight swelling of the cell volume. Here, a significant increase in fluorescence intensity after 2'3'-cthGAMP uptake was monitored (Figure 3c, lower panel, N = 85/72). Both observations suggest, that 2'3'-cthGAMP is successfully taken up by both cell lines, however with different biological response: while cellular accumulation of 2'3'-cthGAMP leads to the expected brightness increase in THP-1 STING KO cells due to unavailability of the STING receptor and hence missing cellular response, the uptake in THP-1 wt cells triggered downstream
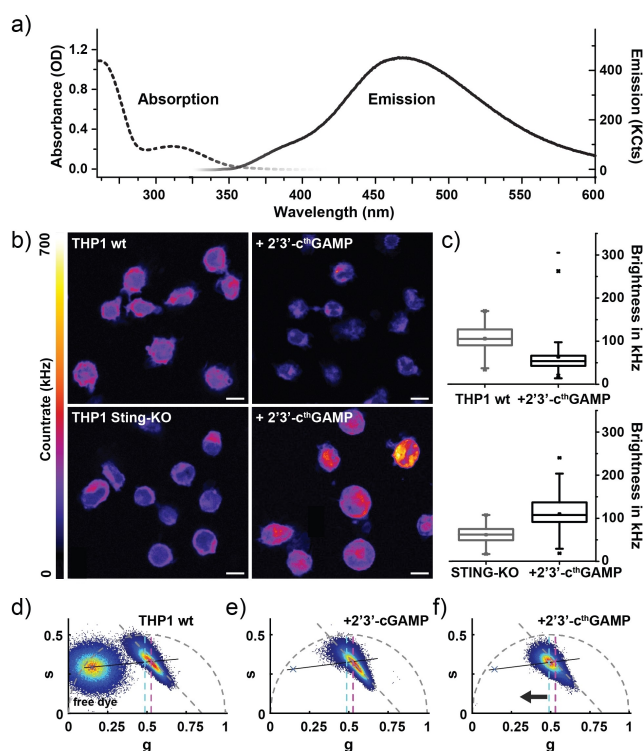
Figure 3. Fluorescence microscopy probing the cellular uptake of 2'3'-cthGAMP in THP-1 cells. a) Absorption (dotted line) and emission spectrum (solid line) of 52 µM 2'3'-cthGAMP in water after excitation at 310 nm. b-c) Two-photon images (b) and average cell brightness (c) of THP-1 wt cells (upper panel) and THP-1 STING-KO cells (lower panel) in absence and presence of 2'3'-cthGAMP. 2'3'-cthGAMP is biologically active in THP-1 wt cells leading to morphological changes and brightness decrease. In contrast, uptake of 2'3'-cthGAMP in STING knockout cells leads to a fluorescence increase. The emission was recorded between 417–477 nm and evaluated on average for 70–130 cells per condition. d–f) Phasor analysis of the average lifetime observed for THP-1 wt cells before (d) and after uptake of 50 µM 2'3'-cGAMP (e) and 200 µM 2'3'-cthGAMP (f). d) Phasor representation of the fluorescence signature of THP-1 wt cells and free 2'3'-cthGAMP in cell medium. The angled dotted line (grey) marks the multicomponent autofluorescent background in THP-1 wt cells. The center positions of the populations before (pink) and after (cyan) addition of 2'3'-cthGAMP (f) is marked with dotted lines. e) The addition of the non-fluorescent compound cGAMP triggers a shift in cellular autofluorescence towards shorter lifetimes and reduced brightness. f) The addition of 2'3'-cthGAMP leads to an off-axis shift towards free 2'3'-cthGAMP (along the black line), confirming the successful uptake.

processes due to activity of 2'3'-cthGAMP. Consecutive changes in cellular environment could affect the autofluorescent background, but also alter the photochemistry of the environmentally sensitive 2'3'-cthGAMP compound (see Supporting Information Figure S5.4.) by cellular interactions, leading to a decrease in fluorescence (if we anticipate the short time-window for free 2'3'-cthGAMP diffusion before binding to STING).

The autofluorescence signature of THP-1 overlaps with the emission spectrum of 2'3'-cthGAMP (**2**). To investigate whether the fluorescence increase observed for THP-1 STING KO cells can be directly linked to the uptake of 2'3'-cthGAMP (**2**), we evaluated the time-correlated single photon counting (TCSPC) data available for each image pixel in addition to the recorded

ChemBioChem

Research Article
doi.org/10.1002/cbic.202200005

Chemistry Europe
European Chemical
Societies Publishing

brightness information. At first, we recorded two-photon images of free dye only in solution for comparison and calibration (Supporting Information Figure S5.4a-b). By analyzing the exponential decay of the TCSPC histograms, we found an approximately mono-exponential behavior (on long time-scales) of 16.8 ns for 2'3'-c[th]GAMP in water, similar to [th]G in water (14.8 ns).[14] In buffers, however, we observed a shortened lifetime of 6.2 ns in PBS and even 4.3 ns in THP-1 cell medium (Supporting Information Figure S5.4a). Due to this complex behavior and the multi-exponential nature of cellular autofluorescence, we expanded the lifetime evaluation using the phasor approach[20], which graphically translates the fluorescence lifetime decay into Fourier space (see Supporting Information Note 4.4 for details). This technique enables the detection of small contributions to a multi-component lifetime mixture.[20a] Here, mono-exponential decays will be observed on an arc of radius 0.5 with long lifetime components near the origin (0,0), while short lifetimes are expected to contribute near (1,0). On the other side, multi-exponential decay pathways or fluorescence decays of mixed species are expected inside the circle. They are composed of weighted linear compositions of the contributing mono-exponential species along the arc and obtained by vectorial addition of the weighted contributions by each fluorescence species (Supporting Information Figure S4.2d–f).

When analyzing the TCSPC data by the phasor approach, 2'3'-c[th]GAMP in PBS and cell medium is characterized by a bi-exponential, long-lived lifetime lying close to the left half-circle (Supporting Information Figure S5.4b), compared to the single-exponential signature of Atto532 in PBS on the circle. For the uptake of the fluorescent 2'3'-c[th]GAMP into THP-1 cells, we expect a mix between the signature of the fluorescent analogue and the autofluorescence of the cell line. The uptake should be seen by a shift of the cellular autofluorescence signature towards the population of the free dye, while for the natural, non-fluorescent 2'3'-cGAMP no change should occur.

THP-1 wt cells show a short-lived, multi-exponential autofluorescence of about 1.85 ns. Their population lies in the right half-circle compared to the longer-lived signature of the free 2'3'-c[th]GAMP in cell medium (Figure 3d). The addition of the natural analog 2'3'-cGAMP to THP-1 cells triggers a change in morphology and autofluorescent background. This change is evident by a shift along the grey dotted line towards shorter lifetimes and concomitantly reduced brightness. Besides a decrease of the average lifetime from 1.85 to 1.75 ns (Figure 3e), no shift towards the free 2'3'-c[th]GAMP compound (along the black line) was observed. Upon addition of 2'3'-c[th]GAMP, however, a clear shift towards the free fluorescent analog is observed (Figure 3f), as marked for the center position of cellular autofluorescent in absence (pink) and presence of 2'3'-c[th]GAMP (cyan). The cellular uptake of 2'3'-c[th]GAMP leads to an increase in average lifetime (2.05 ns) although a simultaneous reduction in autofluorescence background and lifetime is observed. For the STING KO line an identical behavior was detected (Supporting Information Figure 5.4c). Both findings, the brightness increase (Figure 3c, lower panel) as well as the lifetime shift towards the pure compound (Figure 3f) give clear

evidence, that 2'3'-c[th]GAMP was taken up into THP-1 monocytes.

Conclusion

In summary, we report the first organic synthesis of 2'3'-c[th]GAMP (**2**) and 3'3'-c[th]GAMP (**3**), which feature the fluorescent [th]G base. The described synthetic strategy - involving phosphoramidite and phosphate chemistry - provides direct access to large quantities of both immunostimulants and enabled us to carry out cell feeding experiments with 2'3'-c[th]GAMP (**2**) as well as subsequent two-photon microscopy on THP-1 cells. While biochemical as well as cell-based assays confirmed the biologically activity of the synthetically derived compound, we further verified its presence in cells using fluorescence imaging and lifetime. Moreover, our observations show that the fluorescence lifetime of 2'3'-c[th]GAMP (**2**) is highly dependent on its environment suggesting a complex photochemistry for CDNs in general including the synthesized compound. While suitable for two-photon excitation microscopy, the cellular application of the fluorescent 2'3'-cGAMP analogue including intracellular tracking and downstream monitoring is strongly dependent on the autofluorescence of the chosen cell line, which creates an additional cell dependent detection limit. The decreased binding affinity of 2'3'-c[th]GAMP (**2**) to human STING in combination with high EC50 values[15] indicate substantial shortcomings which need to be addressed in the future. Nevertheless, as second messengers with diverse roles in both prokaryotes and eukaryotes, both fluorescent c[th]GAMP analogues may well serve for enzymatic assays/screening assays for inhibitors of CDN metabolism enzymes facilitating the development of therapeutics that target the cGAS-STING signaling pathway.

Experimental Section

Detailed experimental procedures during the synthesis and characterization of the fluorescent dinucleotides, protein purification of murine and human STING receptors, cell culturing, and advanced fluorescence microscopy are provided in the Supporting Information.

ChemBioChem

Research Article
doi.org/10.1002/cbic.202200005

**Chemistry
Europe**
European Chemical
Societies Publishing

Conflict of Interest

The authors declare no conflict of interest.

Data Availability Statement

The data that support the findings of this study are available from the corresponding author upon reasonable request.

[1] R. Medzhitov, C. A. Janeway, Jr., *Cell* **1997**, *91*, 295–298.

[2] S. Gordon, *Cell* **2002**, *111*, 927–930.

[3] K. Schroder, J. Tschopp, *Cell* **2010**, *140*, 821–832.

[4] A. Ablasser, M. Goldeck, T. Cavlar, T. Deimling, G. Witte, I. Röhl, K.-P. Hopfner, J. Ludwig, V. Hornung, *Nature* **2013**, *498*, 380–384.

[5] a) O. Danilchanka, J. J. Mekalanos, *Cell* **2013**, *154*, 962–970; b) L. Sun, J. Wu, F. Du, X. Chen, Z. Chen, *Science* **2013**, *339*, 786–791; c) U. Römling, M. Y. Galperin, M. Gomelsky, *Microbiol. Mol. Biol. Rev.* **2013**, *77*, 1–52.

[6] a) R. M. Corrigan, J. C. Abbott, H. Burhenne, V. Kaever, A. Gründling, *PLoS Path.* **2011**, *7*, e1002217; b) B. W. Davies, R. W. Bogard, T. S. Young, J. J. Mekalanos, *Cell* **2012**, *149*, 358–370; c) P. Ross, H. Weinhouse, Y. Aloni, D. Michaeli, P. Weinberger-Ohana, R. Mayer, S. Braun, E. de V-room, G. A. van der Marel, J. H. van Boom, M. Benziman, *Nature* **1987**, *325*, 279–281; d) G. Witte, S. Hartung, K. Büttner, K. P. Hopfner, *Mol. Cell* **2008**, *30*, 167–178.

[7] A. Decout, J. D. Katz, S. Venkatraman, A. Ablasser, *Nat. Rev. Immunol.* **2021**, *21*, 548–569.

[8] H. Ishikawa, G. N. Barber, *Nature* **2008**, *455*, 674.

[9] a) S. Liu, X. Cai, J. Wu, Q. Cong, X. Chen, T. Li, F. Du, J. Ren, Y.-T. Wu, N. V. Grishin, Z. J. Chen, *Science* **2015**, *347*, aaa2630; b) R. Fang, C. Wang, Q. Jiang, M. Lv, P. Gao, X. Yu, P. Mu, R. Zhang, S. Bi, J.-M. Feng, Z. Jiang, *J. Immunol.* **2017**, *199*, 3222.

[10] J. Wu, N. Dobbs, K. Yang, N. Yan, *Immunity* **2020**, *53*, 115–126.e115.

[11] a) M. F. Gulen, U. Koch, S. M. Haag, F. Schuler, L. Apetoh, A. Villunger, F. Radtke, A. Ablasser, *Nat. Commun.* **2017**, *8*, 427; b) J. Sarhan, B. C. Liu, H. I. Muendlein, C. G. Weindel, I. Smirnova, A. Y. Tang, V. Ilyukha, M. Sorokin, A. Buzdin, K. A. Fitzgerald, A. Poltorak, *Cell Death Differ.* **2019**, *26*, 332–347.

[12] L. Andreeva, B. Hiller, D. Kostrewa, C. Lässig, C. C. de Oliveira Mann, D. J. Drexler, A. Maiser, M. Gaidt, H. Leonhardt, V. Hornung, K.-P. Hopfner, *Nature* **2017**, *549*, 394.

[13] a) J. Zhou, Y. Zheng, B. T. Roembke, S. M. Robinson, C. Opoku-Temeng, D. A. Sayre, H. O. Sintim, *RSC Adv.* **2017**, *7*, 5421–5426; b) R. W. Sinkeldam, N. J. Greco, Y. Tor, *Chem. Rev.* **2010**, *110*, 2579–2619.

[14] D. Shin, R. W. Sinkeldam, Y. Tor, *J. Am. Chem. Soc.* **2011**, *133*, 14912–14915.

[15] B. Novotná, L. Vaneková, M. Zavřel, M. Buděšínský, M. Dejmek, M. Smola, O. Gutten, Z. A. Tehrani, M. Pimková Polidarová, A. Brázdová, R. Liboska, I. Štěpánek, Z. Vavřina, T. Jandušík, R. Nencka, L. Rulíšek, E. Bouřa, J. Brynda, O. Páv, G. Birkuš, *J. Med. Chem.* **2019**, *62*, 10676–10690.

[16] Y. Li, A. Fin, A. R. Rovira, Y. Su, A. B. Dippel, J. A. Valderrama, A. M. Riestra, V. Nizet, M. C. Hammond, Y. Tor, *ChemBioChem* **2020**, *21*, 2595–2598.

[17] S. M. Ching, W. J. Tan, K. L. Chua, Y. Lam, *Bioorg. Med. Chem.* **2010**, *18*, 6657–6665.

[18] X. Zhang, H. Shi, J. Wu, X. Zhang, L. Sun, C. Chen, Z. J. Chen, *Mol. Cell* **2013**, *51*, 226–235.

[19] A. Fuchs, P. Mannhardt, P. Hirschle, H. Wang, I. Zaytseva, Z. Ji, O. M. Yaghi, S. Wuttke, E. Ploetz, *Adv. Mater.* **2021**, *34*, 2104530.

[20] a) G. I. Redford, R. M. Clegg, *J. Fluoresc.* **2005**, *15*, 805; b) M. A. Digman, V. R. Caiolfa, M. Zamai, E. Gratton, *Biophys. J.* **2008**, *94*, L14-L16; c) G. Weber, *J. Phys. Chem.* **1981**, *85*, 949–953; d) D. M. Jameson, E. Gratton, R. D. Hall, *Appl. Spectrosc. Rev.* **1984**, *20*, 55–106.

5.2 "Redirected nuclear glutamate dehydrogenase supplies Tet3 with α-ketoglutarate in neurons"

Franziska R. Traube, Dilara Özdemir, Hanife Sahin, Constanze Scheel, Andrea F. Glück, Anna S. Geserich, Sabine Oganesian, Sarantos Kostidis, Katharina Iwan, René Rahimoff, Grazia Giorgio, Markus Müller, Fabio Spada, Martin Biel, Jürgen Cox, Martin Giera, Stylianos Michalakis and Thomas Carell

Introduction and Summary

Modifications on the canonical base cytosine provide an epigenetically regulated control over gene expression. Cytosine can be modified to 5'-methylcytosine, which is usually related to inactivation of genes. 5'-methylcytosine (mdC) can be modified further to 5'-hydroxymethylcytosine (hmdC), 5'-formylcytosine, and 5'-carboxylcytosine by the Ten-eleven-translocases (TET 1-3). The 5mC to 5hmC modification is related to activation of promoters, regulating transcription levels in neurons and embryonic stem cells. The reaction of TET enzymes require oxygen and α-ketoglutarate. α-ketoglutarate coordinates with the iron (FeII) center in TET enzymes generating an active Fe(IV)-oxo site which oxidates the methyl-group. 5hmC is most abundant in the brain in humans, specifically in neurons in the hippocampus where learning and memory functions require synapse formation.

The supply mechanism of the metabolite α-ketoglutarate to the site of action of TET3 is investigated in this research article in neurons. The mitochondrial enzyme glutamate dehydrogenase is translocated to the nucleus in hippocampal neurons to catalyse the NAD$^+$-dependent conversion of glutamate to α-ketoglutarate. This translocation doesn't occur in liver cells where there is no TET expression. In HEK293 cells, Gdh is only translocated o the nucleus when co-expressed with TET3. The proximity of Gdh and TET3 is required for the activity of TET3. When Gdh is expressed with a nuclear exporter sequence along with TET3 in HEK293 cells, a reduced conversion of mdC to hmdC and fdC is observed. In signalling neurons, Gdh activity is required for the conversion of mdC to hmdC by TET3. In hippocampal neurons, the Gdh/TET3 complex localises close to the Nuclear Pore Complex (NPC) on the nuclear envelope.

Declaration of Contribution

In this work, I performed the IHC/ICC experiments and Proximity Ligation Assays (PLA) and designed and cloned the Glud1-NES plasmid. I helped with the in vitro assays of TET3 and its optimisation. I helped with the depolarisation of hippocampal slices, DNA extraction and digestion, and western blots.

Authorization

Check for updates

Redirected nuclear glutamate dehydrogenase supplies Tet3 with α-ketoglutarate in neurons

Franziska R. Traube [1], Dilara Özdemir[1], Hanife Sahin[1], Constanze Scheel[2], Andrea F. Glück[1], Anna S. Geserich[2], Sabine Oganesian[1], Sarantos Kostidis [3], Katharina Iwan [1], René Rahimoff[1], Grazia Giorgio[2], Markus Müller [1], Fabio Spada [1], Martin Biel[2], Jürgen Cox [4], Martin Giera [3], Stylianos Michalakis [2,5 ✉] & Thomas Carell [1 ✉]

Tet3 is the main α-ketoglutarate (αKG)-dependent dioxygenase in neurons that converts 5-methyl-dC into 5-hydroxymethyl-dC and further on to 5-formyl- and 5-carboxy-dC. Neurons possess high levels of 5-hydroxymethyl-dC that further increase during neural activity to establish transcriptional plasticity required for learning and memory functions. How αKG, which is mainly generated in mitochondria as an intermediate of the tricarboxylic acid cycle, is made available in the nucleus has remained an unresolved question in the connection between metabolism and epigenetics. We show that in neurons the mitochondrial enzyme glutamate dehydrogenase, which converts glutamate into αKG in an NAD^+-dependent manner, is redirected to the nucleus by the αKG-consumer protein Tet3, suggesting on-site production of αKG. Further, glutamate dehydrogenase has a stimulatory effect on Tet3 demethylation activity in neurons, and neuronal activation increases the levels of αKG. Overall, the glutamate dehydrogenase-Tet3 interaction might have a role in epigenetic changes during neural plasticity.

[1] Department of Chemistry, Ludwig-Maximilians-Universität München, Munich, Germany. [2] Department of Pharmacy – Center for Drug Research, Ludwig-Maximilians-Universität München, Munich, Germany. [3] Leiden University Medical Center, Center for Proteomics and Metabolomics, Leiden, The Netherlands. [4] Computational Systems Biochemistry, Max Planck Institute of Biochemistry, Martinsried, Germany. [5] Department of Ophthalmology, University Hospital, LMU Munich, Munich, Germany. ✉email: michalakis@lmu.de; thomas.carell@lmu.de

Genomic DNA (gDNA) in higher vertebrates contains in addition to the four canonical nucleobases 5-methylcytosine (mdC), 5-hydroxymethylcytosine (hmdC), 5-formyl-cytosine (fdC), and 5-carboxy-cytosine (cadC)[1–3]. These cytosine (dC) derivatives give rise to an additional information layer that controls transcriptional activity[4]. The mdC-oxidation products hmdC, fdC, and cadC are generated by ten eleven translocation enzymes (Tet1-3), which are themselves α-ketoglutarate (αKG)- and oxygen-dependent dioxygenases (Fig. 1a). They decarboxylate αKG to generate an active site-bound Fe(IV)-oxo species that ultimately performs the oxidation[5]. Accumulating evidence suggests that mdC and hmdC directly affect transcriptional activity[6]. In contrast, fdC and cadC are considered as nucleobases that are exchanged with dC[7]. This exchange enables active demethylation that allows the system to switch between transcriptional states. While fdC and cadC are only present in trace amounts in differentiated cells, mdC and hmdC are detectable in all tissues[8]. Among all tissues, hmdC levels are by far the highest in brain[9,10], and in particular found in synapse-related genes of neurons[11]. This correlates with high Tet expression levels in neurons[12], further suggesting that dynamic oxidation-dependent active DNA demethylation is an essential prerequisite for neuronal plasticity[13,14]. The question of how neuronal nuclei are supplied with the required amounts of αKG is an unsolved question that couples mdC-oxidation chemistry in the genome to metabolism.

αKG is mainly generated in mitochondria as a key intermediate of the tricarboxylic acid (TCA) cycle[15]. The αKG levels outside the mitochondria vary substantially between cell types[16,17]. In differentiating cells this concentration was shown to be about 15 μM and the αKG availability was able to be linked to Tet activity with elevated αKG concentrations providing higher hmdC levels[16,18]. This indicates that αKG supply is indeed a Tet-activity limiting factor[16,18,19]. The principle that co-substrate availability in the nucleus determines the activity of epigenetic enzymes was already established in recent years for other epigenetic marks. Histone acetylation, for example, depends on acetyl-CoA. In neuronal nuclei, acetyl-coA is produced on-site by the acetate-dependent acetyl-CoA synthetase 2, which translocates from the cytosol to the nucleus[20]. In proliferating cells, acetyl-CoA is produced by the pyruvate dehydrogenase complex (PDC), which is shuttled from mitochondria into the nucleus[21]. This moonlighting of mitochondrial and cytosolic protein echoforms into the nucleus is a new principle that establishes the nucleus as a biosynthetically active entity[22] controlled by metabolic fluctuations that can differ substantially within the cell[23]. Here we show that neuronal Tet3 redirects the mitochondrial enzyme Gdh into the nucleus to establish an intranuclear production of αKG from NAD^+ and glutamate.

Results

Tet3 enzyme kinetics. All three Tet paralogues have functions in a neuronal context[14,24,25], but only the $Tet3^{-/-}$ phenotype is neonatal lethal in mice[26,27]. In humans, TET3 deficiencies were further recently linked to intellectual disabilities and growth retardation[28]. In order to compare the global expression levels of all three Tet enzymes in murine brain, a western blot was performed and the Tet expression levels in brain were compared to the levels in mouse embryonic stem cells (mESCs), which are known to have high Tet1, but low Tet3 levels[3]. The data depicted in Fig. 1b confirm that in accordance with literature[12], Tet3 is compared to Tet1 the dominantly expressed paralogue in brain. We next studied the affinity of Tet3 for αKG; again in comparison to Tet1 for which the enzyme kinetics were already studied in detail[3,29]. We expressed the catalytic domains of Tet1 and Tet3 as

N-terminal GFP-fusion constructs (GFP-Tet1cd and GFP-Tet3cd) in HEK293T cells and purified the proteins with anti-GFP nanobody-coated magnetic beads (Supplementary Fig. 1a). For the assay, we adjusted the amounts of added protein based on the GFP fluorescence. The bead-attached proteins were then used to oxidize a single-stranded DNA oligonucleotide substrate containing one central mdC base with increasing amounts of αKG (Fig. 1c). The DNA was subsequently purified and the conversion of mdC to the three oxidation products hmdC, fdC, and cadC was analyzed by matrix-assisted laser desorption ionization time of flight (MALDI-TOF) and quantified on the nucleoside level by UHPLC triple quadrupole (UHPLC-QQQ) mass spectrometry (MS). The MALDI data revealed that GFP-Tet3cd requires an approximately 20-fold higher αKG concentration than GFP-Tet1cd to reach a similar oxidation yield (Fig. 1c). Our UHPLC-QQQ-MS data revealed a Michaelis constant (K_m) of 39 μM αKG for GFP-Tet1cd, which is slightly lower than the previously reported K_m for Tet1[29]. For GFP-Tet3cd, the measured K_m was almost twofold higher at 73 μM αKG with a maximal conversion rate (v_{max}) only 15% compared to GFP-Tet1cd for (Supplementary Fig. 1b). In summary, the data suggest that Tet3, which is the dominantly expressed Tet paralogue in brain, has a particularly low affinity for αKG.

Gdh produces αKG co-substrate for Tet3 directly in neuronal nuclei. In order to search for Tet3 interaction partners that could provide αKG, we next performed an affinity-based proteomics study with nuclear lysate from whole murine brain. Prior to the study, we confirmed that the lysates showed specific enrichment of nuclear proteins (Supplementary Fig. 1c). For the initial co-immunoprecipitation (coIP), we overexpressed murine full-length Tet3 lacking the CXXC domain, which is the prevalent isoform in neuronal tissue[30], as an N-terminal GFP-fusion construct (GFP-Tet3) in HEK293T cells. The protein was then immobilized again on anti-GFP nanobody-coated beads (Supplementary Fig. 1d, e) and the beads were used as fishing baits for interacting proteins (Fig. 2a). Unfused GFP purified from the same source served as a negative control. By this approach we aimed to overcome the potential problem of antibody specificity, which may occur if two different antibodies—one for the actual coIP and one for the control coIP—are used. The samples were analyzed using label-free quantitative mass spectrometry (LFQ-MS)[31]. The statistical analysis of the data confirmed that the method provided highly reproducible datasets. The obtained data showed a high correlation within the replicates as determined by the Pearson correlation (Supplementary Fig. 2a). Particularly informative was the enrichment of O-linked-β-N-acetylglucosamine-transferase (Ogt) (Fig. 2b and Supplementary Fig. 2b). Because Ogt is a well-known Tet3 interactor[32–34], this finding was a first validation of the method. A search for other enriched proteins uncovered the mitochondrial enzyme glutamate dehydrogenase (Gdh), which catalyzes the NAD^+-dependent conversion of glutamate into αKG (Fig. 2c), as a Tet3 interactor (Fig. 2b and Supplementary Fig. 2b). Gdh is a key component of carbohydrate, amino acid, neurotransmitter and oxidative energy metabolism[35,36] and typically localizes to mitochondria[37]. The discovery of Gdh as a Tet3 interactor in nuclear lysate suggests an additional nuclear localization of Gdh.

Given the very high glutamate concentration in neurons, ranging from 5 to 10 mM[23], an on-site biosynthesis of αKG from glutamate by nuclear Gdh would establish a direct local co-substrate supply chain for Tet3. Gdh is a bidirectional enzyme that can also consume αKG. For this to occur, however, Gdh requires low glutamate concentrations and especially high levels of ammonium, which are known to be toxic for neurons[38,39]. To address the enzyme directionality, we measured the αKG-to-
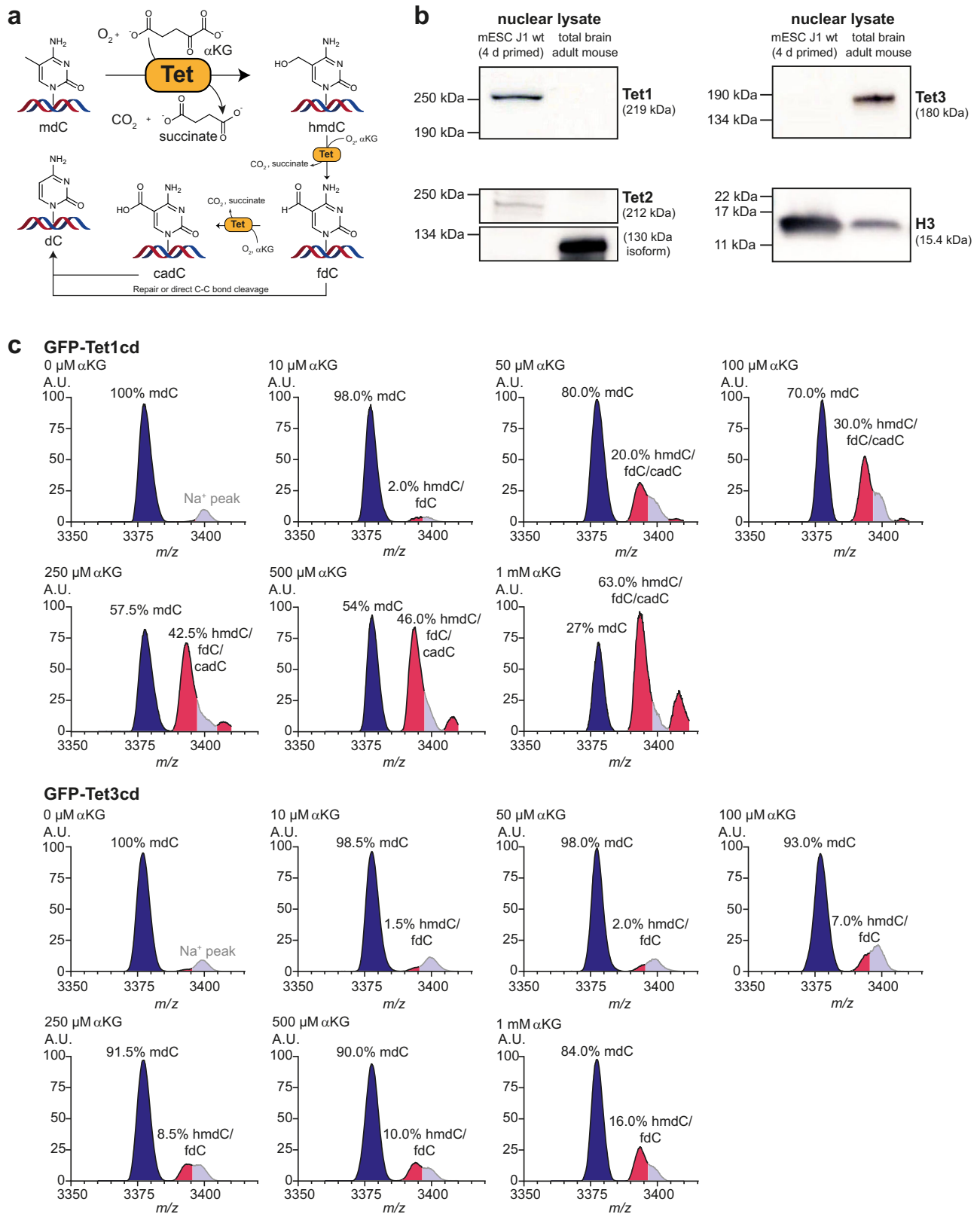
Fig. 1 Tet enzyme kinetics. a Illustration of αKG and O_2-dependent mdC-oxidation to hmdC and further on to fdC and cadC by Tet enzymes, with hmdC being the main oxidation product. FdC and cadC can be finally replaced by unmodified dC. **b** Western blots against Tet1, Tet2, and Tet3 in nuclear lysate of mESCs compared to murine brain. **c** MALDI-TOF MS spectra ($n = 3$ independent experiments, spectra show mean) of a single-stranded DNA oligonucleotide containing mdC (blue and Na^+ peak in gray) that is oxidized to hmdC, fdC, and cadC (magenta) by GFP-Tet1cd or GFP-Tet3cd in the presence of increasing αKG concentrations. A.U. arbitrary units, m/z mass to charge ratio. Source data are provided as a Source Data file.
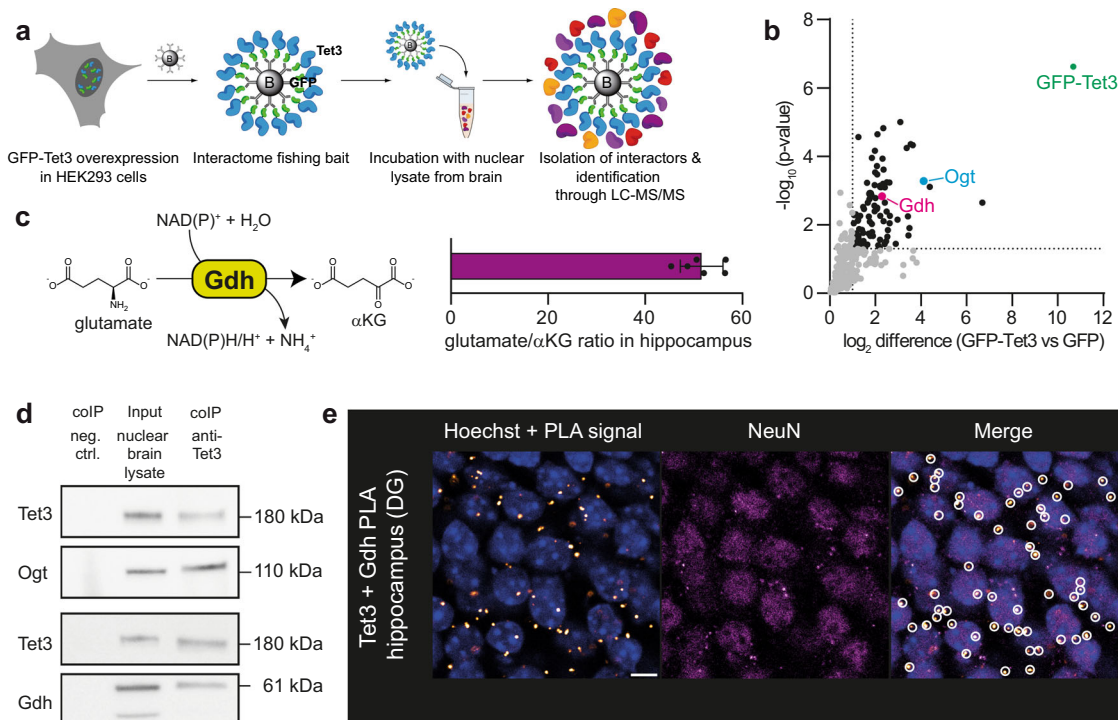
Fig. 2 Interaction of Tet3 with Gdh in neurons. a Experimental set-up for Tet3-enriched coIP. **b** Volcano plot after Tet3-enriched coIP in nuclear brain lysate of adult mice ($n = 4$ biologically independent sample preparations). Interaction partners were analyzed using label-free quantification after LC–MS/MS. Enriched interaction partners (FDR < 0.05, $\log_2$ FC > 1) are highlighted in black. **c** Conversion of glutamate to αKG by Gdh and glutamate to αKG ratio determined by NMR-based metabolomics in murine hippocampus ($n = 6$ biologically independent animals, bar shows mean, error bars SD). **d** Western blots detecting Tet3, Ogt, and Gdh after endogenous Tet3-coIP in nuclear brain lysate. **e** PLA signal (white/orange dots) of Tet3 and Gdh in the dentate gyrus (DG) of the murine hippocampus. Nuclei (blue) were stained with Hoechst and NeuN staining indicates neuronal nuclei. Scale bar is 5 μm. Source data are provided as a Source Data file.

glutamate ratio by NMR-based metabolomics[40] in hippocampus. We found that the glutamate levels are least 50 times higher than those for αKG (Fig. 2c). This finding in combination with the low ammonium levels in neurons[39] suggests that Gdh is operating in neuronal nuclei in the direction of αKG production, which is in line with previous reports about the function of Gdh in rat brain[41].

To substantiate the suspected interaction of Tet3 with Gdh, we immunoprecipitated endogenous Tet3 from nuclear brain lysate and analyzed the interaction partners by western blotting. The interaction of Tet3 with Ogt served again as a positive control. Importantly, Gdh was successfully pulled down in Tet3-endogenous coIP (Fig. 2d), confirming the result obtained by Tet3-enriched coIP. To further validate the interaction of Tet3 and Gdh in situ, we next performed a proximity ligation assay (PLA), which provides a signal only when the two investigated proteins are within a 40 nm distance[42]. For the study, we used coronal brain slices and antibodies that were validated before the experiment (Supplementary Fig. 3 and ref. [43]). Indeed, the Tet3/Gdh-PLA provided positive signals in hippocampal neurons (Fig. 2e and Supplementary Fig. 4a), further supporting a close proximity of Tet3 and Gdh in neuronal nuclei.

Gdh is transported with its MTS into neuronal nuclei. Gdh is known to be highly expressed in brain, which has high hmdC and Tet3 levels, as well as in liver, which has in contrast very low hmdC and Tet3 levels in a non-fasting state[9,12,41,44]. We investigated if the differences regarding the hmdC levels correlate with a different Gdh distribution. Using immunohistochemistry (IHC), we indeed found an exclusive mitochondrial localization for Gdh in hepatocytes. A specific Gdh signal in the nuclei of hepatocytes could not be detected and we failed to detect Tet3 (Fig. 3a and Supplementary Fig. 4b). In granule neurons of the

hippocampal dentate gyrus, however, we detected only very little Gdh in mitochondria. In contrast, Gdh was dominantly present in the nucleus. Tet3 was also detected with the expected nuclear localization (Fig. 3a and Supplementary Fig. 4b). Altogether, these immunofluorescence data revealed that Gdh exists in two echoforms of which one is situated inside mitochondria, while a second form can be transferred to the nucleus in neurons.

Next, we investigated the question of how Gdh can moonlight[22] into the nucleus. The gene *Glud1* encodes Gdh including an N-terminal 53 amino acids long mitochondrial-targeting sequence (MTS), which is cleaved off after import into the mitochondria[35,37]. When we analyzed neuronal Gdh in different subcellular compartments by western blotting, we found in the cytosolic fraction only the long variant with MTS migrating above the 57 kDa marker band, whereas in the organelle fraction only the short variant without MTS was detected (Fig. 3b). For the nuclear fraction, we detected two Gdh signals, with the dominant signal being at ~61.3 kDa and the weaker signal at ~55.9 kDa corresponding to two Gdh echoforms with and without the MTS, respectively. The weak band below 57 kDa that is detected in the nuclear fraction likely reflects some mitochondrial impurity, which is supported by a weak signal for CoxIV, which is a protein of the mitochondrial matrix. As the MTS is cleaved off after its import into mitochondria, detection of the short version in the organelle fraction was expected. The discovery of the long Gdh echoform in the nucleus suggests that the nuclear Gdh does not pass through the mitochondrion, but rather that it is directly transferred into the nucleus despite its MTS.

The Gdh-Tet3 proximity increases Tet3 activity. To study how the proximity of Tet3 and Gdh influences Tet3 function, we
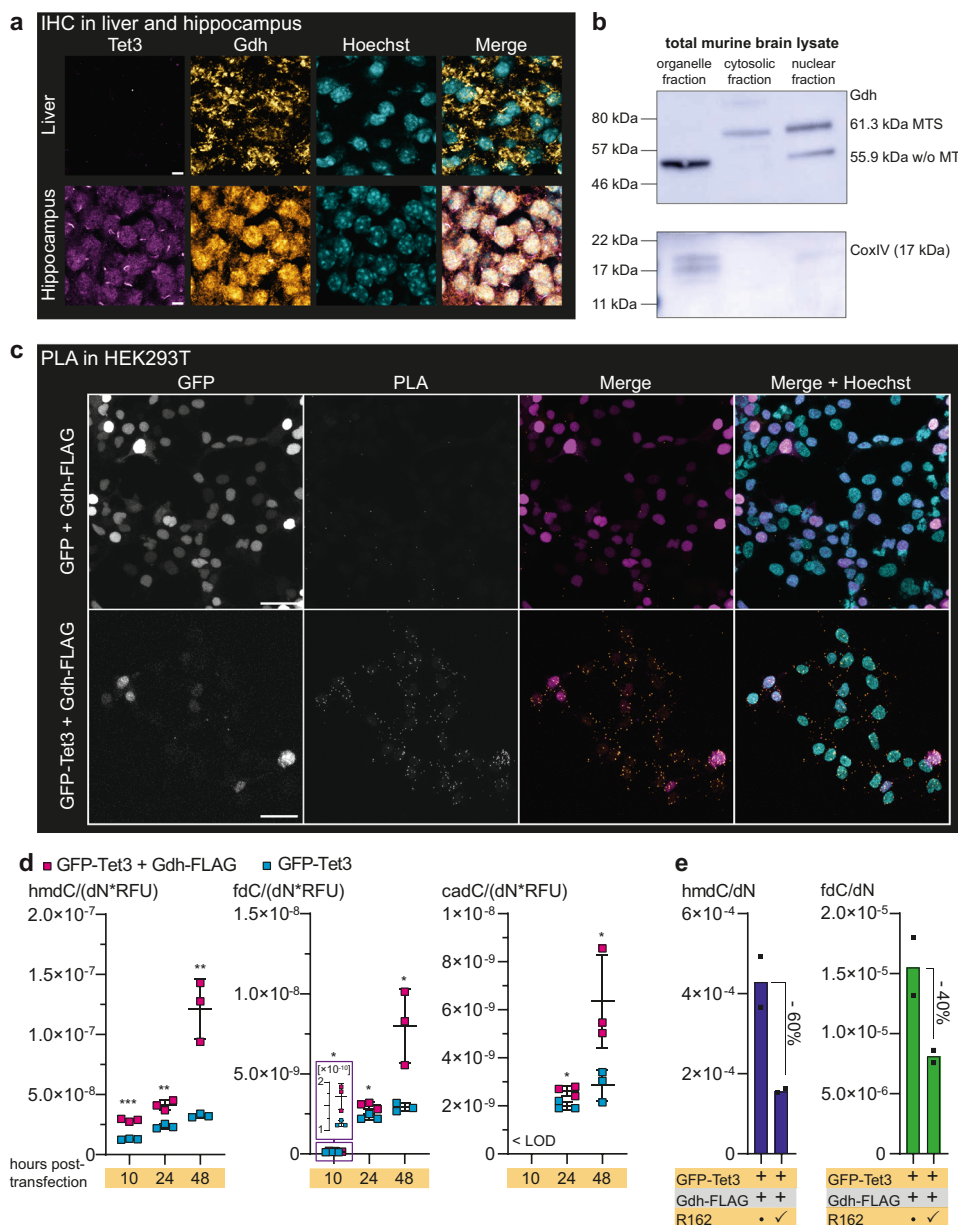
Fig. 3 Gdh localization in brain and liver and Tet3 + Gdh interaction after ectopic co-expression in HEK293T cells. a Immunofluorescence staining of Tet3 and Gdh in murine hippocampus compared to liver. Scale bar is 5 μm. **b** Western blot to determine Gdh content of different cellular compartments (fractionation from total murine brain) shows different echoforms of Gdh. CoxIV was used as a mitochondrial marker. **c** PLA in HEK293T after ectopic co-expression of GFP-Tet3 and Gdh-FLAG. GFP + Gdh-FLAG co-expressing cells were used as a negative control. In the merged image, GFP signal is shown in magenta, PLA signal in orange and nuclei (cyan) were stained with Hoechst. Scale bar is 50 μm. **d** Levels of hmdC, fdC, and cadC 10 h, 24 h, and 48 h after transfection of HEK293T ($n = 3$ biologically independent samples for each timepoint) with either GFP-Tet3 + Gdh-FLAG expressing plasmids (magenta) or GFP-Tet3 expression plasmid and an empty vector (cyan). Levels of mdC-oxidation products were normalized to the GFP signal of the cells. For each modification, each timepoint was compared individually. Two-sided t-test, correction for multiple comparisons using Holm-Sidak method, $p_{adj} < 0.05$ (*), < 0.01 (**), < 0.001 (***); exact p values and statistical details are provided in the Statistics and Reproducibility sub-section within the "Methods" section. Bars show mean, error bars show SD. LOD limit of detection **e** Levels of hmdC and fdC in the absence or presence of 20 μM of Gdh inhibitor R162 24 h after transfection of HEK293T ($n = 2$ biologically independent samples) with GFP-Tet3 and Gdh-FLAG expressing plasmids. **a**, **c** Images show Z-stacks. Source data are provided as a Source Data file.

performed a functional assay in HEK293T cells with ectopically co-expressed murine GFP-Tet3 and C-terminally FLAG-tagged murine Gdh (Gdh-FLAG). We first verified the interaction of GFP-Tet3 and Gdh-FLAG in HEK293T cells, again using a PLA with anti-GFP and anti-FLAG primary antibodies (Fig. 3c). While in the negative control, where unfused GFP and Gdh-FLAG were co-expressed, no PLA signal was detectable, co-expression of GFP-Tet3 and Gdh-FLAG provided clear PLA signals, indicating

that GFP-Tet3 and Gdh-FLAG were in close proximity in the nuclei of HEK293T cells. Next, we quantified the levels of hmdC, fdC, and cadC using our reported UHPLC-QQQ-MS method[45] at 10, 24, and 48 h post transfection in HEK293T cells that were either transfected with plasmids coding for GFP-Tet3 and Gdh-FLAG, or with the plasmid coding for GFP-Tet3 and an empty vector. In this model system, glutamate supply was guaranteed by the addition of 2 mM of L-alanyl-glutamine to the medium. To

correct for expression level differences of GFP-Tet3 between the samples, we normalized the hmdC, fdC, and cadC levels against the GFP signal (relative fluorescent unit (RFU)), which we determined using fluorescence-based flow cytometry (Supplementary Fig. 5a). For all modifications at any timepoint, the GFP-Tet3 + Gdh-FLAG co-expressing HEK293T cells showed significantly higher Tet-product levels than the cells expressing GFP-Tet3 alone (Fig. 3d). The largest difference was observed after 48 h, indicating that under limited nutrient and therefore limited αKG availability, additional αKG supply by Gdh enhances the Tet3 activity substantially.

To further investigate the stimulatory effect of Gdh activity on Tet3, we applied the previously published Gdh inhibitor R162 on the GFP-Tet3/Gdh-FLAG expressing cells. R162, which is a purpurin analog, was shown to be a highly specific Gdh inhibitor with an inhibition and a dissociation constant (K_i and K_d) of around $30\,\mu M$ and a good cell permeability due to its allyl group[46]. In the presence of R162, the hmdC levels dropped by 60% and the fdC levels dropped by 40% (Fig. 3e). Application of R162 did not decrease Tet3 activity in the cells expressing only GFP-Tet3 (Supplementary Fig. 5b), indicating that the endogenous (human) GDH does not contribute to the αKG supply of ectopically expressed murine Tet3.

In order to check how the proximity of Gdh and Tet3 influences Tet3 activity, we repeated the experiment with a Gdh-FLAG construct additionally containing a nuclear export sequence (Gdh-FLAG-NES), to prevent nuclear localization of Gdh (Supplementary Fig. 5c). We co-expressed Gdh-FLAG-NES with GFP-Tet3 and measured the hmdC and fdC levels compared to the GFP-Tet3/Gdh-FLAG expressing HEK293T cells. Twenty-four hours post transfection, the hmdC and fdC levels were significantly lower in the GFP-Tet3 + Gdh-FLAG-NES expressing cells (Fig. 4a). In addition, we were not able to mimic the effect of Gdh on Tet3 by the addition of 4 mM of cell-permeable dimethyl-αKG (DM-αKG) (Supplementary Fig. 5d), suggesting that the direct supply of Tet3 with αKG by Gdh in proximity is indeed enhancing Tet3 activity.

To clarify whether Gdh transport into the nucleus depends on Tet3, we next investigated the localization of Gdh in GFP-Tet3 + Gdh-FLAG and GFP + Gdh-FLAG expressing HEK293T cells using immunocytochemistry (ICC). Interestingly, when Gdh-FLAG was co-expressed with GFP-Tet3, Gdh-FLAG localization was ~40% nuclear and 60% mitochondrial (Fig. 4b and Supplementary Fig. 6a). GFP-Tet3 showed only the expected nuclear localization. In contrast, nuclear localization of Gdh-FLAG was abolished when it was co-expressed with GFP alone (Fig. 4b), indicating that the Gdh import into the nucleus is Tet3-dependent. We noted, however, that the expression of Tet3 and Gdh from two different promoters provided much higher Gdh levels than Tet3, which compromised interpretation of the data. Therefore, we repeated the experiment with a bicistronic vector including a T2A sequence that allowed for equimolar expression of FLAG$_3$-Tet3 and Gdh from the same promoter. Previous studies confirmed that ribosome skipping at the T2A is very efficient, so that only low amounts of fusion proteins are formed, and that this expression system does not change the localization of the expressed proteins[47,48]. Using this expression system, we first investigated the possible formation of Tet3-Gdh fusion proteins and found none by western blotting, whereas a forced Tet3-Gdh fusion protein using the bicistronic vector with a mutated T2A sequence (T2A$^{\Delta GP}$), which prevents the ribosome skipping event, showed a clear band at the expected size (Supplementary Fig. 6b). The following ICC studies revealed that in the presence of Tet3, Gdh was efficiently transported to the nucleus and only minor amounts of Gdh were detected in mitochondria. By comparison, the endogenous human GDH was only located in the mitochondria (Fig. 4c), which might explain

why the application of R162 did not change the Tet3 activity in the just GFP-Tet3 expressing cells. The forced Tet3-Gdh fusion protein did not locate to the nucleus but remained in the cytosol (Supplementary Fig. 6c). Altogether, the data support our model that the nuclear localization of Gdh requires the presence of Tet3 and suggests that Tet3 itself, or a complex of which Tet3 is part of, mediates transfer of Gdh into the nucleus.

Neuronal depolarization leads to Gdh-dependent stimulation of Tet enzymes. To transfer these findings from the HEK293T model system into a more physiological context, we exposed acute mouse hippocampal slices to depolarizing conditions (25 mM KCl), which simulate stimulation and induce neural activity[49]. After 6 h, we quantified the hmdC levels and compared them to the hmdC levels of hippocampal slices that were kept in parallel in a physiological buffer solution. Constant neuronal depolarization led to significantly increased global hmdC levels. In the presence of the Gdh inhibitor R162, however, this hmdC increase could be fully suppressed (Fig. 4d). Although off-target effects of the pharmacological small-molecule inhibitor R162 could not be fully excluded, previous publications gave no such indication[46]. Importantly, application of R162 allowed us to influence Gdh activity on the protein level directly and immediately. In contrast, siRNA-based approaches to knock-down Gdh expression by initiating Gdh-mRNA degradation do not affect Gdh activity directly and require transfection of siRNA, which might have comprised the quality of the sensible acute hippocampal slices.

As a reversed approach, we applied UK5099, which acts as an inhibitor of the mitochondrial pyruvate carrier and as a stimulator of Gdh[50]. In this experimental set-up, a further increase in the hmdC levels after stimulation was observed (Fig. 3d). These data suggest that Gdh is indeed involved in Tet-dependent hmdC generation upon neuronal activation.

Quantification of αKG in the hippocampal slices before and after depolarization supported this interpretation. We detected a strong increase of the αKG concentration and an increase of the αKG/succinate ratio under depolarizing conditions. In the presence of the Gdh inhibitor R162, however, the αKG amount dropped significantly, while the αKG/succinate levels were back at the basal level (Fig. 4e). These data suggest that a substantial amount of the αKG increase during neural activity is caused by the action of Gdh.

We wanted to explore whether the metabolic stimulation of Tet-activity affects the expression levels of important neuronal genes. Neuronal stimulation is known to affect the DNA methylation status of several genes that modulate the response of the neuron toward present and future stimuli[13,14]. Among those genes, the neuronal PAS-domain containing protein 4 (Npas4) and the brain-derived neurotrophic factor (Bdnf) play a pivotal role in synaptic homeostasis, learning and memory formation[51,52]. We used RT-qPCR to quantify the expression of Npas4 and Bdnf and observed for both genes reduced transcription during neuronal stimulation upon addition of R162 (Fig. 4f).

It is known that spatial organization of the nucleus has a direct impact on gene expression and that localization of a gene at the nuclear laminar is associated with gene silencing, whereas proximity to the nuclear pore complex (NPC) is linked to active gene expression[53]. Therefore, the gene-activating interaction of Tet3 and Gdh would be expected to proceed at the NPC. We noticed that a high number of Tet3 + Gdh-PLA signals in the hippocampus derived from the nuclear periphery (Fig. 2e). To test for the hypothesis that the interaction between Tet3 and Gdh happens at the NPC, we investigated the individual interactions of Tet3 and Gdh with the NPC by PLA. Indeed, in both cases, we obtained PLA signals supporting that the Tet3/Gdh complex is localized close to the NPC (Fig. 4g). In addition, proteomic
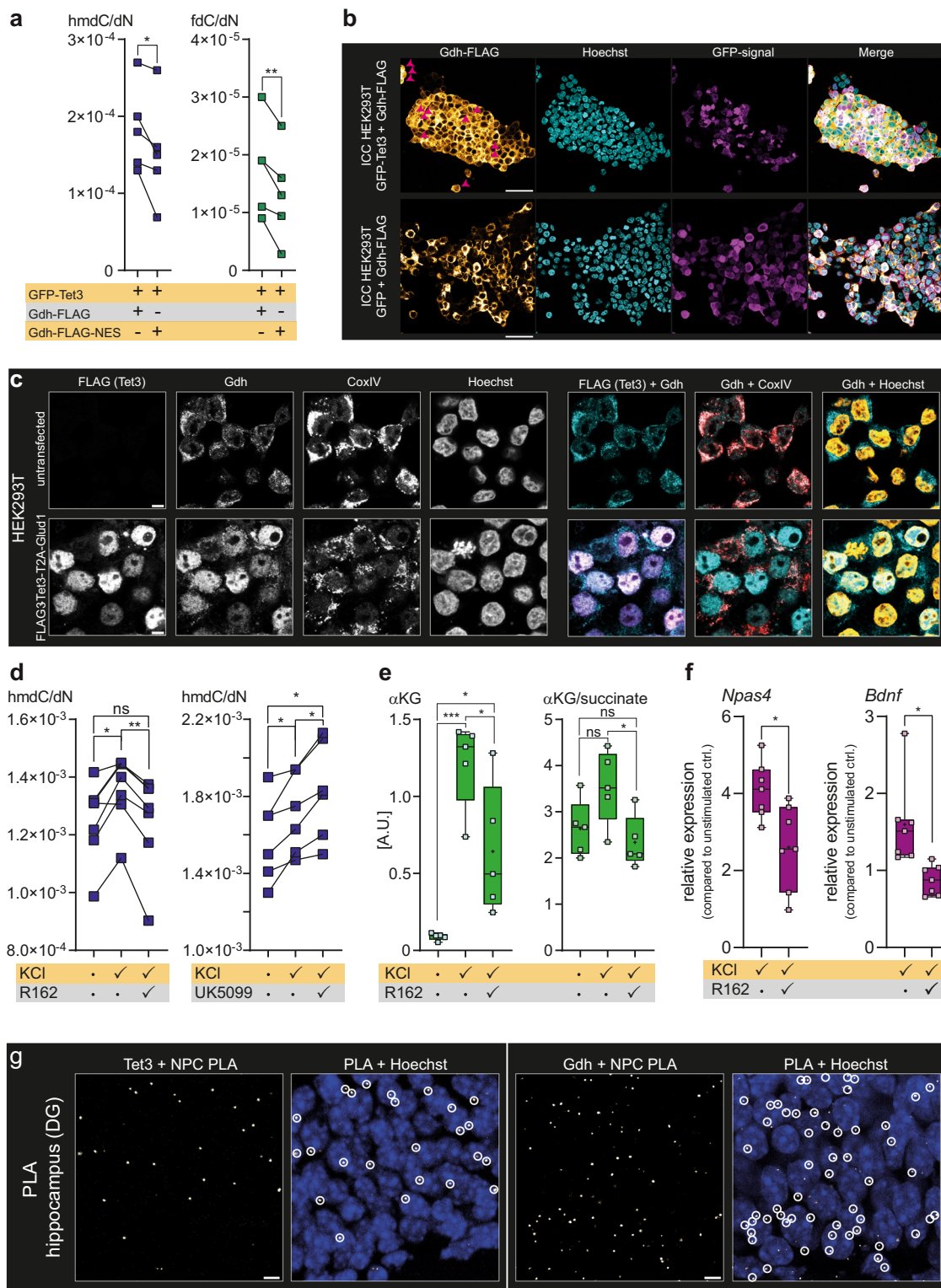
analysis of a Tet3-coIP in nuclear brain lysate showed enrichment of several RNA-processing proteins like Fus (Supplementary Fig. 2b), which is a DNA/RNA-binding protein that is important for pre-mRNA binding and transport and has distinct functions in neuronal homeostasis[54]. However, how the interaction of Tet3 and Gdh is organized within the nucleus and how this spatial organization is specifically linked to gene expression, needs to be addressed in future studies.

Altogether, our data support the idea that the interplay between nuclear Gdh for the NAD^+-dependent manufacturing of αKG and Tet3 is a hinge that allows metabolism to influence active demethylation processes in neurons. The mechanisms how the interaction of Tet3 and Gdh is regulated and whether Tet3 and Gdh interact indirectly or directly, potentially as part of a larger complex requires further investigation.

Discussion

Gdh is responsible for the NAD^+-dependent deamination of glutamate to αKG. Although it is known to be a mitochondrial enzyme and is expressed with an MTS, Gdh is reported to have an additional

Fig. 4 Gdh localization and influence of Gdh on Tet enzymes, gene expression and metabolism during neuronal stimulation. a Comparison of hmdC and fdC levels in HEK293T ($n = 5$ biologically independent samples) expressing GFP-Tet3 + Gdh-FLAG or GFP-Tet3 + Gdh-FLAG-NES for 24 h. A two-sided paired t-test was performed. **b** ICC in HEK239T showing FLAG and GFP signal after ectopic co-expression of GFP-Tet3 + Gdh-FLAG or GFP + Gdh-FLAG from different promoters. Scale bar is 50 μm. **c** ICC in HEK293T showing FLAG, Gdh, and CoxIV after expressing FLAG₃-Tet3 and Gdh from a bicistronic vector compared to untransfected cells. Merged images: FLAG (magenta), Gdh (cyan), CoxIV (red) and Hoechst (yellow). Scale bar is 5 μm. **d** Hippocampal hmdC levels upon neuronal stimulation with 25 mM KCl for 6 h with and without 20 μM Gdh inhibitor R162 ($n = 7$ biologically independent animals) or 40 μM PDC inhibitor UK5099 ($n = 6$ biologically independent animals). Connected dots represent matched hmdC values from one individual mouse. RM one-way ANOVA combined with Tukey's multiple comparisons test was performed. **e** αKG level and αKG/succinate ratio in hippocampus ($n = 5$ biologically independent animals) after depolarization with and without R162. Ordinary one-way ANOVA combined with Tukey's multiple comparisons test was performed. A.U. arbitrary units. **f** Relative gene expression levels of Npas4 and Bdnf ($n = 7$ biologically independent animals) in hippocampus after depolarization with and without R162 normalized to expression levels in unstimulated control. An unpaired two-sided t-test with Welch's correction was performed. **g** PLA of Tet3 + NPC and Gdh + NPC in the hippocampus. Images show Z-stacks. Scale bar is 5 μm. **a**, **d**–**f** p (a, f) or $p_{(adj)}$ (**d**, **e**) <0.05 (*), <0.01 (**), <0.001 (***); exact p values and statistical details are provided in the Statistics and Reproducibility sub-section within the "Methods" section. **e**, **f** Boxes display interquartile range, median is shown as center line, mean as +, whiskers represent the minimum and the maximum. Source data are provided as a Source Data file.

nuclear localization in neural contexts[35,37,55]. Our data confirm that neuronal Gdh has indeed a split spatial distribution with a substantial fraction of the protein being redirected to the nucleus, probably before entering the mitochondria. In neurons, glutamate is one of the most abundant metabolites making it in this respect an ideal starting material for the generation of large amounts of αKG. Our data suggest that one of the functions of Gdh in the nucleus is to supply Tet3 with αKG, thereby regulating Tet3-activity. Given that αKG is involved in many epigenetic processes and energy metabolism in general[15], elevating the effective αKG molarity solely in the presence of Tet3 is an elegant way to avoid globally changing αKG levels, which could produce various side effects. This puts Gdh in line with other mitochondrial proteins, such as the PDC or enzymes of the TCA cycle that can be also translocated to the nucleus for controlled intranuclear metabolite biosynthesis and consequently metabolic regulation of gene expression by changing histone modifications[21,56]. Our data expand this coupling between metabolism and epigenetics to the Tet-dependent oxidation of mdC to hmdC and likely further on to fdC and cadC. Since Gdh requires NAD⁺ for the conversion of glutamate into αKG, these oxidation reactions are seemingly associated with the NAD⁺ levels in the nucleus. NAD⁺ is an essential small-molecule cofactor that is biosynthesized in a compartmentalized manner by different nicotinamide mononucleotide adenylyl transferases (NMNATs) in the nucleus (NMNAT-1), in the cytoplasm (NMNAT-2) and in mitochondria (NMNAT-3)[57]. It was recently shown that the nuclear NAD⁺ levels fluctuate depending on the metabolic state of the cell and it was suggested that the compartmentalized NAD⁺ biosynthesis plays a key role in controlling transcriptional processes[58]. Although we are far from understanding how a shift in energy and NAD⁺ metabolism leads to the controlled activation of specific genes, our data suggest that nuclear localized Gdh for the NAD⁺-dependent on-site biosynthesis of αKG to steer Tet3 activity, can be an important contributor and regulator.

Methods

All procedures concerning animals conform to the German animal protection laws and were approved by the local authority (Regierung von Oberbayern).

Antibodies. CoxIV antibody (Cell Signaling Technology brain-derived neurotrophic fact4850, clone 3E11, rabbit monoclonal IgG): western blotting (1:1000), ICC (1:500)

Cytochrome C antibody (Santa Cruz Biotechnology sc-13560, clone 7H8, mouse monoclonal IgG): western blotting (1:1000)

FLAG antibody (Sigma-Aldrich F1804, clone M2, mouse monoclonal IgG): western blotting (1:2000), ICC (1:500)

FLAG antibody (Sigma-Aldrich F2555, clone SIG1-25, rabbit monoclonal IgG): PLA (1:250)

Gdh antibody (Invitrogen PA5-19267, goat polyclonal IgG, Lot #74422112, P1): western blotting (1:1000 – 1:2000), ICC (1:100 – 1:200), IHC (1:100)
Validation:

- Western blotting: signal at 56 kDa for haploid mESC, no signal for haploid mESC^Glud1 -/ (Supplementary Fig. 3d)
- ICC: strong signal for haploid mESC, no signal for haploid mESC^Glud1 -/ (Supplementary Fig. 3d)

GFP antibody (Cell Signaling Technology 2955, clone 4B10, mouse monoclonal): western blotting (1:1000), PLA (1:200)

Histone H3 antibody (Cell Signaling Technology 4499 S, clone D1H2, rabbit monoclonal IgG): western blotting 1:1000

NeuN antibody (EMD Millipore MAB377X, clone A60, Alexa488 conjugated, mouse monoclonal IgG): IHC (1:100)

NPC antibody (Sigma-Aldrich N8786, clone 414, mouse monoclonal IgG): IHC (1:250)

Ogt antibody (Invitrogen PA5-22071, rabbit polyclonal IgG, Lot #RH2258725): western blotting (1:1000)

Tet1 antibody (Active Motif 61741, clone 5D6, rat monoclonal IgG): western blotting (1:1000)
Validation:

- Western blotting: one strong signal above 200 kDa for mESC, but not for mESC TET triple knockout (TKO) cells (Supplementary Fig. 7)

Tet2 antibody (ptglab 21207-1-AP, rabbit polyclonal IgG): western blotting (1:1000)
Validation:

- Western blotting: a strong signal at the expected 212 kDa for mESC and at 130 kDa for murine brain, but not for mESC TET TKO cells (Supplementary Fig. 7)

Tet3 antibody (Abiocode N1 R1092-1, rabbit polyclonal IgG, Lot #7063 and #9013):
western blotting (1:1000), coIP (2 μg), ICC (1:500), IHC (1:500)
Validation:

- Western blotting: one strong signal at ~180 kDa for nuclear brain lysate, but not for mESC TET TKO cells (Supplementary Fig. 3a)
- ICC: total signal overlap with GFP in GFP-Tet3 transfected HEK293T, but not with GFP in GFP only transfected HEK293T (Supplementary Fig. 3b)
- ICC: no signal in mESC TET TKO (Supplementary Fig. 3c)
- IP: validation for IP has already been reported[43]

β-Tubulin antibody (Cell Signaling Technology 2128, clone 9F3, rabbit monoclonal IgG): western blotting (1:1000)

Secondary antibodies. Anti-goat IgG (Sigma-Aldrich G4018, rabbit polyclonal): IP (1 μg for MS analysis, 2 μg for western blot analysis)

Cy2-anti-goat IgG (Jackson ImmunoResearch 705-225-147): IHC (1:200)
Cy3-anti-goat IgG (Jackson ImmunoResearch 805-165-180): IHC (1:400)
HRP-conjugated anti-goat IgG (Sigma-Aldrich A5420): western blotting (1:5000)

Alexa488-anti-mouse IgG (Cell Signaling Technologies 4408): IHC (1:800)
Alexa555-anti-mouse IgG (Cell Signaling Technologies 4409): IHC (1:800)
HRP-conjugated anti-mouse IgG (Sigma-Aldrich AP130P): western blotting (1:5000)

Cy3-anti-mouse IgG (Jackson ImmunoResearch 715-165-150): IHC (1:400)
Alexa488-anti-rabbit IgG (Cell Signaling Technologies 4412): IHC (1:800)
Alexa555-anti-rabbit IgG (Cell Signaling Technologies 4413): IHC (1:800)
Cy3-anti-rabbit IgG (Jackson ImmunoResearch 711-165-152): IHC (1:400)
HRP-conjugated anti-rabbit IgG (Sigma-Aldrich A0545): western blotting (1:5000)

Expression plasmids. GFP-Tet1cd (plasmid with ampicillin resistance, CAG promoter[59]):

Expressed protein (N-terminus) eGFP—TEV cleavage site—Tet1cd (C-terminus); Tet1cd is the shortened version of murine Tet1 (NCBI XP_006513930.1) starting from amino acid 1367 of the original sequence, TEV cleavage site ENLYFQ|G

GFP-Tet3cd (plasmid with ampicillin resistance, CAG promoter):

Expressed protein (N-terminus) eGFP—TEV cleavage site—Tet3cd (C-terminus); Tet3cd is the shortened version of murine Tet3 (NCBI NP_001334242.1) starting from amino acid 696 of the original sequence

GFP-Tet3 (plasmid with ampicillin resistance, CAG promoter[59]):

Expressed protein (N-terminus) eGFP—TEV cleavage site—Tet3; murine Tet3 (NP_898961.2) starting from amino acid 1 of the original sequence

Glud1-FLAG (plasmid with ampicillin resistance, CMV promoter):

Expressed protein (N-terminus) Gdh-FLAG (C-terminus); murine Glud1 (UniProtKB – P26443) starting from amino acid 1 of the original sequence, FLAG DYKDDDDK

Glud1-FLAG-NES (plasmid with ampicillin resistance, CMV promoter):
Expressed protein (N-terminus) Gdh-FLAG-NES (C-terminus); NES GS**LALKLAGLDI**[60]

FLAG₃-Tet3-T2A-Glud1 (plasmid with ampicillin resistance, promoter TRE):
Expressed proteins (N-terminus) Strep-FLAG₃ - TEV cleavage site - Tet3 (C-terminus) and Gdh

FLAG₃-Tet3-T2A^ΔGP-Glud1 (plasmid with ampicillin resistance, promoter TRE):

Expressed protein (N-terminus) Strep-FLAG₃ - TEV cleavage site -Tet3-Gdh (C-terminus)

Chemical structures. Chemical structures were drawn using ChemDraw Professional 16.0.

Cell culture HEK293T cells. HEK293T cells (ATCC) were cultivated at 37 °C in water saturated, CO_2-enriched (5%) atmosphere. DMEM (Sigma-Aldrich D6546) or RPMI 1640 (Sigma-Aldrich R0883), containing 10% (v/v) fetal bovine serum (Invitrogen 10500-064), 1% (v/v) L-alanyl-L-glutamine (Sigma-Aldrich G8541), and 1% (v/v) penicillin–streptomycin (Sigma-Aldrich P0781), were used as growing medium. When reaching a confluence of 70–80%, the cells were routinely passaged. Cells were tested at least once in 2 months for Mycoplasma contamination using Mycoplasma Detection Kit (JenaBioscience PP-401L).

Transfection of HEK293T cells

Transfection of HEK293T cells for high protein expression. The transfection was performed in four p150 petri dishes (Sarstedt 83.3903.300). Five to six million cells per p150 were seeded in 25 mL of medium. After seeding, the cells were incubated for 24 h to reach a confluence of 40–80%. Ten micrograms of expression plasmid DNA and 30 μL of the transfection reagent jetPRIME (Polyplus Transfection VWR 114-15) were used as described by the manufacturer. Four hours and 28 h after transfection the medium was changed, and sodium butyrate (final conc. 4 mM) was added. Forty-eight hours after transfection, the cells were harvested by trypsinization and immediately used for protein extract preparation.

Transfection of HEK293T cells for ICC. The transfection was performed in 15 μ—slide eight-well plates (ibidi 80826). A total of $2–3 \times 10^4$ cells were seeded per well in 200 μL of medium. Twenty-four hours after seeding, the cells were transfected using 150 ng of DNA per expression plasmid, 0.5 μL of jetPRIME, and 15 μL of jetPRIME buffer. Twenty-four hours after transfection, the cells were washed once with PBS supplemented with $MgCl_2$ and $CaCl_2$ (PBS⁺, Dulbecco's phosphate buffered saline, Sigma-Aldrich D8662) and immunofluorescence staining was performed.

In case of the bicistronic vector construct, cells were transfected with 200 ng plasmid DNA. 4 h after transfection, expression was induced by doxycycline (1 μg/mL final concentration) and 24 h after induction, cells were washed once with PBS⁺ and ICC was performed.

Transfection of HEK293T cells for UHPLC-QQQ-MS. The transfection was performed in six-well plates (Sarstedt 83.3920.300). A total of 2.5×10^5 cells were seeded per well in 3 mL of RPMI medium. Twenty-four hours after seeding, the cells were transfected using 1.5 μg of DNA per expression plasmid (combination of GFP-Tet3 and one of the *Glud1* expression plasmids), 4 μL of jetPRIME, and 150 μL of jetPRIME buffer. In case of GFP-Tet3 only expressing cells, 1.5 μg of pESG-iba45 were co-transfected to keep the amount of transfected DNA constant. Six hours after transfection, the medium was changed and 10, 24, and 48 h after transfection, the cells were harvested and washed once with 1 mL of ice-cold PBS. Hundred microliters were used for GFP signal quantification of living cells using FACS (BD LSRFortessa; FSC 130 V, SSC 300 V, GFP 370 V log, 10,000 events per measurement), the rest was lysed and gDNA was isolated and analyzed by UHPLC-QQQ-MS as described previously using the Agilent 6400 Series Triple Quadrupole LC/MS System with the associated MassHunter Workstation Acquisition software and MassHunter Quantitative Analysis software[45]. The hmdC/dN values were subsequently divided by the mean GFP signal to obtain hmdC/(dN*RFU).

When cells were fed with 4 mM DM-αKG, DM-αKG was added with the medium change 6 h after transfection.

Protein extract preparation

Protein extract preparation from transfected HEK293T cells. The harvested HEK293T cells and the resulting lysate were kept on ice during the preparation at all time. Per eight million cells, 1 mL of RIPA buffer (10 mM Tris (pH = 7.5), 150 mM NaCl, 0.5 mM EDTA, 0.1% (w/v) SDS, 1 % (v/v) Triton X-100, 1% (w/v) deoxycholate), supplemented with 2.5 mM $MgCl_2$, 100 U/mL benzonase (Merck Millipore 70746-3) and 1 × protease inhibitor cocktail (PIC, Roche 05056489001) on the day of preparation was used for the lysis. Cells were resuspended in RIPA buffer and lysed for 1 h at 4 °C on a tube rotator. Afterward, the lysate was centrifuged (10,000 × g, 15 min, 4 °C) and the supernatant containing the proteins was transferred into a new tube. To enrich GFP-tagged proteins, the lysate was immediately incubated with GFP Nano-Traps either on agarose beads (Chromotek gta-20, for in vitro activity assay) or on magnetic agarose beads (Chromotek gtma-20).

Protein extract preparations from murine brain. Protein extracts from whole murine brain (Mus musculus, C57-BL6/J wild type, both genders, 110 days old; Charles River, Sulzfeld, Germany), including separation into the organelle, cytosolic, and the nuclear fraction, were prepared according to a previously published protocol[61]. The nuclear extract was then treated with 25 U/mL benzonase for 30 min on ice and subsequently centrifuged (21,000 × g, 15 min, 4 °C). The supernatant containing the nuclear lysate was transferred to a new tube. A Bradford protein assay (Bio-Rad 5000006) was performed according to the manufacturer´s instructions to determine the protein concentration. To check whether the nuclear fraction showed specific enrichment for nuclear proteins in comparison to the combined organelle/cytosolic fraction and was not heavily contaminated with proteins from other compartments, a western blot against histone H3 (nuclear) and cytochrome c (mitochondrial) was performed. The western blot confirmed the specific enrichment of nuclear proteins in the nuclear fraction (Supplementary Fig. 1c).

Protein extracts from mESC and HEK293T. Protein extracts from mESC J1 wt, mESC TET TKO (primed for 96 h according to a previously published protocol[62]), and HEK293T were prepared as previously described[63].

In vitro activity assay. For the in vitro activity assay on GFP Nano-Trap on agarose beads, GFP-Tet1cd or GFP-Tet3cd bound to the trap was used. The proteins were ectopically expressed in HEK293T (per in vitro assay 1 × P150 culture dishes for GFP-Tet1cd, 3 × P150 culture dishes for GFP-Tet3cd) and the resulting protein extracts were incubated for 1 h at 4 °C on a tube rotator with 140 μL of GFP Nano-Traps on agarose beads per extract. Afterwards, the beads were washed twice with coIP wash buffer 1 (10 mM HEPES pH = 7.5, 150 mM NaCl, 0.5 mM EDTA), twice with coIP wash buffer 2 (10 mM HEPES pH = 7.5, 1 M NaCl, 0.5 mM EDTA) and twice with coIP wash buffer 1. The fluorescence of the GFP-tagged proteins bound to the GFP Nano-Trap was checked on a Tecan Plate Reader (Tecan GENios Pro, fluorescence intensity excitation 400 nm, emission 535 nm) and per reaction, the amount of Nano-Trap was adjusted that the fluorescence signal was 25,000 per reaction. Per assay, seven reactions in TET reaction buffer (50 mM HEPES pH = 7.5, 100 mM NaCl, 2 mM Vitamin C, 1.2 mM ATP, 2.5 mM DTT, 0.1 mM $Fe^{(II)}(NH_4)_2(SO_4)_2$ 6 × H_2O) with different concentrations of αKG (0 μM; 10 μM; 50 μM; 100 μM; 250 μM; 500 μM; 1000 μM) and 4 μM of DNA oligonucleotide (5′-TTTTG[mdC]GGTTG-3′) were set up in 50 μL reaction volume/sample. The samples were incubated at 35 °C for 4 h under shaking. For MALDI-TOF measurements, 1 μL of the reaction supernatant was desalted on a 0.025 μm ø VSWP filter membrane against ddH_2O for at least one hour, co-crystallized in a 3-hydroxypicolinic acid matrix (HPA) and mass spectra were recorded on a Bruker Autoflex II in a m/z range of 1500–6000. Spectra were normalized to the recorded maximum intensity. For each condition (GFP-Tet1cd or GFP-Tet3cd, defined αKG concentration) three independent experiments were set up and MALDI-TOF spectra recorded. Afterward, the mean was calculated. The area under the curve was calculated using GraphPad Prism (version 8.0.0 or higher) for mdC in the m/z range 3373.5–3389.0 and 3397.5–3404.5 (Na⁺ peak), hmdC and fdC in the m/z range 3389.0–3397.5 and cadC in the m/z range 3404.5–3410.

To determine the αKG concentration where half-maximal conversion rate is achieved, DNA oligonucleotides were purified after the assay using the Oligo Clean & Concentrator (Zymo Research D4061). Fifty picomoles of the DNA oligonucleotide were digested and analyzed by UHPLC-QQQ-MS according to a previously published protocol[45]. As isotopologues D_3-mdC, D_2-$^{15}N_2$-hmdC, $^{15}N_2$-fdC, $^{15}N_2$-cadC (10 pmol each), and $^{13}C_{10}$-$^{15}N_2$-dT (120 pmol) were spiked in per 50 μL sample. The absolute amounts [pmol] of hmdC, fdC, cadC were calculated and normalized to the absolute amount of dT. As for the conversion to hmdC one molecule of αKG is needed, for the conversion to fdC two molecules and for the conversion to cadC three molecules, the conversion rate was calculated as (n (hmdC)+2*n(fdC)+3*n(cadC))/n(dT).

Tet3-enriched coIP. Twenty microliters of magnetic anti-GFP beads (Chromotek gtma-20) were washed three times with GFP wash buffer (10 mM Tris pH 7.5, 150 mM NaCl, 0.5 mM EDTA) and then incubated for 15 min on ice with nuclear

extract of GFP-Tet3 overexpressing HEK293T cells. To ensure the saturation of the beads with the GFP-fusion construct, different amounts of lysate were tested and monitored using a Tecan Reader. The GFP-Tet3 loaded beads were then washed twice with coIP wash buffer 1, twice with coIP wash buffer 2 and twice with lysis buffer C (20 mM HEPES pH = 7.5, 420 mM NaCl, 2 mM $MgCl_2$, 0.2 mM EDTA, 20% (v/v) glycerol). The GFP-Tet3 beads were subsequently incubated with 200 µg of nuclear brain extract for 15 min on ice. Following, they were washed twice with GFP wash buffer (10 mM Tris pH = 7.5, 150 mM NaCl, 0.5 mM EDTA). To elute the bound proteins, 50 µl of 200 mM glycine pH 2.5 were added and the solution was vortexed for 30 s. To gain more yield, the elution step was repeated. For the negative control, the same procedure was followed using GFP instead of GFP-Tet3.

Tet3-endogenous coIP. CoIP of endogenous Tet3 was performed using nuclear brain extract. Five hundred micrograms of nuclear brain extract, 2 µg of antibody, and 20 µL of Dynabeads Protein G (Thermo Fisher 10003D) were used per replicate. Anti-goat IgG was used for the negative control, which was performed with the same amounts.

The nuclear brain extract was incubated with the antibody for 1 h at 4 °C on a tube rotator and the Dynabeads Protein G were washed three times with GFP wash buffer. Afterward, the Dynabeads were added to the lysate, PBS was added to a final volume of 500 µL and the suspension was incubated for 1 h at 4 °C on a tube rotator. After incubation, the beads were washed three times 10 min with coIP wash buffer 1. Last, proteins were eluted with 50 µL of SDS loading buffer (50 mM Tris pH 6.8, 100 mM DTT, 2% (w/v) SDS, 10% (v/v) glycerol, 0.1% (w/v) bromophenol blue) for 10 min at 70 °C.

LC–MS/MS analysis. Samples for the mass spectrometer were reduced by the addition of 100 mM TCEP and subsequent incubation for 1 h at 60 °C on a shaker at 650 rpm. They were then alkylated by adding 200 mM iodoacetamide and incubating for 30 min at room temperature in the dark. Following, the samples were digested with 0.5 µg trypsin (Promega V5113) at 37 °C for 16 h. Afterward, they were incubated for 5 min at 100 °C, and subsequently 1 mM phenylmethylsulphonyl fluoride was added. StageTips were utilized to purify the samples for MS[64].

The samples were analyzed with an UltiMate 3000 nano liquid chromatography system (Dionex, Fisher Scientific) attached to an LTQ-Orbitrap XL (Thermo Fisher Scientific). They were desalted and concentrated on a µ-precolumn cartridge (PepMap100, C18, 5 µM, 100 Å, size 300 µm i.d. × 5 mm) and further processed on a custom-made analytical column (ReproSil-Pur, C18, 3 µM, 120 Å, packed into a 75 µm i.d. × 150 mm and 8 µm picotip emitter).

The samples were processed via a 127 min multi-step analytical separation at a flow rate of 300 nL/min. The gradient with percentages of solvent B was programmed as follows:

1% for 1 min; 1–4% over 1 min; 4–24% over 100 min; 24–60% over 8 min; 60–85% over 2 min; 85% for 5 min; 85–1% over 2 min; 1% for 8 min.

Mass spectrometric analysis was done with a full mass scan in the mass range between m/z 300 and 1700 at a resolution of 60,000. Following this survey scan, five scans were performed using the ion trap mass analyzer at a normal resolution setting and wideband CID fragmentation with a normalized collision energy of 35. Signals with an unrecognized charge state or a charge state of 1 were not picked for fragmentation. To avoid supersampling of the peptides, an exclusion list was implemented with the following settings: after 2 measurements in 30 s, the peptide was excluded for 90 s.

LFQ data processing. The MaxQuant[65] software (version 1.5.0.25) was used for LFQ. Quantification was performed with four biological replicates for Tet3-enriched coIP. GFP alone (four biological replicates) served here as control. The Andromeda search engine was used in combination with Uniprot databases (Mus musculus). A maximum of two missed cleavage sites was allowed. The main search peptide tolerance was set to 4.5 ppm. Carbamidomethyl (C) was set as static modification. Variable modifications were Acetyl (Protein N-term) and Oxidation (M). The LFQ algorithm was applied with default settings. The option "match between runs" was also used. The MS proteomics data have been deposited to the ProteomeXchange Consortium via the PRIDE[66] partner repository with the dataset identifier PXD004518.

LFQ data were analyzed with the Perseus software (version 1.5.0.9). The LFQ intensities were log transformed and only proteins identified in at least three samples were retained. As one of the GFP control quadruplicates contained only 64 proteins instead of >400, this replicate was removed from the dataset. Gene ontology analyses were performed with the Database for Annotation, Visualization, and Integrated Discovery (DAVID Bioinformatics Resources 6.7).

Western blotting. Samples were loaded on a 4–15% precast polyacrylamide gel (Bio-Rad) and MagicMark XP Standard (Thermo Fisher LC5603) and Blue Pre-stained Protein Standard, Broad Range (11–190 kDa) (New England Biolabs P7706S) or Color-coded Prestained Protein Marker, Broad Range (11–250 kDa) (New England Biolabs 14208) were used as protein standards. The gel was run at constant 150 V for 60 min in SDS running buffer (25 mM Tris, 192 mM glycine, 0.1% (w/v) SDS). For blotting, we used a PVDF blotting membrane (GE Healthcare Amersham Hybond P0.45 PVDF membrane 10600023) and pre-cooled Towbin

blotting buffer (25 mM Tris, 192 mM glycine, 20% (v/v) methanol, 0.038% (w/v) SDS). The membrane was activated for 1 min in methanol, washed with water, and equilibrated for additional 1 min in Towbin blotting buffer; the Whatman gel blotting papers (Sigma-Aldrich WHA 10426981) were equilibrated for 15 min in Towbin buffer and the precast gel was equilibrated for 5 min in Towbin buffer after the run. Western blotting (tank (wet) electro transfer) was performed at 4 °C for 10 h at constant 35 V. After blotting, the PVDF membrane was blocked for 1 h at room temperature using 5% (w/v) milk powder in TBS-T (20 mM Tris pH = 7.5, 150 mM NaCl, 0.1% (v/v) Tween-20). The primary antibodies were diluted in 5 mL of 5% (w/v) milk powder in TBS-T. The blocking suspension was discarded, and the diluted primary antibodies were added for 12 h at 4 °C and shaking. After incubation, the primary antibodies were discarded, and the membrane was washed three times 10 min with TBS-T. HRP-conjugated secondary antibodies were diluted in 5% (w/v) milk powder in TBS-T and added for 1 h at room temperature under shaking. In case of Tet3-endogenous coIP samples, TidyBlot HRP-conjugated Western blot detection reagent (Bio-Rad STAR209P) was used instead of HRP-conjugated secondary antibodies if the primary antibody against the potential interactor was produced in rabbit to avoid detection of the antibody fragments from the coIP. Afterward, the membrane was washed two times with TBS-T and one time with TBS (TBS-T without Tween-20) before SuperSignal West Pico Chemiluminescent Substrate (Thermo Scientific 34077) was used for imaging. Western blots were imaged using Amersham Imager 680 (auto exposure mode).

IHC. All steps were performed in a humidity chamber and at room temperature when not otherwise specified. Twelve micrometers thick coronar cryo-sections of snap-frozen adult mouse brain and liver were incubated (if applicable) with MitoTracker Deep Red FM (Invitrogen M22426) before fixation. Cryo-sections were fixed on slides using 4% paraformaldehyde (4% PFA, Thermo Scientific 28908) in 0.1 M phosphate-buffered solution, pH 7.4 (0.1 M PB). After three times washing with 0.1 M PB, the slices were permeabilized and blocked for 30 min using 0.3% (v/v) Triton X-100 and 5% (v/v) blocking reagent CB (Chemiblocker, Merck Millipore 2170) in 0.1 M PB. The primary antibodies were diluted in 0.1 M PB, containing 5% (v/v) CB and 0.3% (v/v) Triton X-100 and applied for 12 h at 4 °C. For the negative controls, no primary antibodies were added. After incubation, slices were washed three times with 0.1 M PB containing 2% (v/v) CB. For secondary detection, the fluorescent labeled secondary antibodies were diluted in 0.1 M PB, containing 3% (v/v) CB and applied the antibodies for 1 h in the dark, followed by three times washing with 0.1 M PB. Cell nuclei were stained with Hoechst 33342 (5 µg/mL), which was applied for 10 min in the dark, followed by one washing step with 0.1 M PB. After mounting (Mountant Permafluor Thermo Scientific TA-030-FM), the slices were analyzed using a Leica SP8 confocal laser scanning microscope with the associated LAS X software (Leica, Wetzlar).

ICC. ICC experiments were performed as IHC experiments, but instead of 0.1 M PB PBS^+ was used. When ICC of transfected HEK293T cells was analyzed, Image J (version 2.0.0) was used.

PLA. For the PLA experiments, Duolink InSitu Orange Starter Kit (Sigma-Aldrich DUO92102 and DUO92106) was used. Until the application of primary antibodies, the procedure followed the IHC and ICC procedures described above. PLA probes without primary antibodies served as a negative control. After incubation with primary antibodies, slices/cells were washed once with 0.1 M PB/PBS^+. The following steps were carried out as described by the manufacturer with modifications after the last washing step as described in the manual with 0.01 wash buffer B. Before staining of cell nuclei and mounting, slices/cells were washed with 0.1 M PB/PBS^+. Where applicable, Alexa488-NeuN antibody was applied for 2 h in 2% (v/v) CB in 0.1 M PB and slices were washed afterwards three times with 0.1 M PB. However, Alexa488-NeuN application impaired the intensity of the PLA signal. Cell nuclei were stained with Hoechst 33342 (5 µg/mL), which was applied for 10 min in the dark, followed by one washing step with 0.1 M PB/PBS^+. After mounting (Mountant Permafluor Thermo Scientific TA-030-FM), the slices were analyzed using a Leica SP8 confocal laser scanning microscope (Leica, Wetzlar).

Isolation of genomic DNA (gDNA), RNA, and UHPLC-QQQ-MS. Isolation of gDNA, RNA, and UHPLC-QQQ-MS experiments were performed according to a previously published protocol[45].

Synthesis of the Gdh inhibitor R162. Synthesis of the inhibitor R162 was done according to the literature[67,68]. Prior to use for the cell culture, the compound was purified via preparative HPLC (Nucleosil VP 250/10 C18 column Macherey Nagel, 100% MeCN for 10 min).

Depolarization of hippocampal neurons followed by UHPLC-QQQ-MS analysis

Animals. Four- to five-week-old C57-BL6/J (Charles River, Sulzfeld, Germany) wild-type mice of both genders were used.

Hippocampal slices. Acute transverse hippocampal slices (400 μm thick) were prepared as described previously[69,70]. In brief, the brain was removed, the hippocampi of each hemisphere were dissected and cut using a MX-TS tissue slicer (Siskiyou Cooperation, OR). The slices were collected in an oxygenated (95% O_2, 5% CO_2) physiological solution (118 mM NaCl, 3 mM KCl, 1 mM NaH_2PO_4, 25 mM $NaHCO_3$, 10 mM glucose, 1.5 mM $CaCl_2$, 1 mM $MgCl_2$, 0.1% (v/v) DMSO) at 37 °C until the hippocampi of all replicates were cut. Then the slices were distributed to three different conditions: oxygenated physiological solution, oxygenated 25 mM KCl solution (118 mM NaCl, 25 mM KCl, 1 mM NaH_2PO_4, 25 mM $NaHCO_3$, 10 mM Glucose, 1.5 mM $CaCl_2$, 1 mM $MgCl_2$, 0.1% (v/v) DMSO) and oxygenated 25 mM KCl solution supplemented with 20 μM inhibitor R162 or 40 μM UK5099 (Sigma-Aldrich PZ0160-5MG). Six to ten slices were pooled for each replicate. After 6 h incubation time, the slices were transferred into reaction tubes, snap frozen in liquid nitrogen and stored at −80 °C until use. Isolation of gDNA, subsequent digest of gDNA, and analysis by UHPLC-QQQ-MS were performed according to a previously published protocol[45].

We excluded mice from further analysis (hmdC quantification and gene expression) when *Npas4* expression was not upregulated in the depolarized hippocampal slices compared to the unstimulated control (one mouse out of eight for R162 experiment and two mice out of eight for UK5099 experiment) as this is an indicator that stimulation did not work, and the slices might be damaged.

RT-qPCR. For cDNA synthesis, the RevertAid First Strand cDNA Synthesis Kit (Thermo Scientific K1621) was used according to the manufacturer's instructions. One hundred ninety nanograms of total RNA was used for cDNA synthesis. Real-time quantitative PCR (RT-qPCR) was performed on StepOnePlus Real-Time PCR system (Applied Biosystems Thermo Fisher Scientific) using PowerUp[TM] SYBR[TM] Green qPCR Master Mix (Applied Biosystems Thermo Fisher Scientific A25742). C_T values of each sample were determined in technical duplicates by the StepOne[TM] Software (Applied Biosystems Thermo Fisher Scientific) using the fast cycle protocol. The relative expression levels of target genes were then quantified from seven biological replicates ($n = 7$) according to Pfaffl et al.[71,72].

The primers for RT-qPCR are listed in Supplementary Table 1 and the following primers have been published previously:
Npas4 (mouse)[73]
Bdnf total (mouse)[74]

Metabolomics. Pre-weighed frozen hippocampal tissues from six mice ($n = 6$) per condition (physiological solution, 25 mM KCl, 25 mM KCl + R162) were homogenized using a bullet blender and five 1.4 mm stainless steel beads in a mixture of 1.05 ml ice-cold methanol/chloroform 1:2 (v/v). Following sonication of supernatants for 1 min, an additional 0.7 ml mixture of chloroform/LC grade water, 1:1 (v/v) were added, samples were vortexed for 20 s and incubated on wet ice for 30 min. Extracts were then centrifuged for 5 min at $16,000 \times g$ and 4 °C and 0.6 ml from the upper aqueous phase were collected and dried under nitrogen gas. For NMR measurements, the dried extracts were dissolved in 0.25 ml 0.15 M phosphate buffer (pH 7.4) in deuterated water containing 0.04 mM sodium trimethylsilyl-propionate-d_4 (TSP) as internal standard. One 1D proton NMR was collected for each sample in a 14.1 T Bruker Avance II NMR under standardized conditions as described in Kostidis et al., 2017[40]. The NMR buffer was degassed, and NMR tubes were flushed with nitrogen to prevent oxidation. Metabolites were quantified in Chenomx NMR suit 8.4 (Chenomx Inc, Canada) and concentrations were corrected according to the tissue mass per sample. One mouse was completely excluded from further analysis as one sample out of the three conditions was lost during the sample preparation.

Statistics and Reproducibility
Details about the statistical analysis. Statistical analysis, except for LFQ data processing as described above, was performed using GraphPad Prism (version 8.0.0 or higher) and only measurements from biological independent samples were considered.
Figure 3d:
For each biologically independent sample, hmdC/dN, fdC/dN, and cadC/dN values were normalized to the GFP signal to balance different Tet3 expression levels between the GFP-Tet3 and the GFP-Tet3 + Gdh-FLAG expressing cells, resulting in hmdC/(dN*RFU), fdC/(dN*RFU) and cadC/(dN*RFU). Samples were grouped (columns: Group A GFP-Tet3, Group B GFP-Tet3 + Gdh-FLAG; rows: 10, 24, 48 h post transfection; $n = 3$ biologically independent samples for each condition). For analysis, multiple t-tests (one per row, all of them two-sided) were chosen with individual variances between the rows. Statistical significance was determined using Holm-Sidak method with alpha = 0.05 to correct for multiple comparisons.
hmdC/(dN*RFU): 10 h: *p* value 0.000026, p_{adj} value 0.000078
24 h: *p* value 0.002581, p_{adj} value 0.005156
48 h: *p* value 0.003545, p_{adj} value 0.005156
fdC/(dN*RFU):10 h: *p* value 0.022270, p_{adj} value 0.038038
24 h: *p* value 0.009375, p_{adj} value 0.027862
48 h: *p* value 0.019204, p_{adj} value 0.038038
cadC/(dN*RFU):10 h: - 24 h: *p* value 0.009375, p_{adj} value 0.030692

48 h: *p* value 0.019204, p_{adj} value 0.040533
Figure 4a:
Differences between hmdC and fdC levels of GFP-Tet3 + Gdh-FLAG and GFP-Tet3 + Gdh-FLAG-NES expressing cells were analyzed individually for each biological replicate by calculating the paired t-test (two-sided *p* value).
hmdC: paired *t* test *p* value 0.0468; correlation coefficient *r* of the pairing 0.9492 (*p* value 0.0068, significantly effective pairing).
fdC: paired *t* test *p* value 0.0081; correlation coefficient r of the pairing 0.9708 (*p* value 0.0030, significantly effective pairing).
Figure 4d–f:
For each mouse, the prepared hippocampal slices were distributed to three different conditions – (A) physiological buffer, (B) 25 mM KCl, (C) 25 mM KCl + Inhibitor (20 μM R162 or 40 μM UK5099).
Figure 4d:
hmdC level R162 experiment:
$n = 7$, RM one-way ANOVA with Geisser–Greenhouse correction *p* value 0.0052; matching *p* value (one-sided) <0.0001. Tukey's multiple comparisons test with individual variances computed for each comparison: A/B *p* value 0.0136, A/C *p* value 0.9995, B/C *p* value 0.0037.
hmdC level UK5099 experiment:
$n = 6$, RM one-way ANOVA with Geisser–Greenhouse correction *p* value 0.0034; matching *p* value (one-sided) <0.0001. Tukey's multiple comparisons test with individual variances computed for each comparison: A/B *p* value 0.0410, A/C p-value 0.0123, B/C p-value 0.0130.
Figure 4e:
αKG level (normalized to mg of tissue) R162 experiment $n = 5$, ordinary one-way ANOVA *p* value 0.0002 (Brown-Forsythe test *p* value 0.1512). Tukey's multiple comparisons test A/B *p* value 0.0001, A/C *p* value 0.0279, B/C *p* value 0.0230.
αKG/succinate ratio R162 experiment: $n = 5$, ordinary one-way ANOVA p-value 0.0368 (Brown–Forsythe test p-value 0.7828). Tukey's multiple comparisons test A/B *p* value 0.1215, A/C *p* value 0.7684, B/C *p* value 0.0364.
Figure 4f:
Npas4 gene expression level R162 experiment normalized to the gene expression level of the unstimulated control: $n = 7$, unpaired t-test with Welch's correction (*F* test *p* value 0.3443) *p* value (two-sided) 0.0131.
Bdnf gene expression level R162 experiment normalized to the gene expression level of the unstimulated control: $n = 7$, unpaired *t*-test with Welch's correction (*F* test *p* value 0.0208) *p* value (two-sided) 0.0136.
Supplementary Fig. 5d:
For each sample ($n = 3$ biologically independent samples), hmdC/dN and fdC/dN values were normalized to the GFP signal to balance different Tet3 expression levels between the samples (GFP-Tet3 A, GFP-Tet3 + 4 mM DM-αKG B, GFP-Tet3 + Gdh-FLAG C, GFP-Tet3 + Gdh-FLAG-NES), resulting in hmdC/(dN*RFU) and fdC/(dN*RFU).
For hmdC, ordinary one-way ANOVA *p* value 0.0209 (Brown–Forsythe test *p* value 0.6166). Tukey's multiple comparisons test A/B *p* value 0.6289, A/C *p* value 0.0103, A/D *p* value 0.1509.
For fdC, ordinary one-way ANOVA *p* value 0.0070 (Brown–Forsythe test *p* value 0.6725). Tukey's multiple comparisons test A/B *p* value 0.9942, A/C *p* value 0.0052, A/D *p* value 0.3030.

Details about the reproducibility. Figure 1b:
The preparation of the nuclear lysate from mESCs (4d primed) and total murine brain (4–5 weeks old wt BL6/J) was performed from two biologically independent samples/animals. These preparations were subsequently analyzed by western blotting against Tet1, Tet2, Tet3, and histone H3. Figure 1b shows representative western blots of this experiment.
Figure 2d:
coIP of endogenous Tet3 and a corresponding control coIP (using a non-targeting anti-goat antibody) was performed twice using two biologically independent nuclear lysate preparations from total murine brain (three months old wt BL6/J) and analyzed by western blotting. Figure 2d shows one representative blot of this experiment.
Figure 2e:
Tet3-Gdh PLA was performed in total four times using coronal cryo-sections of snap-frozen adult mouse brain from two biologically independent animals. Figure 2e shows one representative PLA result.
Figure 3a:
IHC/IF in hippocampus (Tet3 and Gdh) was performed in total four times using coronal cryo-sections of snap-frozen adult mouse brain from two biologically independent animals. IHC/IF in liver (Tet3 and Gdh) was performed two times using coronal cryo-sections of snap-frozen adult mouse liver from one animal. Figure 3a shows one representative IHC result.
Figure 3b:
Cell fractionation preparation from total murine brain (4–5 weeks old wt BL6/J) was performed from four biologically independent animals. These preparations were subsequently analyzed by western blotting. Figure 3b shows one representative western blot of this experiment.
Figure 3d:

GFP-Tet3 + Gdh-FLAG PLA or GFP + Gdh-FLAG PLA were performed twice in two biologically independent samples. Figure 3d shows one representative PLA result.

Figure 4b:

ICC/IF in GFP-Tet3 + Gdh-FLAG or GFP + Gdh-FLAG expressing HEK293T cells was performed three times using three biologically independent samples. Figure 4b shows one representative ICC result.

Figure 4c:

ICC/IF in FLAG₃-Tet3-T2A-Glud1 transfected or untransfected HEK293T cells was performed three times using three biologically independent samples. Figure 4c shows one representative ICC result.

Figure 4g:

Tet3-NPC PLA and Gdh-NPC PLA were performed twice using coronar cryo-sections of snap-frozen adult mouse brain from one animal. Figure 4g shows one representative PLA result.

Reporting summary. Further information on research design is available in the Nature Research Reporting Summary linked to this article.

Data availability

References

1. Kriaucionis, S. & Heintz, N. The nuclear DNA base 5-hydroxymethylcytosine is present in Purkinje neurons and the brain. *Science* **324**, 929–930 (2009).
2. Tahiliani, M. et al. Conversion of 5-methylcytosine to 5-hydroxymethylcytosine in mammalian DNA by MLL partner TET1. *Science* **324**, 930–935 (2009).
3. Ito, S. et al. Role of Tet proteins in 5mC to 5hmC conversion, ES-cell self-renewal and inner cell mass specification. *Nature* **466**, 1129–1133 (2010).
4. Chen, K., Zhao, Boxuan, S. & He, C. Nucleic acid modifications in regulation of gene expression. *Cell Chem. Biol.* **23**, 74–85 (2016).
5. Lu, X., Zhao, B. S. & He, C. TET family proteins: oxidation activity, interacting molecules, and functions in diseases. *Chem. Rev.* **115**, 2225–2239 (2015).
6. Ehrlich, M. & Ehrlich, K. C. DNA cytosine methylation and hydroxymethylation at the borders. *Epigenomics* **6**, 563–566 (2014).
7. Traube, F. R. & Carell, T. The chemistries and consequences of DNA and RNA methylation and demethylation. *RNA Biol.* **14**, 1099–1107 (2017).
8. Carell, T., Kurz, M. Q., Müller, M., Rossa, M. & Spada, F. Non-canonical bases in the genome: the regulatory information layer in DNA. *Angew. Chem. Int. Ed. Engl.* **57**, 4296–4312 (2018).
9. Globisch, D. et al. Tissue distribution of 5-hydroxymethylcytosine and search for active demethylation intermediates. *PLoS ONE* **5**, e15367 (2010).
10. Wagner, M. et al. Age-dependent levels of 5-methyl-, 5-hydroxymethyl-, and 5-formylcytosine in human and mouse brain tissues. *Angew. Chem. Int. Ed. Engl.* **54**, 12511–12514 (2015).
11. Khare, T. et al. 5-hmC in the brain is abundant in synaptic genes and shows differences at the exon-intron boundary. *Nat. Struct. Mol. Biol.* **19**, 1037–1043 (2012).
12. Szwagierczak, A., Bultmann, S., Schmidt, C. S., Spada, F. & Leonhardt, H. Sensitive enzymatic quantification of 5-hydroxymethylcytosine in genomic DNA. *Nucleic Acids Res.* **38**, e181 (2010).
13. Guo, J. U. et al. Neuronal activity modifies DNA methylation landscape in the adult brain. *Nat. Neurosci.* **14**, 1345–1351 (2011).
14. Yu, H. et al. Tet3 regulates synaptic transmission and homeostatic plasticity via DNA oxidation and repair. *Nat. Neurosci.* **18**, 836–843 (2015).
15. Zdzisińska, B., Żurek, A. & Kandefer-Szerszeń, M. Alpha-ketoglutarate as a molecule with pleiotropic activity: well-known and novel possibilities of therapeutic use. *Arch. Immunol. Ther. Exp.* **65**, 21–36 (2017).
16. Yang, Q. et al. AMPK/α-ketoglutarate axis dynamically mediates DNA demethylation in the Prdm16 promoter and brown adipogenesis. *Cell Metab.* **24**, 542–554 (2016).
17. Park, J. O. et al. Metabolite concentrations, fluxes and free energies imply efficient enzyme usage. *Nat. Chem. Biol.* **12**, 482–489 (2016).
18. TeSlaa, T. et al. alpha-ketoglutarate accelerates the initial differentiation of primed human pluripotent stem cells. *Cell Metab.* **24**, 485–493 (2016).
19. Carey, B. W., Finley, L. W., Cross, J. R., Allis, C. D. & Thompson, C. B. Intracellular alpha-ketoglutarate maintains the pluripotency of embryonic stem cells. *Nature* **518**, 413–416 (2015).
20. Mews, P. et al. Acetyl-CoA synthetase regulates histone acetylation and hippocampal memory. *Nature* **546**, 381–386 (2017).
21. Sutendra, G. et al. A nuclear pyruvate dehydrogenase complex is important for the generation of acetyl-CoA and histone acetylation. *Cell* **158**, 84–97 (2014).
22. Boukouris, A. E., Zervopoulos, S. D. & Michelakis, E. D. Metabolic enzymes moonlighting in the nucleus: metabolic regulation of gene transcription. *Trends Biochem. Sci.* **41**, 712–730 (2016).
23. Featherstone, D. E. Intercellular glutamate signaling in the nervous system and beyond. *ACS Chem. Neurosci.* **1**, 4–12 (2010).
24. Fasolino, M., Welsh, S. A. & Zhou, Z. TET and 5hmC in neurodevelopment and the adult brain, in *DNA modifications in the brain*. (ed. Bredy, T. W.) 61–79 (Academic Press is an imprint of Elsevier, London, United Kingdom, 2017).
25. Kaas, G. A. et al. TET1 controls CNS 5-methylcytosine hydroxylation, active DNA demethylation, gene transcription, and memory formation. *Neuron* **79**, 1086–1093 (2013).
26. Tan, L. & Shi, Y. G. Tet family proteins and 5-hydroxymethylcytosine in development and disease. *Development* **139**, 1895–1902 (2012).
27. Dawlaty, M. M. et al. Combined deficiency of Tet1 and Tet2 causes epigenetic abnormalities but is compatible with postnatal development. *Dev. Cell* **24**, 310–323 (2013).
28. Beck, D. B. et al. Delineation of a human mendelian disorder of the DNA demethylation machinery: TET3 deficiency. *Am. J. Hum. Genet.* **106**, 234–245 (2020).
29. Laukka, T. et al. Fumarate and succinate regulate expression of hypoxia-inducible genes via TET enzymes. *J. Biol. Chem.* **291**, 4256–4265 (2016).
30. Liu, N. et al. Intrinsic and extrinsic connections of Tet3 dioxygenase with CXXC zinc finger modules. *PLoS ONE* **8**, e62755 (2013).
31. Cox, J. et al. Accurate proteome-wide label-free quantification by delayed normalization and maximal peptide ratio extraction, termed MaxLFQ. *Mol. Cell. Proteom.* **13**, 2513–2526 (2014).
32. Bauer, C. et al. Phosphorylation of TET proteins is regulated via O-GlcNAcylation by the O-linked N-acetylglucosamine transferase (OGT). *J. Biol. Chem.* **290**, 4801–4812 (2015).
33. Deplus, R. et al. TET2 and TET3 regulate GlcNAcylation and H3K4 methylation through OGT and SET1/COMPASS. *EMBO J.* **32**, 645–655 (2013).
34. Ito, R. et al. TET3-OGT interaction increases the stability and the presence of OGT in chromatin. *Genes Cells* **19**, 52–65 (2014).
35. Plaitakis, A., Kalef-Ezra, E., Kotzamani, D., Zaganas, I. & Spanaki, C. The glutamate dehydrogenase pathway and its roles in cell and tissue biology in health and disease. *Biology* **6**, 11 (2017).
36. Hohnholt, M. C. et al. Glutamate dehydrogenase is essential to sustain neuronal oxidative energy metabolism during stimulation. *J. Cereb. Blood Flow. Metab.* **38**, 1754–1768 (2017).
37. Mastorodemos, V. et al. Human GLUD1 and GLUD2 glutamate dehydrogenase localize to mitochondria and endoplasmic reticulum. *Biochem. Cell Biol.* **87**, 505–516 (2009).
38. Spinelli, J. B. et al. Metabolic recycling of ammonia via glutamate dehydrogenase supports breast cancer biomass. *Science* **358**, 941 (2017).
39. Braissant, O., McLin, V. A. & Cudalbu, C. Ammonia toxicity to the brain. *J. Inherit. Metab. Dis.* **36**, 595–612 (2013).
40. Kostidis, S., Addie, R. D., Morreau, H., Mayboroda, O. A. & Giera, M. Quantitative NMR analysis of intra- and extracellular metabolism of mammalian cells: a tutorial. *Anal. Chim. Acta* **980**, 1–24 (2017).
41. Cooper, A. J. L. 13N as a tracer for studying glutamate metabolism. *Neurochem. Int.* **59**, 456–464 (2011).
42. Söderberg, O. et al. Characterizing proteins and their interactions in cells and tissues using the in situ proximity ligation assay. *Methods* **45**, 227–232 (2008).
43. Perera, A. et al. TET3 is recruited by REST for context-specific hydroxymethylation and induction of gene expression. *Cell Rep.* **11**, 283–294 (2015).
44. Karaca, M. et al. Liver glutamate dehydrogenase controls whole-body energy partitioning through amino acid-derived gluconeogenesis and ammonia homeostasis. *Diabetes* **67**, 1949–1961 (2018).
45. Traube, F. R. et al. Isotope-dilution mass spectrometry for exact quantification of noncanonical DNA nucleosides. *Nat. Protoc.* **14**, 283–312 (2019).
46. Jin, L. et al. Glutamate dehydrogenase 1 signals through antioxidant glutathione peroxidase 1 to regulate redox homeostasis and tumor growth. *Cancer Cell* **27**, 257–270 (2015).
47. Hurh, S. et al. Expression analysis of combinatorial genes using a Bi-cistronic T2A expression system in porcine fibroblasts. *PLoS ONE* **8**, e70486 (2013).
48. Liu, Z. et al. Systematic comparison of 2A peptides for cloning multi-genes in a polycistronic vector. *Sci. Rep.* **7**, 2193 (2017).
49. Bading, H., Ginty, D. D. & Greenberg, M. E. Regulation of gene expression in hippocampal neurons by distinct calcium signaling pathways. *Science* **260**, 181 (1993).

50. Yang, C. et al. Glutamine oxidation maintains the TCA cycle and cell survival during impaired mitochondrial pyruvate transport. *Mol. Cell* **56**, 414–424 (2014).

51. Kowiański, P. et al. BDNF: a key factor with multipotent impact on brain signaling and synaptic plasticity. *Cell. Mol. Neurobiol.* **38**, 579–593 (2018).

52. Sun, X. & Lin, Y. Npas4: linking neuronal activity to memory. *Trends Neurosci.* **39**, 264–275 (2016).

53. Sexton, T., Schober, H., Fraser, P. & Gasser, S. M. Gene regulation through nuclear organization. *Nat. Struct. Mol. Biol.* **14**, 1049 (2007).

54. Chen, C., Ding, X., Akram, N., Xue, S. & Luo, S.-Z. Fused in sarcoma: properties, self-assembly and correlation with neurodegenerative diseases. *Molecules* **24**, 1622 (2019).

55. Lai, J. C., Sheu, K. F., Kim, Y. T., Clarke, D. D. & Blass, J. P. The subcellular localization of glutamate dehydrogenase (GDH): is GDH a marker for mitochondria in brain? *Neurochem. Res.* **11**, 733–744 (1986).

56. Nagaraj, R. et al. Nuclear localization of mitochondrial TCA cycle enzymes as a critical step in mammalian zygotic genome activation. *Cell* **168**, 210–223 e211 (2017).

57. Nikiforov, A., Kulikova, V. & Ziegler, M. The human NAD metabolome: functions, metabolism and compartmentalization. *Crit. Rev. Biochem. Mol. Biol.* **50**, 284–297 (2015).

58. Ryu, K. W. et al. Metabolic regulation of transcription through compartmentalized NAD+ biosynthesis. *Science* **360**, eaan5780 (2018).

59. Müller, U., Bauer, C., Siegl, M., Rottach, A. & Leonhardt, H. TET-mediated oxidation of methylcytosine causes TDG or NEIL glycosylase dependent gene reactivation. *Nucleic Acids Res.* **42**, 8592–8604 (2014).

60. Xu, D., Farmer, A., Collett, G., Grishin, N. V. & Chook, Y. M. Sequence and structural analyses of nuclear export signals in the NESdb database. *Mol. Biol. Cell* **23**, 3677–3693 (2012).

61. Guillemin, I., Becker, M., Ociepka, K., Friauf, E. & Nothwang, H. G. A subcellular prefractionation protocol for minute amounts of mammalian cell cultures and tissue. *Proteomics* **5**, 35–45 (2005).

62. Iwan, K. et al. 5-Formylcytosine to cytosine conversion by C–C bond cleavage in vivo. *Nat. Chem. Biol.* **14**, 72–78 (2017).

63. Dignam, J. D., Lebovitz, R. M. & Roeder, R. G. Accurate transcription initiation by RNA polymerase II in a soluble extract from isolated mammalian nuclei. *Nucleic Acids Res.* **11**, 1475–1489 (1983).

64. Kulak, N. A., Pichler, G., Paron, I., Nagaraj, N. & Mann, M. Minimal, encapsulated proteomic-sample processing applied to copy-number estimation in eukaryotic cells. *Nat. Methods* **11**, 319–324 (2014).

65. Cox, J. & Mann, M. MaxQuant enables high peptide identification rates, individualized p.p.b.-range mass accuracies and proteome-wide protein quantification. *Nat. Biotechnol.* **26**, 1367–1372 (2008).

66. Vizcaíno, J. A. et al. 2016 update of the PRIDE database and its related tools. *Nucleic Acids Res.* **44**, D447–D456 (2016).

67. Murty, K. V. S. N., Pal, R., Datta, K. & Mal, D. Glucose promoted claisen rearrangement of 1-Allyloxy anthraquinones. *Synth. Commun.* **24**, 1287–1292 (1994).

68. Sharghi, H. & Aghapour, G. Claisen rearrangement of allyloxyanthraquinones with silver/potassium iodide in acetic acid as a new and efficient reagent. *J. Org. Chem.* **65**, 2813–2815 (2000).

69. Kleppisch, T. et al. Long-term potentiation in the hippocampal CA1 region of mice lacking cGMP-dependent kinases is normal and susceptible to inhibition of nitric oxide synthase. *J. Neurosci.* **19**, 48–55 (1999).

70. Michalakis, S. et al. Altered synaptic plasticity and behavioral abnormalities in CNGA3-deficient mice. *Genes Brain Behav.* **10**, 137–148 (2011).

71. Pfaffl, M. W. A new mathematical model for relative quantification in real-time RT-PCR. *Nucleic Acids Res.* **29**, e45 (2001).

72. Pfaffl, M. W., Horgan, G. W. & Dempfle, L. Relative expression software tool (REST) for group-wise comparison and statistical analysis of relative expression results in real-time PCR. *Nucleic Acids Res.* **30**, e36 (2002).

73. Ramamoorthi, K. et al. Npas4 regulates a transcriptional program in CA3 required for contextual memory formation. *Science* **334**, 1669–1675 (2011).

74. Ma, D. K. et al. Neuronal activity-induced Gadd45b promotes epigenetic DNA demethylation and adult neurogenesis. *Science* **323**, 1074–1077 (2009).

75. Haug, K. et al. MetaboLights: a resource evolving in response to the needs of its scientific community. *Nucleic Acids Res.* **48**, D440–D444 (2019).

Author contributions

F.R.T. designed experiments, performed and analyzed Tet3-endogenous coIP, performed and analyzed western blots, IHC/ICC experiments, PLAs, UHPLC-QQQ-MS experiments, in vitro activity assays, RT-qPCR, helped with depolarization experiments of hippocampal slices and interpreted data. D.Ö. performed and analyzed IHC/ICC experiments and PLAs, helped with western blots and in vitro activity assays, and designed the Gdh-FLAG-NES construct. H.S. designed the bicistronic vector for FLAG$_3$-Tet3/Gdh expression, performed and analyzed ICC experiments and western blots. C.S. performed depolarization experiments of acute hippocampal slices, dissected mouse brain and liver and prepared cryo-sections thereof, analyzed IHC/ICC experiments and performed and analyzed RT-qPCR experiments. A.F.G. designed proteomics experiments, developed the GFP-Tet3-enriched coIP workflow, performed and analyzed GFP-Tet3-enriched coIP and interpreted proteomics data. A.S.G. helped performing and analyzing IHC/ICC experiments and PLAs. S.O. helped with in vitro activity assays. S.K. performed and analyzed metabolomics experiments. K.I. helped performing and analyzing UHPLC-QQQ-MS experiments. R.R. synthesized R162. G.G. helped analyzing ICC experiments. M.M. and F.S. designed experiments and interpreted data. M.B. interpreted data. J.C. helped with analysis of proteomics data. M.G. supervised metabolomics experiments. S.M. designed and supervised experiments, performed depolarization experiments of acute hippocampal slices and interpreted data. T.C. designed and supervised the whole study and interpreted data. F.R.T. and T.C wrote the manuscript with help from M.M. and S.M.

Funding

Open Access funding enabled and organized by Projekt DEAL.

Competing interests

The authors declare no competing interests.

Additional information

Supplementary information The online version contains supplementary material available at https://doi.org/10.1038/s41467-021-24353-9.

Correspondence and requests for materials should be addressed to S.M. or T.C.

Peer review information *Nature communications* thanks the anonymous reviewers for their contributions to the peer review of this work.

Reprints and permission information is available at http://www.nature.com/reprints

Publisher's note Springer Nature remains neutral with regard to jurisdictional claims in published maps and institutional affiliations.

5.3 "Novel Poxin Stable cGAMP-Derivatives Are Remarkable STING Agonists"

Samuele Stazzoni*, Daniel F. R. Böhmer*, Fabian Hernichel*, Dilara Özdemir, Aikaterini Pappa, David Drexler, Stefan Bauernfried, Gregor Witte, Mirko Wagner, Simon Veth, Karl-Peter Hopfner, Veit Hornung*, Lars M. König*, and Thomas Carell*

*: These authors contributed equally to this work.

Introduction and Summary

The innate immune pathway cGAS-STING is activated upon detection of cytosolic DNA. One way of DNA to be found in the cytosol is viral infection. DNA viruses replicating their genetic material in the cytosol have developed mechanisms to overcome the defence mechanisms of the cell. When cGAS detects cytosolic DNA, it produces 2',3'-cyclic-Guanosine-Adenosine-Monophosphate (cGAMP). Poxviruses have poxin enzymes which are able to degrade cGAMP. Chemists of the Carell group have synthesized poxin-stable cGAMP analogues by removal of the -OH groups. The synthesis was done by using a synthetic combination of phosphoramidite and phosphotriester chemistry. The analogues dideoxy-2',3'-cGAMP, dideoxy-2',3'-cAAMP and dideoxy-2',3'-cAGMP were evaluated for their Effective Concentration 50 (EC_{50}) values, melting temperatures (ΔT_M) and binding constants (K_D). Stability of the analogues dideoxy-2',3'-cGAMP and dideoxy-2',3'-cAAMP were observed by enzymatic assay followed by quantitation with liquid chromatography-mass spectrometry. These analogues were then subjected in a hepatocellular tumor model *in vivo*. Both analogues were found to reduce tumour growth in comparison to natural 2',3'-cGAMP, whereas dideoxy-2',3'-cAAMP showed the most remarkable growth reduction of the tumor.

Declaration of Contribution

In this work, I performed EC_{50} assays for all compounds. I designed and optimised the enzymatic assay to assess stability of the compounds against poxins. I processed the samples of the enzymatic assays after the analogues were exposed to the poxin enzymes, extracted the samples and purified them for sensitive LC-MS analysis. Detailed information of these processes can be found in this thesis under section 3.1.

Authorization

VIP **Medicinal Chemistry** *Very Important Paper*

Novel Poxin Stable cGAMP-Derivatives Are Remarkable STING Agonists

Samuele Stazzoni[+], Daniel F. R. Böhmer[+], Fabian Hernichel[+], Dilara Özdemir,
Aikaterini Pappa, David Drexler, Stefan Bauernfried, Gregor Witte, Mirko Wagner,
Simon Veth, Karl-Peter Hopfner, Veit Hornung,* Lars M. König,* and Thomas Carell*

Abstract: 2′,3′-cGAMP is a cyclic A- and G-containing dinucleotide second messenger, which is formed upon cellular recognition of foreign cytosolic DNA as part of the innate immune response. The molecule binds to the adaptor protein STING, which induces an immune response characterized by the production of type I interferons and cytokines. The development of STING-binding molecules with both agonistic as well as antagonistic properties is currently of tremendous interest to induce or enhance antitumor or antiviral immunity on the one hand, or to treat autoimmune diseases on the other hand. To escape the host innate immune recognition, some viruses encode poxin endonucleases that cleave 2′,3′-cGAMP. Here we report that dideoxy-2′,3′-cGAMP (**1**) and analogs thereof, which lack the secondary ribose-OH groups, form a group of poxin-stable STING agonists. Despite their reduced affinity to STING, particularly the compound constructed from two A nucleosides, dideoxy-2′,3′-cAAMP (**2**), features an unusually high antitumor response in mice.

*T*he innate immune system is the first line of defense against pathogens. It is triggered by dedicated sensor proteins that recognize specific pathogen features as non-self.[1,2] Bacterial and viral infections, but also ruptured nuclear and mitochondrial membranes of damaged cells, generate double-stranded DNA (dsDNA) in the cytosol of the corresponding cell.[3] This creates a pathogenic state that is sensed by the enzyme cyclic-GMP-AMP-synthase (cGAS), which cyclizes GTP and ATP to generate the second messenger 2′,3′-cyclic-GMP-AMP (2′,3′-cGAMP) (Figure 1a).[4–7] Binding of 2′,3′-cGAMP to the endoplasmic reticulum transmembrane protein stimulator of interferon genes (STING) leads to its oligomerization, which finally stimulates the expression of type I interferons (IFNs) and pro-inflammatory cytokines with potent anti-viral and anti-bacterial effects.[8] To circumvent the cGAS/STING host defense system, vaccinia viruses encode poxvirus immune nucleases (poxins), which were shown to specifically hydrolyze the 3′-5′-linkage of the mediator molecule 2′,3′-cGAMP, leading to its degradation (Figure 1a).[9] This is achieved by the metal ion-free catalysis of an auto-degradation process, in which the poxin activates the free 2′-OH of 2′,3′-cGAMP with an active site lysine residue (K142) to promote an intramolecular attack on the 3′-5′ phosphodiester linkage, to generate an adenosine-2′,3′-cyclophosphate intermediate. According to this mechanism, removing the 2′-OH group of 2′,3′-cGAMP would potentially provide a powerful agonist that would be resistant to this viral escape pathway. However, removing the ribose OH group has consequences regarding binding to STING. It is proposed that the 3′-OH group establishes a key interaction with Ser162 of the human STING (hSTING) active site.[10] This is supposed to allow hSTING to differentiate 2′,3′-cGAMP from 3′,3′-cGAMP, which is a key bacterial second messenger (Figure 1a).

In the context of antiviral therapies, the cGAS/STING-pathway is a key component of innate immunity against DNA viruses and retroviruses such as HIV.[11–15] Activation of STING can consequently increase antiviral responses. In

---

[*] Dr. S. Stazzoni[+]
New address: Monoclonal Antibody Discovery (MAD) Lab, Fonda-zione Toscana Life Sciences
53100 Siena (Italy)

Dr. S. Stazzoni,[+] MSc. F. Hernichel,[+] MSc. D. Özdemir,
MSc. A. Pappa, Dr. M. Wagner, Dr. S. Veth, Prof. Dr. T. Carell
Department of Chemistry, Ludwig-Maximilians-Universität München
Butenandtstr. 5–13, 81377 Munich (Germany)
E-mail: Thomas.carell@lmu.de

Dr. D. F. R. Böhmer,[+] Dr. L. M. König
Division of Clinical Pharmacology, University Hospital, Ludwig-Maximilians-Universität München
Lindwurmstr. 2a, 80337 Munich (Germany)
E-mail: lars.koenig@med.uni-muenchen.de

Dr. D. Drexler, Dr. S. Bauernfried, Dr. G. Witte,
Prof. Dr. K.-P. Hopfner, Prof. Dr. V. Hornung
Gene Center and Department of Biochemistry, Ludwig-Maximilians-Universität München
Feodor-Lynen-Str. 25, 81377 Munich (Germany)
E-mail: hornung@genzentrum.lmu.de

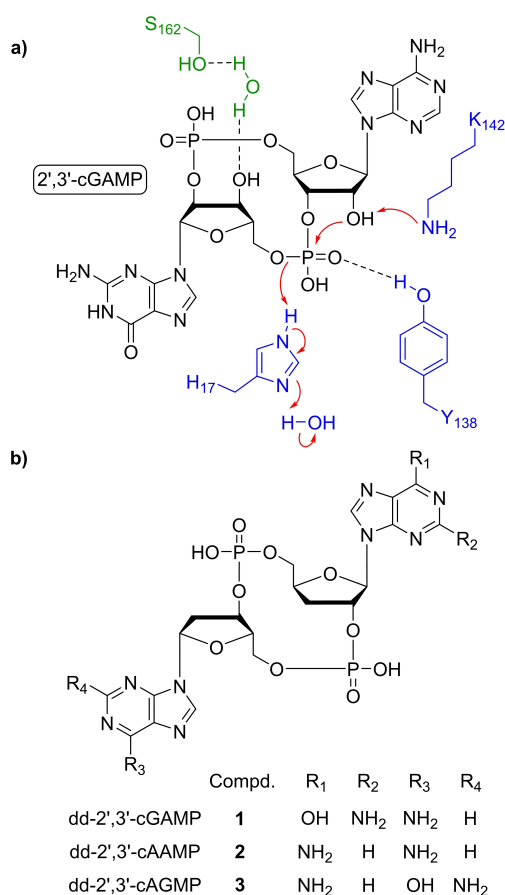[+] These authors contributed equally to this work.

Figure 1. a) Depiction of important 2′,3′-cGAMP interactions. Green: Interaction of 3′-OH with S162 of hSTING according to Zhang et al.[10] Blue: Mechanism of cleavage performed by vaccinia virus poxins, adapted from Eaglesham et al.[9] b) Structures of the synthesized dideoxy-2′,3′-cGAMP derivatives.

addition, STING activation can stimulate antitumor immune responses, which makes STING also a prime target for cancer immunotherapy.[16–19] The first STING agonists have recently entered clinical trials.[20–22] Here we present a new and concise synthesis of dideoxy-2′,3′-cyclic-dinucleotides (dd-2′,3′-CDNs) such as **1**, **2** and **3** (Figure 1b) and data about poxin-mediated degradation. Furthermore, we benchmark the synthesized compounds to natural 2′,3′-cGAMP in a preclinical mouse model of hepatocellular carcinoma.

The synthesis of dd-2′,3′-CDNs **1–3** started from protected xylofuranose **4** (Scheme 1). Dimethoxytrityl (DMTr) protected 3′-deoxyribonucleotides **5** and **6** were obtained over seven steps via Barton-McCombie deoxygenation, acetolysis and subsequent Vorbrüggen glycosylation, according to literature procedures.[23–25] The key 2′-phosphotriester precursors **7** and **8** were prepared in a four-step one-pot reaction by first converting **5** and **6** into the respective 2′-phosphoramidites, then condensing them with allyl alcohol, followed by oxidation with *tert*-butyl hydroperoxide (*t*BuOOH) and deprotection with dichloroacetic acid (DCA). Precursors **7** and **8** were subsequently coupled with commercially available adenosine and guanosine phosphoramidites **9** and **10** to give the 2′-5′ linked dinucleotides **11**, **12**

and **13**. Next, the allyl protecting group was removed with sodium iodide in refluxing acetone to provide the dinucleotides **14**, **15** and **16**. After precipitation and product isolation, 1-(mesitylene-2-sulfonyl)-3-nitro-1*H*-1,2,4-triazole (MSNT) was added to solutions containing **14–16** to activate the free phosphate for the cyclization key step, which established the 3′-5′ linkage. The raw cyclization products were not isolated, but directly subjected to a deprotection step with 33 % *v*/*v* methylamine in ethanol. We obtained the final compounds **1**, **2** and **3** after precipitation from cold acetone and purification by reverse-phase HPLC in the form of white powders.

The binding properties of dd-2′,3′-CDNs **1–3** were evaluated with nano differential scanning fluorimetry (nDSF) thermal shift experiments. To this end, we added increasing amounts of the compounds to recombinant hSTING and measured the protein melting curves. Binding of the ligand stabilizes the protein, which increases the T_m-value. As shown in Table 1 all our dd-2′,3′-CDNs stabilize hSTING. Natural 2′,3′-cGAMP generated the largest stabilization (ΔT_m) by 16.2 °C, followed by dd-2′,3′-cGAMP (**1**), which stabilized by 13.1 °C. This shows that the OH groups indeed influence the binding to STING but that they are not essential. In contrast dd-2′,3′-cAAMP (**2**) and dd-2′,3′-cAGMP (**3**) showed a significantly smaller stabilization effect of $\Delta T_m = 2$ °C. For dd-2′,3′-cAAMP (**2**) this is less than half compared to the OH-containing reference compound 2′,3′-cAAMP with $\Delta T_m = 5.5$ °C. These data suggest that the nucleoside exchange from G to A has a much more dramatic influence on binding than the OH groups.

We next performed isothermal titration calorimetry (ITC) to gain deeper insight into the binding event (Table 1). Indeed, the lack of the two OH groups reduced the affinity, but binding was still observed in the submicromolar regime. For dd-2′,3′-cGAMP (**1**) we determined a K_D of 445 nM, mostly because of a loss of enthalpic stabilization. dd-2′,3′-cAAMP (**2**) showed reduced binding compared

Table 1: EC$_{50}$ and affinity data of dd-2′,3′-CDNs **1–3**.[a]

Compound	EC$_{50}$ [μM][b]	ΔT_m [°C] (nDSF)[c]	K_D [μM] (ITC)[d]
dd-2′,3′-cGAMP (**1**)	7.4 ± 1.7	13.1	0.45 ± 0.23
dd-2′,3′-cAAMP (**2**)	74.4 ± 4.6	1.90 ± 0.04	15.1 ± 14.5
dd-2′,3′-cAGMP (**3**)	>110	2.30 ± 0.02	42.9 ± 35.1
2′,3′-cAAMP	26.6 ± 4.9	5.50 ± 0.01	4.98 ± 0.82
2′,3′-cGAMP	10.6[e]	16.2 ± 0.1	0.004[f]

[a] Green: Synthesized dd-2′,3′-CDNs **1–3**. Blue: OH-containing reference compounds. [b] EC$_{50}$ values were measured in THP-1-Dual monocytic cells in three independent experiments. [c] Thermal shift temperatures are obtained from nDSF experiments. The temperature represents the difference in melting temperature between 5 μM hSTING incubated with 100 μM of the respective ligand and 5 μM hSTING without ligand. The results are mean values from three independent experiments. [d] K_D values are calculated from ITC experiments with an error from the individual fit of the binding model to the experimental data. [e] A single-replicate experiment was conducted to confirm literature known EC$_{50}$ values of 2′,3′-cGAMP.[27] [f] K_D value published by Zhang et al.[10]

Angew. Chem. Int. Ed. **2022**, *61*, e202207175 (2 of 5)

© 2022 The Authors. Angewandte Chemie International Edition published by Wiley-VCH GmbH
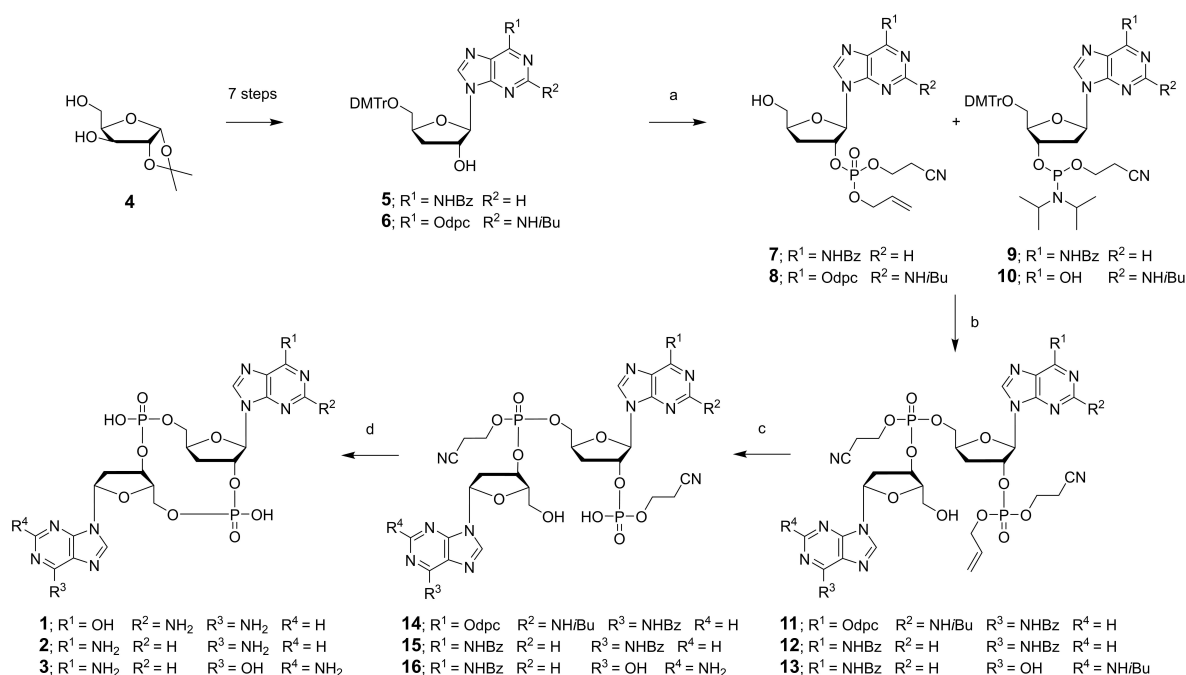
Scheme 1. Synthesis of dd-2′,3′-cGAMP derivatives **1**, **2** and **3**. Conditions: a) 1. 2-Cyanoethyl *N,N,N′,N′*-tetraisopropylphosphorodiamidite, pyridine trifluoroacetate, DCM, RT, 3 h; 2. BTT, allyl alcohol, RT, 1 h; 3. *t*BuOOH, RT, 40 min; 4. 3% *v/v* DCA in DCM, RT, 15 min; b) 1. BTT, MeCN, RT, 1 h; 2. *t*BuOOH, RT, 40 min; 3. 3% *v/v* DCA in DCM, RT, 10 min; c) NaI in acetone, reflux, 3 h; d) 1. MSNT, pyridine, RT, 18 h; 2. 33% *v/v* MeNH$_2$ in EtOH, RT, 4 h.

to reference compound 2′,3′-cAAMP by a factor of 3, while for dd-2′,3′-cAGMP (**3**) binding shifted to a higher micromolar value. Most importantly, all compounds, particularly dd-2′,3′-cGAMP (**1**) with a K_D of 0.5 µM, have a higher binding affinity to STING compared to other recently reported nucleoside agonists.[26]

To investigate the in cellulo activity of the prepared dd-2′,3′-CDNs **1**, **2** and **3**, we next measured their ability to induce an interferon response in immune cells (Table 1). For this purpose, we used a THP-1 monocytic reporter cell line containing a Lucia luciferase gene under the control of a promoter that is stimulated by 5 IFN-stimulated response elements. This allows to study the activation of the interferon pathway by measuring luminescence intensities. For control studies we used a THP-1 reporter cell line with STING being knocked out (STING-KO). For dd-2′,3′-cGAMP (**1**) and dd-2′,3′-cAAMP (**2**) ($c = 200$–300 µM, 37 °C, 24 h) we did not detect luminescence in the STING-KO control cell line, showing that both compounds operate as expected in a strictly STING-dependent fashion. In contrast, STING-competent THP-1 cells showed a strong luminescence response upon 2′,3′-cGAMP treatment. Concentration-dependent studies allowed us to determine an EC$_{50}$ of 10.6 µM for 2′,3′-cGAMP, which is in good agreement with literature data.[27] When performing the measurements using dd-2′,3′-cGAMP (**1**) we again determined a strictly STING-dependent response with an EC$_{50}$ of 7.4 µM, which is even slightly lower compared to natural 2′,3′-cGAMP itself. This is surprising given that the lack of 3′-OH groups reduces the affinity to STING. One possible explanation could be a different cellular uptake triggered by the lacking two OH

groups. For reference compound 2′,3′-cAAMP we measured an EC$_{50}$ of 27 µM and for dd-2′,3′-cAAMP (**2**) an EC$_{50}$ of 74 µM was determined. The dd-2′,3′-cAGMP (**3**) derivative gave an EC$_{50}$ of > 110 µM. These results show that all dideoxy compounds show in cellulo STING activation. In the case of dd-2′,3′-cGAMP (**1**) it goes even beyond the capability of parent compound 2′,3′-cGAMP.

To test the stability of dd-2′,3′-CDNs **1** and **2** towards poxin degradation and compare it with 2′,3′-cGAMP, BHK-21 cells were infected with vaccinia virus WR ($\approx 1 \times 10^7$ PFUs) for one hour and subsequently incubated for another 14 hours to allow expression of viral particles and poxin enzymes. Cell lysates were prepared in a lysis buffer providing suitable conditions for maintaining the enzymatic activity of the poxins.[9] After removal of cell debris and protein quantification, 30 ng of total protein lysate per sample were incubated either with 2′,3′-cGAMP or with compounds **1** and **2** for up to 24 hours, thereby establishing a time course experiment with increasing sampling time intervals. Upon sampling, enzymes were inactivated by addition of a phenol: chloroform mixture (1:1). The aqueous fractions of the samples were purified and subsequently analyzed by LC–MS. Here, all compounds were unequivocally identified via their exact mass and quantified via their UV absorption at 260 nm. The resulting data is depicted in Figure 2. Our data show that the OH- containing reference compound 2′,3′-cGAMP is quickly hydrolyzed by the viral poxins. This is not the case for the dideoxy compounds. Indeed, our data show that dd-2′,3′-CDNs **1** and **2** are stable towards poxin degradation and therefore able to evade the viral degradation response. Taken together, dd-
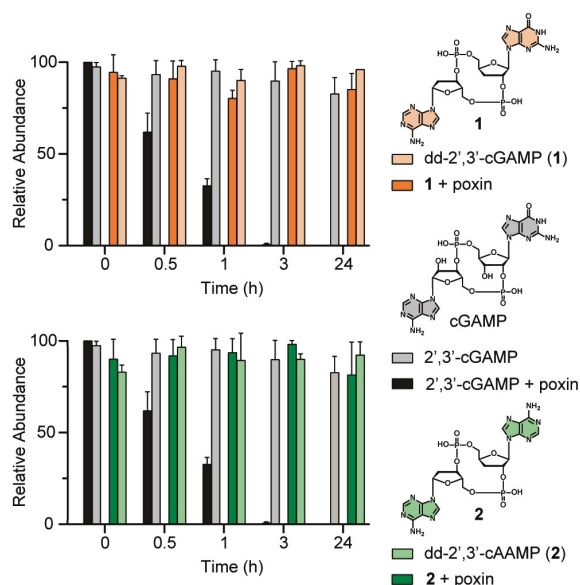
Figure 2. Stability of the dd-2′,3′-CDNs **1** and **2** and of the reference compound 2′,3′-cGAMP against poxin catalyzed degradation. ▨=**1**, ▨=**1**+poxin; ▨=2′,3′-cGAMP, ■=2′,3′-cGAMP+poxin; ▨=**2**, ▨=**2**+poxin. All values are normalized to the amount of compound present at $t=0$ h, which was set to 100%. Error bars represent the standard deviation of three independent experimental replicates.

Figure 3. Schematic presentation of the in vivo xenograft tumor mouse model and the in vivo data, which show a dramatic control of the tumor growth particularly with dd-2′,3′-cAAMP (**2**): Top: Treatment scheme. Mice were subcutaneously inoculated with RIL-175 tumor cells (hepatocellular carcinoma cells). Once tumors reached a mean volume of 20 mm³, intratumoral therapy on every third day was initiated. Solvent control or 15 nmol of 2′,3′-cGAMP, dd-2′,3′-cGAMP (**1**) or dd-2′,3′-cAAMP (**2**) were used for up to five treatments as depicted. Bottom: Tumor growth of CDN-treated tumors ($n=11$ for solvent control, $n=12$ for 2′,3′-cGAMP and dd-2′,3′-cAAMP (**2**) and $n=6$ for dd-2′,3′-cGAMP (**1**)). Mean tumor volume $+/-$ SEM is shown. Pooled data from two independent experiments are shown.

2′,3′-cGAMP (**1**) and dd-2′,3′-cAAMP (**2**) are stable STING agonists with reduced affinity but with remarkable EC$_{50}$ values.

In order to finally clarify how compounds **1** and **2** would behave in a tumor model, we examined their therapeutic efficacy in a mouse model of hepatocellular carcinoma (HCC) targeting mouse STING (mSTING). Analysis of published crystal structures and active site sequences shows that the interaction of mSTING and hSTING with the 3′-OH group should be similar.[7,28] For the study, 1×10^6 RIL-175 tumor cells were subcutaneously injected into C57BL/6 mice. The mice were treated five times by intratumoral injections of solvent control ($n=11$), 2′,3′-cGAMP ($n=12$), dd-2′,3′-cAAMP (**2**) ($n=12$) and dd-2′,3′-cGAMP (**1**) ($n=6$). The data together with a schematic representation of the experiment are shown in Figure 3. The data show that intratumoral injection of 2′,3′-cGAMP into RIL-175 tumors led to a significant delay in tumor growth (Figure 3 and Figure SI-5). Unexpectedly, we observed with dd-2′,3′-CDNs **1** and **2** a superior delay in tumor growth compared to parent compound 2′,3′-cGAMP (Figure 3 and Figure SI-5). At this point we believe that one reason for the better in vivo effect could be an improved cellular uptake of the dideoxy compounds as already hypothesized for the exceptional EC$_{50}$ values. In addition, the "less is more" paradigm could be at work here, which argues that a lower affinity of the compounds to the STING adaptor protein could result in a decreased T-cell toxicity, which has been described for high concentration of STING agonists.[29,30] Certainly, the surprisingly high EC$_{50}$ values and the strong in vivo tumor growth control require deeper mechanistic investigation.

In conclusion, we described the synthesis of 2′,3′-cGAMP dideoxy derivatives with superior in vivo characteristics for potential use as anti-viral and anti-tumoral therapeutics. The 2′- and 3′-OH groups of 2′,3′-cGAMP, which is the natural ligand for the adaptor protein STING, have been discussed as key elements that allow STING binding and enable STING to differentiate the 2′,3′-linked cGAMP derivative from 3′,3′-linked cyclic dinucleotides, of which the latter are key bacterial second messengers. The OH groups do affect binding of the ligands in two ways: first the 3′-OH group is known to establish a H-bond with Ser162 of the protein; second, the OH groups change and define the pucker of the ribose unit.[10] In deoxyribonucleotides it is known that the ribose can exist both in the C2′-endo and C3′-endo conformation, while for the ribonucleotides containing a free 2′-OH groups, a clear conformational preference for the C3′-endo conformation is reported as needed for binding.[31] The synthesis of the key compounds dd-2′,3′-cGAMP (**1**) and of dd-2′,3′-cAAMP (**2**) were possible using a new and concise synthetic combination of phosphoramidite and phosphotriester chemistry. ITC measurements show that the OH groups have only a minor enthalpic effect, but they make binding entropically more unfavorable because of the less preorganized structure of the ribose unit (Figure SI-3 and Table SI-1). Despite this effect, all prepared dideoxy-compounds show specific STING binding and STING pathway activation. Due to the lack of the 2′-OH groups, which is exploited by poxins to initiate 2′,3′-cGAMP hydrolysis, our compounds resist poxin degradation. Unexpectedly, we

observe in a preclinical tumor model that particularly dd-2′,3′-cAAMP (**1**) is able to control the tumor growth far better than the parent compound and natural ligand 2′,3′-cGAMP.

Conflict of Interest

The authors declare no conflict of interest.

Data Availability Statement

The data that support the findings of this study are available from the corresponding author upon reasonable request.

[1] X. Tan, L. Sun, J. Chen, Z. J. Chen, *Annu. Rev. Microbiol.* **2018**, *72*, 447–478.

[2] G. P. Amarante-Mendes, S. Adjemian, L. M. Branco, L. C. Zanetti, R. Weinlich, K. R. Bortoluci, *Front. Immunol.* **2019**, *9*, 2379.

[3] K. N. Miller, S. G. Victorelli, H. Salmonowicz, N. Dasgupta, T. Liu, J. F. Passos, P. D. Adams, *Cell* **2021**, *184*, 5506–5526.

[4] A. Ablasser, M. Goldeck, T. Cavlar, T. Deimling, G. Witte, I. Röhl, K.-P. Hopfner, J. Ludwig, V. Hornung, *Nature* **2013**, *498*, 380–384.

[5] L. Sun, J. Wu, F. Du, X. Chen, Z. J. Chen, *Science* **2013**, *339*, 786–791.

[6] J. Wu, L. Sun, X. Chen, F. Du, H. Shi, C. Chen, Z. J. Chen, *Science* **2013**, *339*, 826–830.

[7] P. Gao, M. Ascano, Y. Wu, W. Barchet, B. L. Gaffney, T. Zillinger, A. A. Serganov, Y. Liu, R. A. Jones, G. Hartmann, T. Tuschl, D. J. Patel, *Cell* **2013**, *153*, 1094–1107.

[8] C. Zhang, G. Shang, X. Gui, X. Zhang, X.-C. Bai, Z. J. Chen, *Nature* **2019**, *567*, 394–398.

[9] J. B. Eaglesham, Y. Pan, T. S. Kupper, P. J. Kranzusch, *Nature* **2019**, *566*, 259–263.

[10] X. Zhang, H. Shi, J. Wu, X. Zhang, L. Sun, C. Chen, Z. J. Chen, *Mol. Cell* **2013**, *51*, 226–235.

[11] D. Gao, J. Wu, Y.-T. Wu, F. Du, C. Aroh, N. Yan, L. Sun, J. Chen Zhijian, *Science* **2013**, *341*, 903–906.

[12] M. Moriyama, T. Koshiba, T. Ichinohe, *Nat. Commun.* **2019**, *10*, 4624.

[13] X.-D. Li, J. Wu, D. Gao, H. Wang, L. Sun, J. Chen Zhijian, *Science* **2013**, *341*, 1390–1394.

[14] J. Paijo, M. Döring, J. Spanier, E. Grabski, M. Nooruzzaman, T. Schmidt, G. Witte, M. Messerle, V. Hornung, V. Kaever, U. Kalinke, *PLoS Pathog.* **2016**, *12*, e1005546.

[15] B. Sun, K. B. Sundström, J. J. Chew, P. Bist, E. S. Gan, H. C. Tan, K. C. Goh, T. Chawla, C. K. Tang, E. E. Ooi, *Sci. Rep.* **2017**, *7*, 3594.

[16] Y. Wang, J. Luo, A. Alu, X. Han, Y. Wei, X. Wei, *Mol. Cancer* **2020**, *19*, 136.

[17] L. T. Khoo, L.-Y. Chen, *EMBO Rep.* **2018**, *19*, e46935.

[18] J. Kwon, S. F. Bakhoum, *Cancer Discovery* **2020**, *10*, 26–39.

[19] A. Amouzegar, M. Chelvanambi, J. N. Filderman, W. J. Storkus, J. J. Luke, *Cancers* **2021**, *13*, 2695.

[20] D.-S. Kim, A. Endo, F. G. Fang, K.-C. Huang, X. Bao, H.-W. Choi, U. Majumder, Y. Y. Shen, S. Mathieu, X. Zhu, K. Sanders, T. Noland, M.-H. Hao, Y. Chen, J. Y. Wang, S. Yasui, K. TenDyke, J. Wu, C. Ingersoll, K. A. Loiacono, J. E. Hutz, N. Sarwar, *ChemMedChem* **2021**, *16*, 1741–1744.

[21] W. Chang, M. D. Altman, C. A. Lesburg, S. A. Perera, J. A. Piesvaux, G. K. Schroeder, D. F. Wyss, S. Cemerski, Y. Chen, E. DiNunzio, A. M. Haidle, T. Ho, I. Kariv, I. Knemeyer, J. E. Kopinja, B. M. Lacey, J. Laskey, J. Lim, B. J. Long, Y. Ma, M. L. Maddess, B.-S. Pan, J. P. Presland, E. Spooner, D. Steinhuebel, Q. Truong, Z. Zhang, J. Fu, G. H. Addona, A. B. Northrup, E. Parmee, J. R. Tata, D. J. Bennett, J. N. Cumming, T. Siu, B. W. Trotter, *J. Med. Chem.* **2022**, *65*, 5675–5689.

[22] J. Le Naour, L. Zitvogel, L. Galluzzi, E. Vacchelli, G. Kroemer, *Oncoimmunology* **2020**, *9*, 1777624–1777624.

[23] F. Hulpia, S. Van Calenbergh, G. Caljon, L. Maes, Universiteit Gent, Universiteit Antwerpen, WO2019076633, **2019**.

[24] A. Kumar, S. I. Khan, A. Manglani, Z. K. Khan, S. B. Katti, *Nucleosides Nucleotides Nucleic Acids* **1994**, *13*, 1049–1058.

[25] C. Meier, J. M. Neumann, F. Andre, Y. Henin, T. Huynh Dinh, *J. Org. Chem.* **1992**, *57*, 7300–7308.

[26] C. Ding, Z. Song, A. Shen, T. Chen, A. Zhang, *Acta Pharm. Sin. B* **2020**, *10*, 2272–2298.

[27] B. Novotná, L. Vaneková, M. Zavřel, M. Buděšínský, M. Dejmek, M. Smola, O. Gutten, Z. A. Tehrani, M. Pimková Polidarová, A. Brázdová, R. Liboska, I. Štěpánek, Z. Vavřina, T. Janduší, R. Nencka, L. Rulíšek, E. Bouřa, J. Brynda, O. Páv, G. Birkuš, *J. Med. Chem.* **2019**, *62*, 10676–10690.

[28] D. Lu, G. Shang, J. Li, Y. Lu, X.-C. Bai, X. Zhang, *Nature* **2022**, *604*, 557–562.

[29] K. E. Sivick, A. L. Desbien, L. H. Glickman, G. L. Reiner, L. Corrales, N. H. Surh, T. E. Hudson, U. T. Vu, B. J. Francica, T. Banda, G. E. Katibah, D. B. Kanne, J. J. Leong, K. Metchette, J. R. Bruml, C. O. Ndubaku, J. M. McKenna, Y. Feng, L. Zheng, S. L. Bender, C. Y. Cho, M. L. Leong, A. van Elsas, T. W. Dubensky, S. M. McWhirter, *Cell Rep.* **2018**, *25*, 3074–3085.

[30] M. F. Gulen, U. Koch, S. M. Haag, F. Schuler, L. Apetoh, A. Villunger, F. Radtke, A. Ablasser, *Nat. Commun.* **2017**, *8*, 427.

[31] W. Saenger, *Principles of Nucleic Acid Structure*, Springer, New York, **1984**.

6 List of Abbreviations

AGS	Aicardi-Goutieres Syndrome
ALS	Amyotrophic lateral sclerosis
ARF	ADP-ribosylation factor
ATP	Adenosine triphosphate
BHK21	Baby hamster kidney fibroblasts
c-di-AMP	cyclic-di-adenosine monophosphate
cGAMP	cyclic- guanosine monophosphate-adenosine monophosphate
cGAS	cyclic GMP-AMP synthase
CCF	Cytosolic chromatin fragment
CD8	cluster of differentiation 8
CDN	Cyclic dinucleotide
CIN	Chromosomal instabilities
COPI	coat protein complex I
COPII	coat protein complex II
CPT-11	irinotecan
CRBN	cereblon
CT26	Colorectal carcinoma cell line 26
CTT	C-terminus tail
Cys	cysteine
DAMP	Danger-associated molecular pattern
DC	dendritic cell
DDR	DNA damage response
DMXAA	5,6-dimethylxanthenone-4-acetic acid / Vadimezan
DNA	2'-deoxyribonucleic acid
DNase	deoxyribonuclease
dNTPase	deoxynucleoside triphosphohydrolase
E3 ligase	E3 ubiquitin ligase
EC_{50}	half maximal effective concentration
ENPP1	Ectonucleotide Pyrophosphatase/Phosphodiesterase 1
ER	endoplasmic reticulum

List of Abbreviations

ERGIC	endoplasmic-reticulum-Golgi intermediate compartment
gDNA	genomic DNA
GTP	Guanosine triphosphate
HI	heat inactivated
HIV	Human immunodeficiency virus
IFN	interferon
IFNAR	interferon-alpha/beta receptors
IKK	I kappa B kinase
IL-6	interleukin 6
IRF	interferon regulatory factor
ISG	interferon stimulated gene
dsDNA	double stranded DNA
ssDNA	single stranded DNA
LBD	ligand binding domain
LRRC8	Leucine-rich repeat-containing protein 8A
MAVS	Mitochondrial antiviral-signalling protein
MDA5	melanoma differentiation-associated protein 5
MMP	matrix metalloproteinase
MOMP	mitochondrial outer membrane permeabilization
mtDNA	mitochondrial DNA
MTT	3-(4,5-dimethylthiazol-2-yl)-2,5-diphenyltetrazolium bromide
MYD88	Myeloid differentiation primary response 88
NF-κB	Nuclear-Factor-kappa light-chain enhancer of activated B cells
NK cell	Natural killer cell
NLRC3	Nucleotide-binding by leucine-rich repeat containing protein 3
NOD2	Nucleotide-binding oligomerization domain-containing protein 2
PAMP	Pathogen-associated molecular pattern
PEG	polyethylene glycol
PD-I	Programmed cell death protein 1
PINK1	parkin and ubiquitin kinase
POI	Protein of interest

List of Abbreviations

PPG   Photocleavable protecting groups

PROTAC   Proteolysis Targeting Chimera

PRR   Pattern recognition receptor

RFC1   Reduced folate carrier 1

RIG-I   retinoic acid-inducible gene I

RLU   Relative light unit

RNA   ribonucleic acid

ssRNA   single stranded RNA

dsRNA   double stranded RNA

RNF5   Ring finger protein 5

SAMHD1   sterile alpha motif and HD domain-containing protein 1

SASP   senescence-associated secretory phenotype

SATE   S-acyl-2-thioethyl

SAVI   STING-associated vasculopathy with onset of infancy

Ser   serine

SLC19A1   solute carrier family 19 member 1

SLC46A2   solute carrier family 46 member 2

STAT   Signal transducer and activator of transcription

STEEP   STING ER exit protein

STIM1   Stromal interaction molecule

STING   Stimulator of interferon genes

hSTING human STING

mSTING   mouse STING

TBK1   Tank-binding kinase I

TDP 43 TAR DNA-binding protein 43

TFAM   transcription factor A, mitochondrial

THP-1   Human leukaemia monocytic cell line

TLR   Toll-like Receptor

TME   Tumour microenvironment

TNF   Tumor necrosis factor

TPOXX   Tecovirimat

List of Abbreviations

TREX-I	3'-prime repair exonuclease I
UPS	ubiquitin-proteasome system
VACV	Vaccinia virus

TREX-I   3'-prime repair exonuclease I

UPS   ubiquitin-proteasome system

VACV   Vaccinia virus

7 References

1.   Alberts, B. *et al. Molecular Biology of the Cell* (W.W. Norton & Company, 2017).

2.   Medzhitov, R. Recognition of microorganisms and activation of the immune response. *Nature.* **449,** 819–826 (2007).

3.   Silva-Gomes, S., Decout, A. & Nigou, J. Pathogen-Associated Molecular Patterns (PAMPs). In *Encyclopedia of Inflammatory Diseases,* edited by M. Parnham (Springer Basel, Basel, 2015), pp. 1–16.

4.   Vénéreau, E., Ceriotti, C. & Bianchi, M. E. DAMPs from Cell Death to New Life. *Front. Immunol.* **6,** 422 (2015).

5.   Boehm, T. & Swann, J. B. Origin and evolution of adaptive immunity. *Annu. Rev. Anim. Biosci.* **2,** 259–283 (2014).

6.   Netea, M. G., Schlitzer, A., Placek, K., Joosten, L. A. B. & Schultze, J. L. Innate and Adaptive Immune Memory: an Evolutionary Continuum in the Host's Response to Pathogens. *Cell Host Microbe.* **25,** 13–26 (2019).

7.   Takeuchi, O. & Akira, S. Pattern recognition receptors and inflammation. *Cell.* **140,** 805–820 (2010).

8.   Roers, A., Hiller, B. & Hornung, V. Recognition of Endogenous Nucleic Acids by the Innate Immune System. *Immunity.* **44,** 739–754 (2016).

9.   Kawai, T. & Akira, S. The role of pattern-recognition receptors in innate immunity: update on Toll-like receptors. *Nat. Immunol.* **11,** 373–384 (2010).

10.   Yoneyama, M., Onomoto, K., Jogi, M., Akaboshi, T. & Fujita, T. Viral RNA detection by RIG-I-like receptors. *Curr. Opin. Immunol.* **32,** 48–53 (2015).

11.   Sabbah, A. *et al.* Activation of innate immune antiviral responses by Nod2. *Nat. Immunol.* **10,** 1073–1080 (2009).

12.   Honda, K., Takaoka, A. & Taniguchi, T. Type I interferon corrected gene induction by the interferon regulatory factor family of transcription factors. *Immunity.* **25,** 349–360 (2006).

13.   Liu, S. *et al.* Phosphorylation of innate immune adaptor proteins MAVS, STING, and TRIF induces IRF3 activation. *Science.* **347,** aaa2630 (2015).

14.   Pestka, S., Krause, C. D. & Walter, M. R. Interferons, interferon-like cytokines, and their receptors. *Immunol. Rev.* **202,** 8–32 (2004).

15.   Björck, P., Leong, H. X. & Engleman, E. G. Plasmacytoid dendritic cell dichotomy: identification of IFN-α producing cells as a phenotypically and functionally distinct subset. *J. Immunol.* **186,** 1477–1485 (2011).

16.   Ali, S. *et al.* Sources of Type I Interferons in Infectious Immunity: Plasmacytoid Dendritic Cells Not Always in the Driver's Seat. *Front. Immunol.* **10,** 778 (2019).

17.   Thomas, C. *et al.* Structural linkage between ligand discrimination and receptor activation by type I interferons. *Cell.* **146,** 621–632 (2011).

18.   Schneider, W. M., Chevillotte, M. D. & Rice, C. M. Interferon-stimulated genes: a complex web of host defenses. *Annu. Rev. Immunol.* **32,** 513–545 (2014).

References

19. Gough, D. J., Messina, N. L., Clarke, C. J. P., Johnstone, R. W. & Levy, D. E. Constitutive type I interferon modulates homeostatic balance through tonic signaling. *Immunity.* **36,** 166–174 (2012).

20. Liu, T., Zhang, L., Joo, D. & Sun, S.-C. NF-κB signaling in inflammation. *Signal Transduct. Target. Ther.* **2** (2017).

21. Sun, S.-C. & Liu, Z.-G. A special issue on NF-κB signaling and function. *Cell Res.* **21,** 1–2 (2011).

22. Sun, S.-C. The non-canonical NF-κB pathway in immunity and inflammation. *Nat. Rev. Immunol.* **17,** 545–558 (2017).

23. Hayden, M. S., West, A. P. & Ghosh, S. NF-kappaB and the immune response. *Oncogene.* **25,** 6758–6780 (2006).

24. McNab, F., Mayer-Barber, K., Sher, A., Wack, A. & O'Garra, A. Type I interferons in infectious disease. *Nat. Rev. Immunol.* **15,** 87–103 (2015).

25. Barnett, K. C. *et al.* Phosphoinositide Interactions Position cGAS at the Plasma Membrane to Ensure Efficient Distinction between Self- and Viral DNA. *Cell.* **176,** 1432-1446.e11 (2019).

26. Civril, F. *et al.* Structural mechanism of cytosolic DNA sensing by cGAS. *Nature.* **498,** 332–337 (2013).

27. Kranzusch, P. J., Lee, A. S.-Y., Berger, J. M. & Doudna, J. A. Structure of human cGAS reveals a conserved family of second-messenger enzymes in innate immunity. *Cell Rep.* **3,** 1362–1368 (2013).

28. Li, X. *et al.* Cyclic GMP-AMP synthase is activated by double-stranded DNA-induced oligomerization. *Immunity.* **39,** 1019–1031 (2013).

29. Zhang, X. *et al.* The cytosolic DNA sensor cGAS forms an oligomeric complex with DNA and undergoes switch-like conformational changes in the activation loop. *Cell Rep.* **6,** 421–430 (2014).

30. Zhou, W. *et al.* Structure of the Human cGAS-DNA Complex Reveals Enhanced Control of Immune Surveillance. *Cell.* **174,** 300-311.e11 (2018).

31. Andreeva, L. *et al.* cGAS senses long and HMGB/TFAM-bound U-turn DNA by forming protein-DNA ladders. *Nature.* **549,** 394–398 (2017).

32. Du, M. & Chen, Z. J. DNA-induced liquid phase condensation of cGAS activates innate immune signaling. *Science.* **361,** 704–709 (2018).

33. Ablasser, A. *et al.* cGAS produces a 2'-5'-linked cyclic dinucleotide second messenger that activates STING. *Nature.* **498,** 380–384 (2013).

34. Gao, P. *et al.* Cyclic G(2',5')pA(3',5')p is the metazoan second messenger produced by DNA-activated cyclic GMP-AMP synthase. *Cell.* **153,** 1094–1107 (2013).

35. Sun, L., Wu, J., Du, F., Chen, X. & Chen, Z. J. Cyclic GMP-AMP synthase is a cytosolic DNA sensor that activates the type I interferon pathway. *Science.* **339,** 786-791 (2013).

36. Zhang, X. *et al.* Cyclic GMP-AMP containing mixed phosphodiester linkages is an endogenous high-affinity ligand for STING. *Mol. Cell.* **51,** 226–235 (2013).

37. Diner, E. J. *et al.* The innate immune DNA sensor cGAS produces a noncanonical cyclic dinucleotide that activates human STING. *Cell Rep.* **3,** 1355–1361 (2013).

References

38. Ishikawa, H. & Barber, G. N. STING is an endoplasmic reticulum adaptor that facilitates innate immune signalling. *Nature.* **455,** 674–678 (2008).

39. Yin, Q. *et al.* Cyclic di-GMP sensing via the innate immune signaling protein STING. *Mol. Cell.* **46,** 735–745 (2012).

40. Shang, G. *et al.* Crystal structures of STING protein reveal basis for recognition of cyclic di-GMP. *Nat. Struct. Mol. Biol.* **19,** 725–727 (2012).

41. Ouyang, S. *et al.* Structural analysis of the STING adaptor protein reveals a hydrophobic dimer interface and mode of cyclic di-GMP binding. *Immunity.* **36,** 1073–1086 (2012).

42. Shang, G., Zhang, C., Chen, Z. J., Bai, X.-C. & Zhang, X. Cryo-EM structures of STING reveal its mechanism of activation by cyclic GMP–AMP. *Nature.* **567,** 389–393 (2019).

43. Ergun, S. L., Fernandez, D., Weiss, T. M. & Li, L. STING Polymer Structure Reveals Mechanisms for Activation, Hyperactivation, and Inhibition. *Cell.* **178,** 290-301.e10 (2019).

44. Gui, X. *et al.* Autophagy induction via STING trafficking is a primordial function of the cGAS pathway. *Nature.* **567,** 262–266 (2019).

45. Zhao, B. *et al.* A conserved PLPLRT/SD motif of STING mediates the recruitment and activation of TBK1. *Nature.* **569,** 718–722 (2019).

46. Saitoh, T. *et al.* Atg9a controls dsDNA-driven dynamic translocation of STING and the innate immune response. *Proc. Natl. Acad. Sci. U.S.A.* **106,** 20842–20846 (2009).

47. Mukai, K. *et al.* Activation of STING requires palmitoylation at the Golgi. *Nat. Commun.* **7,** 11932 (2016).

48. Haag, S. M. *et al.* Targeting STING with covalent small-molecule inhibitors. *Nature.* **559,** 269–273 (2018).

49. Zhang, C. *et al.* Structural basis of STING binding with and phosphorylation by TBK1. *Nature.* **567,** 394–398 (2019).

50. Zhao, B. *et al.* Structural basis for concerted recruitment and activation of IRF-3 by innate immune adaptor proteins. *Proc. Natl. Acad. Sci. U.S.A.* **113,** E3403-3412 (2016).

51. Mukai, K. *et al.* Homeostatic regulation of STING by retrograde membrane traffic to the ER. *Nat. Commun.* **12,** 61 (2021).

52. Oliveira Mann, C. C. de *et al.* Modular Architecture of the STING C-Terminal Tail Allows Interferon and NF-κB Signaling Adaptation. *Cell Rep.* **27,** 1165-1175.e5 (2019).

53. Fang, R. *et al.* NEMO-IKKβ Are Essential for IRF3 and NF-κB Activation in the cGAS-STING Pathway. *J. Immunol.* **199,** 3222–3233 (2017).

54. Cerboni, S. *et al.* Intrinsic antiproliferative activity of the innate sensor STING in T lymphocytes. *J. Exp. Med.* **214,** 1769–1785 (2017).

55. Balka, K. R. *et al.* TBK1 and IKKε Act Redundantly to Mediate STING-Induced NF-κB Responses in Myeloid Cells. *Cell Rep.* **31,** 107492 (2020).

56. Bakhoum, S. F. *et al.* Chromosomal instability drives metastasis through a cytosolic DNA response. *Nature.* **553,** 467–472 (2018).

57. Hou, Y. *et al.* Non-canonical NF-κB Antagonizes STING Sensor-Mediated DNA Sensing in Radiotherapy. *Immunity.* **49,** 490-503.e4 (2018).

References

58.   Chen, H. *et al.* Activation of STAT6 by STING is critical for antiviral innate immunity. *Cell.* **147,** 436–446 (2011).

59.   Li, X.-D. *et al.* Pivotal roles of cGAS-cGAMP signaling in antiviral defense and immune adjuvant effects. *Science.* **341,** 1390–1394 (2013).

60.   Gao, D. *et al.* Cyclic GMP-AMP synthase is an innate immune sensor of HIV and other retroviruses. *Science.* **341,** 903–906 (2013).

61.   Lahaye, X. *et al.* NONO Detects the Nuclear HIV Capsid to Promote cGAS-Mediated Innate Immune Activation. *Cell.* **175,** 488-501.e22 (2018).

62.   Mankan, A. K. *et al.* Cytosolic RNA:DNA hybrids activate the cGAS-STING axis. *EMBO J.* **33,** 2937–2946 (2014).

63.   Collins, A. C. *et al.* Cyclic GMP-AMP Synthase Is an Innate Immune DNA Sensor for Mycobacterium tuberculosis. *Cell Host Microbe.* **17,** 820–828 (2015).

64.   Hansen, K. *et al.* Listeria monocytogenes induces IFNβ expression through an IFI16-, cGAS- and STING-dependent pathway. *EMBO J.* **33,** 1654–1666 (2014).

65.   Watson, R. O. *et al.* The Cytosolic Sensor cGAS Detects Mycobacterium tuberculosis DNA to Induce Type I Interferons and Activate Autophagy. *Cell Host Microbe.* **17,** 811–819 (2015).

66.   Woodward, J. J., Iavarone, A. T. & Portnoy, D. A. c-di-AMP secreted by intracellular Listeria monocytogenes activates a host type I interferon response. *Science.* **328,** 1703–1705 (2010).

67.   White, M. J. *et al.* Apoptotic caspases suppress mtDNA-induced STING-mediated type I IFN production. *Cell.* **159,** 1549–1562 (2014).

68.   Riley, J. S. *et al.* Mitochondrial inner membrane permeabilisation enables mtDNA release during apoptosis. *EMBO J.* **37,** e99238 (2018).

69.   West, A. P. *et al.* Mitochondrial DNA stress primes the antiviral innate immune response. *Nature.* **520,** 553–557 (2015).

70.   Bahat, A., MacVicar, T. & Langer, T. Metabolism and Innate Immunity Meet at the Mitochondria. *Front. Cell Dev. Biol.* **9,** 720490 (2021).

71.   Aarreberg, L. D. *et al.* Interleukin-1β Induces mtDNA Release to Activate Innate Immune Signaling via cGAS-STING. *Mol. Cell.* **74,** 801-815.e6 (2019).

72.   Moriyama, M., Koshiba, T. & Ichinohe, T. Influenza A virus M2 protein triggers mitochondrial DNA-mediated antiviral immune responses. *Nat. Commun.* **10,** 4624 (2019).

73.   Sun, B. *et al.* Dengue virus activates cGAS through the release of mitochondrial DNA. *Sci. Rep.* **7,** 3594 (2017).

74.   Harding, S. M. *et al.* Mitotic progression following DNA damage enables pattern recognition within micronuclei. *Nature.* **548,** 466–470 (2017).

75.   Freund, A., Laberge, R.-M., Demaria, M. & Campisi, J. Lamin B1 loss is a senescence-associated biomarker. *Mol. Biol. Cell.* **23,** 2066–2075 (2012).

76.   Coquel, F. *et al.* SAMHD1 acts at stalled replication forks to prevent interferon induction. *Nature.* **557,** 57–61 (2018).

77.   Park, K. *et al.* Aicardi-Goutières syndrome-associated gene SAMHD1 preserves genome integrity by preventing R-loop formation at transcription-replication conflict regions. *PLoS Genet.* **17,** e1009523 (2021).

78. Hatch, E. M., Fischer, A. H., Deerinck, T. J. & Hetzer, M. W. Catastrophic nuclear envelope collapse in cancer cell micronuclei. *Cell.* **154,** 47–60 (2013).

79. Mackenzie, K. J. *et al.* cGAS surveillance of micronuclei links genome instability to innate immunity. *Nature.* **548,** 461–465 (2017).

80. te Poele, Robert H. *et al*. DNA Damage Is Able to Induce Senescence in Tumor Cells in Vitro and in Vivo 1. *Cancer Res.* **62,** 1876-1883 (2002).

81. Kuilman, T. & Peeper, D. S. Senescence-messaging secretome: SMS-ing cellular stress. *Nat. Rev. Cancer.* **9,** 81–94 (2009).

82. Lecot, P., Alimirah, F., Desprez, P.-Y., Campisi, J. & Wiley, C. Context-dependent effects of cellular senescence in cancer development. *Br. J. Cancer.* **114,** 1180–1184 (2016).

83. Childs, B. G., Durik, M., Baker, D. J. & van Deursen, J. M. Cellular senescence in aging and age-related disease: from mechanisms to therapy. *Nat. Med.* **21,** 1424–1435 (2015).

84. van Deursen, J. M. The role of senescent cells in ageing. *Nature.* **509,** 439–446 (2014).

85. Campisi, J. Aging, cellular senescence, and cancer. *Annu. Rev. Physiol.* **75,** 685–705 (2013).

86. Yang, H., Wang, H., Ren, J., Chen, Q. & Chen, Z. J. cGAS is essential for cellular senescence. *Proc. Natl. Acad. Sci. U.S.A.* **114,** E4612-4620 (2017).

87. Glück, S. *et al.* Innate immune sensing of cytosolic chromatin fragments through cGAS promotes senescence. *Nat. Cell Biol.* **19,** 1061–1070 (2017).

88. Takahashi, A. *et al.* Downregulation of cytoplasmic DNases is implicated in cytoplasmic DNA accumulation and SASP in senescent cells. *Nat. Commun.* **9,** 1249 (2018).

89. Dou, Z. *et al.* Cytoplasmic chromatin triggers inflammation in senescence and cancer. *Nature.* **550,** 402–406 (2017).

90. Kang, T.-W. *et al.* Senescence surveillance of pre-malignant hepatocytes limits liver cancer development. *Nature.* **479,** 547–551 (2011).

91. Lujambio, A. *et al.* Non-cell-autonomous tumor suppression by p53. *Cell.* **153,** 449–460 (2013).

92. Iannello, A. *et al*. p53-dependent chemokine production by senescent tumor cells supports NKG2D-dependent tumor elimination by natural killer cells. *J. Exp. Med.* **210,** 2057–2069 (2013).

93. Faget, D. V., Ren, Q. & Stewart, S. A. Unmasking senescence: context-dependent effects of SASP in cancer. *Nat. Rev. Cancer.* **19,** 439–453 (2019).

94. Ahn, J. & Barber, G. N. Self-DNA, STING-dependent signaling and the origins of autoinflammatory disease. *Curr. Opin. Immunol.* **31,** 121–126 (2014).

95. Gao, D. *et al.* Activation of cyclic GMP-AMP synthase by self-DNA causes autoimmune diseases. *Proc. Natl. Acad. Sci. U.S.A.* **112,** E5699-5705 (2015).

96. Seo, G. J. *et al.* Akt Kinase-Mediated Checkpoint of cGAS DNA Sensing Pathway. *Cell Rep.* **13,** 440–449 (2015).

97. Li, L. *et al.* Hydrolysis of 2'3'-cGAMP by ENPP1 and design of nonhydrolyzable analogs. *Nat. Chem. Biol.* **10,** 1043–1048 (2014).

References

98.   Bischoff, E., Tran-Thi, T. A. & Decker, K. F. Nucleotide pyrophosphatase of rat liver. A comparative study on the enzymes solubilized and purified from plasma membrane and endoplasmic reticulum. *Eur. J. Biochem.* **51,** 353–361 (1975).

99.   Eaglesham, J. B., Pan, Y., Kupper, T. S. & Kranzusch, P. J. Viral and metazoan poxins are cGAMP-specific nucleases that restrict cGAS-STING signalling. *Nature.* **566,** 259–263 (2019).

100.   Ablasser, A. *et al.* Cell intrinsic immunity spreads to bystander cells via the intercellular transfer of cGAMP. *Nature.* **503,** 530–534 (2013).

101.   Chen, Q. *et al.* Carcinoma-astrocyte gap junctions promote brain metastasis by cGAMP transfer. *Nature.* **533,** 493–498 (2016).

102.   Gentili, M. *et al.* Transmission of innate immune signaling by packaging of cGAMP in viral particles. *Science.* **349,** 1232–1236 (2015).

103.   Ritchie, C., Cordova, A. F., Hess, G. T., Bassik, M. C. & Li, L. SLC19A1 Is an Importer of the Immunotransmitter cGAMP. *Mol. Cell.* **75,** 372-381.e5 (2019).

104.   Cordova, A. F., Ritchie, C., Böhnert, V. & Li, L. Human SLC46A2 Is the Dominant cGAMP Importer in Extracellular cGAMP-Sensing Macrophages and Monocytes. *ACS Cent. Sci.* **7,** 1073–1088 (2021).

105.   Zhou, C. *et al.* Transfer of cGAMP into Bystander Cells via LRRC8 Volume-Regulated Anion Channels Augments STING-Mediated Interferon Responses and Anti-viral Immunity. *Immunity.* **52,** 767-781.e6 (2020).

106.   Srikanth, S. *et al.* The Ca2+ sensor STIM1 regulates the type I interferon response by retaining the signaling adaptor STING at the endoplasmic reticulum. *Nat. Immunol.* **20,** 152–162 (2019).

107.   Zhang, B.-C. *et al.* STEEP mediates STING ER exit and activation of signaling. *Nat Immunol.* **21,** 868–879 (2020).

108.   Zhang, L. *et al.* NLRC3, a member of the NLR family of proteins, is a negative regulator of innate immune signaling induced by the DNA sensor STING. *Immunity.* **40,** 329–341 (2014).

109.   Gonugunta, V. K. *et al.* Trafficking-Mediated STING Degradation Requires Sorting to Acidified Endolysosomes and Can Be Targeted to Enhance Anti-tumor Response. *Cell Rep.* **21,** 3234–3242 (2017).

110.   Zhong, B. *et al.* The ubiquitin ligase RNF5 regulates antiviral responses by mediating degradation of the adaptor protein MITA. *Immunity.* **30,** 397–407 (2009).

111.   Liu, D. *et al.* STING directly activates autophagy to tune the innate immune response. *Cell Death Differ.* **26,** 1735–1749 (2019).

112.   Nassour, J. *et al.* Autophagic cell death restricts chromosomal instability during replicative crisis. *Nature.* **565,** 659–663 (2019).

113.   Chen, D. S. & Mellman, I. Oncology meets immunology: the cancer-immunity cycle. *Immunity.* **39,** 1–10 (2013).

114.   Kwon, J. & Bakhoum, S. F. The Cytosolic DNA-Sensing cGAS-STING Pathway in Cancer. *Cancer Discov.* **10,** 26–39 (2020).

115.   Fu, C. & Jiang, A. Dendritic Cells and CD8 T Cell Immunity in Tumor Microenvironment. *Front. Immunol.* **9,** 3059 (2018).

References

116. Fuertes, M. B. *et al.* Host type I IFN signals are required for antitumor CD8+ T cell responses through CD8{alpha}+ dendritic cells. *J. Exp. Med.* **208,** 2005–2016 (2011).

117. Diamond, M. S. *et al.* Type I interferon is selectively required by dendritic cells for immune rejection of tumors. *J. Exp. Med.* **208,** 1989–2003 (2011).

118. Woo, S.-R. *et al.* STING-dependent cytosolic DNA sensing mediates innate immune recognition of immunogenic tumors. *Immunity.* **41,** 830–842 (2014).

119. Diamond, J. M. *et al.* Exosomes Shuttle TREX1-Sensitive IFN-Stimulatory dsDNA from Irradiated Cancer Cells to DCs. *Cancer Immunol. Res.* **6,** 910–920 (2018).

120. Deng, L. *et al.* STING-Dependent Cytosolic DNA Sensing Promotes Radiation-Induced Type I Interferon-Dependent Antitumor Immunity in Immunogenic Tumors. *Immunity.* **41,** 843–852 (2014).

121. Wang, H. *et al.* cGAS is essential for the antitumor effect of immune checkpoint blockade. *Proc. Natl. Acad. Sci. U.S.A.* **114,** 1637–1642 (2017).

122. Schadt, L. *et al.* Cancer-Cell-Intrinsic cGAS Expression Mediates Tumor Immunogenicity. *Cell Rep.* **29,** 1236-1248.e7 (2019).

123. Khoo, L. T. & Chen, L.-Y. Role of the cGAS-STING pathway in cancer development and oncotherapeutic approaches. *EMBO Rep.* **19,** e46935 (2018).

124. Ahn, J. *et al.* Inflammation-driven carcinogenesis is mediated through STING. *Nat. Commun.* **5,** 5166 (2014).

125. Simmons, D. P. *et al.* Type I IFN drives a distinctive dendritic cell maturation phenotype that allows continued class II MHC synthesis and antigen processing. *J. Immunol.* **188,** 3116–3126 (2012).

126. Lee, P. Y. *et al.* Type I interferon modulates monocyte recruitment and maturation in chronic inflammation. *Am. J. Clin. Pathol.* **175,** 2023–2033 (2009).

127. Domeier, P. P. *et al.* B-Cell-Intrinsic Type 1 Interferon Signaling Is Crucial for Loss of Tolerance and the Development of Autoreactive B Cells. *Cell Rep.* **24,** 406–418 (2018).

128. Fujita, H., Asahina, A., Tada, Y., Fujiwara, H. & Tamaki, K. Type I interferons inhibit maturation and activation of mouse Langerhans cells. *J. Invest. Dermatol.* **125,** 126–133 (2005).

129. Marcus, A. *et al.* Tumor-Derived cGAMP Triggers a STING-Mediated Interferon Response in Non-tumor Cells to Activate the NK Cell Response. *Immunity.* **49,** 754-763.e4 (2018).

130. Luteijn, R. D. *et al.* SLC19A1 transports immunoreactive cyclic dinucleotides. *Nature.* **573,** 434–438 (2019).

131. Lahey, L. J. *et al.* LRRC8A:C/E Heteromeric Channels Are Ubiquitous Transporters of cGAMP. *Mol. Cell.* **80,** 578-591.e5 (2020).

132. Delaney, G., Jacob, S., Featherstone, C. & Barton, M. The role of radiotherapy in cancer treatment: estimating optimal utilization from a review of evidence-based clinical guidelines. *Cancer.* **104,** 1129–1137 (2005).

133. Kitai, Y. *et al.* DNA-Containing Exosomes Derived from Cancer Cells Treated with Topotecan Activate a STING-Dependent Pathway and Reinforce Antitumor Immunity. *J. Immunol.* **198,** 1649–1659 (2017).

References

134. Pantelidou, C. *et al.* PARP Inhibitor Efficacy Depends on CD8+ T-cell Recruitment via Intratumoral STING Pathway Activation in BRCA-Deficient Models of Triple-Negative Breast Cancer. *Cancer Discov.* **9,** 722–737 (2019).

135. Sen, T. *et al.* Targeting DNA Damage Response Promotes Antitumor Immunity through STING-Mediated T-cell Activation in Small Cell Lung Cancer. *Cancer Discov.* **9,** 646–661 (2019).

136. Wang, Z. *et al.* cGAS/STING axis mediates a topoisomerase II inhibitor-induced tumor immunogenicity. *J. Clin. Invest.* **129,** 4850–4862 (2019).

137. Parkes, E. E. *et al.* Activation of STING-Dependent Innate Immune Signaling By S-Phase-Specific DNA Damage in Breast Cancer. *J. Natl. Cancer Inst.* **109** (2017).

138. Corrales, L. *et al.* Direct Activation of STING in the Tumor Microenvironment Leads to Potent and Systemic Tumor Regression and Immunity. *Cell Rep.* **11,** 1018–1030 (2015).

139. Demaria, O. *et al.* STING activation of tumor endothelial cells initiates spontaneous and therapeutic antitumor immunity. *Proc. Natl. Acad. Sci. U.S.A.* **112,** 15408–15413 (2015).

140. Li, T. *et al.* Antitumor Activity of cGAMP via Stimulation of cGAS-cGAMP-STING-IRF3 Mediated Innate Immune Response. *Sci. Rep.* **6,** 19049 (2016).

141. Gisselsson, D. *et al.* Abnormal Nuclear Shape in Solid Tumors Reflects Mitotic Instability. *Am. J. Pathol.* **158,** 199–206 (2001).

142. Li, J. *et al.* Metastasis and Immune Evasion from Extracellular cGAMP Hydrolysis. *Cancer Discov.* **11,** 1212–1227 (2021).

143. Vijayan, D., Young, A., Teng, M. W. L. & Smyth, M. J. Targeting immunosuppressive adenosine in cancer. *Nat. Rev. Cancer.* **17,** 709–724 (2017).

144. Gulen, M. F. *et al.* Signalling strength determines proapoptotic functions of STING. *Nat. Commun.* **8,** 427 (2017).

145. Greten, F. R. & Grivennikov, S. I. Inflammation and Cancer: Triggers, Mechanisms, and Consequences. *Immunity.* **51,** 27–41 (2019).

146. Coppé, J.-P. *et al.* Senescence-associated secretory phenotypes reveal cell-nonautonomous functions of oncogenic RAS and the p53 tumor suppressor. *PLoS Biol.* **6,** 2853–2868 (2008).

147. Wang, T. *et al.* Senescent Carcinoma-Associated Fibroblasts Upregulate IL8 to Enhance Prometastatic Phenotypes. *Mol. Cancer Res.* **15,** 3–14 (2017).

148. Nardella, C. *et al.* Aberrant Rheb-mediated mTORC1 activation and Pten haploinsufficiency are cooperative oncogenic events. *Genes Dev.* **22,** 2172–2177 (2008).

149. Birch, J. & Gil, J. Senescence and the SASP: many therapeutic avenues. *Genes Dev.* **34,** 1565–1576 (2020).

150. Kirkland, J. L. & Tchkonia, T. Senolytic drugs: from discovery to translation. *J. Intern. Med.* **288,** 518–536 (2020).

151. Xu, M. *et al.* Senolytics improve physical function and increase lifespan in old age. *Nat. Med.* **24,** 1246–1256 (2018).

152. Gasek, N. S., Kuchel, G. A., Kirkland, J. L. & Xu, M. Strategies for Targeting Senescent Cells in Human Disease. *Nat. Aging.* **1,** 870–879 (2021).

153. Paez-Ribes, M., González-Gualda, E., Doherty, G. J. & Muñoz-Espín, D. Targeting senescent cells in translational medicine. *EMBO Mol. Med.* **11,** e10234 (2019).

References

154. Di Micco, R., Krizhanovsky, V., Baker, D. & Di d'Adda Fagagna, F. Cellular senescence in ageing: from mechanisms to therapeutic opportunities. *Nat. Rev. Mol. Cell Biol.* **22,** 75–95 (2021).

155. Crow, Y. J. *et al.* Mutations in the gene encoding the 3'-5' DNA exonuclease TREX1 cause Aicardi-Goutières syndrome at the AGS1 locus. *Nat. Genet.* **38,** 917–920 (2006).

156. Rodero, M. P. *et al.* Type I interferon-mediated autoinflammation due to DNase II deficiency. *Nat. Commun.* **8,** 2176 (2017).

157. Ahn, J., Gutman, D., Saijo, S. & Barber, G. N. STING manifests self DNA-dependent inflammatory disease. *Proc. Natl. Acad. Sci. U.S.A.* **109,** 19386–19391 (2012).

158. Liu, Y. *et al.* Activated STING in a vascular and pulmonary syndrome. *NEJM.* **371,** 507–518 (2014).

159. Watkin, L. B. *et al.* COPA mutations impair ER-Golgi transport and cause hereditary autoimmune-mediated lung disease and arthritis. *Nat. Genet.* **47,** 654–660 (2015).

160. Lepelley, A. *et al.* Mutations in COPA lead to abnormal trafficking of STING to the Golgi and interferon signaling. *J. Exp. Med.* **217** (2020).

161. Steiner, A. *et al. Activation of STING due to COPI-deficiency. bioRxiv.* (2020).

162. Yu, C.-H. *et al.* TDP-43 Triggers Mitochondrial DNA Release via mPTP to Activate cGAS/STING in ALS. *Cell.* **183,** 636-649.e18 (2020).

163. Sliter, D. A. *et al.* Parkin and PINK1 mitigate STING-induced inflammation. *Nature.* **561,** 258–262 (2018).

164. Amouzegar, A., Chelvanambi, M., Filderman, J. N., Storkus, W. J. & Luke, J. J. STING Agonists as Cancer Therapeutics. *Cancers.* **13,** 2695 (2021).

165. Lara, P. N. *et al.* Randomized phase III placebo-controlled trial of carboplatin and paclitaxel with or without the vascular disrupting agent vadimezan (ASA404) in advanced non-small-cell lung cancer. *J. Clin. Oncol.* **29,** 2965–2971 (2011).

166. Shih, A. Y., Damm-Ganamet, K. L. & Mirzadegan, T. Dynamic Structural Differences between Human and Mouse STING Lead to Differing Sensitivity to DMXAA. *Biophys. J.* **114,** 32–39 (2018).

167. Gremel, G. *et al.* Abstract 4522: Potent induction of a tumor-specific immune response by a cyclic dinucleotide STING agonist. *Cancer Res.* **80,** 4522 (2020).

168. Harrington, K. *et al.* 408 Phase I, first-in-human trial evaluating BI 1387446 (stimulator of interferon genes [STING] agonist) alone and combined with BI 754091 (anti-programmed cell death [PD]-1) in solid tumors. *J. Immunother. Cancer.* **8,** A433 (2020).

169. 33rd Annual Meeting & Pre-Conference Programs of the Society for Immunotherapy of Cancer (SITC 2018) : Washington, D.C., USA. 7-11 November 2018. *J Immunother Cancer.* **6,** 115 (2018).

170. Siu, T. *et al.* Discovery of a Novel cGAMP Competitive Ligand of the Inactive Form of STING. *ACS Med. Chem. Lett.* **10,** 92–97 (2019).

171. Li, S. *et al.* The Cyclopeptide Astin C Specifically Inhibits the Innate Immune CDN Sensor STING. *Cell Rep.* **25,** 3405-3421.e7 (2018).

References

172. Haag, S. M. *et al.* Targeting STING with covalent small-molecule inhibitors. *Nature.* **559,** 269–273 (2018).

173. Hansen, A. L. *et al.* Nitro-fatty acids are formed in response to virus infection and are potent inhibitors of STING palmitoylation and signaling. *Proc. Natl. Acad. Sci. U.S.A.* **115,** E7768-7775 (2018).

174. Hong, Z. *et al.* STING inhibitors target the cyclic dinucleotide binding pocket. *Proc. Natl. Acad. Sci. U.S.A.* **118** (2021).

175. Novotná, B. *et al.* Enzymatic Preparation of 2'-5',3'-5'-Cyclic Dinucleotides, Their Binding Properties to Stimulator of Interferon Genes Adaptor Protein, and Structure/Activity Correlations. *J. Med. Chem.* **62,** 10676–10690 (2019).

176. Xie, X., Liu, J. & Wang, X. Design, Synthesis and Biological Evaluation of (2',5' and 3'5'-Linked) cGAMP Analogs that Activate Stimulator of Interferon Genes (STING). *Molecules.* **25,** 5285 (2020).

177. Kratz, A., Ferraro, M., Sluss, P. M. & Lewandrowski, K. B. Case records of the Massachusetts General Hospital. Weekly clinicopathological exercises. Laboratory reference values. *NEJM.* **351,** 1548–1563 (2004).

178. Kiss, M., Caro, A. A., Raes, G. & Laoui, D. Systemic Reprogramming of Monocytes in Cancer. *Front. Oncol.* **10,** 1399 (2020).

179. Olingy, C. E., Dinh, H. Q. & Hedrick, C. C. Monocyte heterogeneity and functions in cancer. *J. Leukoc. Biol.* **106,** 309–322 (2019).

180. Bosshart, H. & Heinzelmann, M. THP-1 cells as a model for human monocytes. *Ann. Transl. Med.* **4,** 438 (2016).

181. Takahashi T, Old LJ, Boyse EA. Surface alloantigens of plasma cells - first ENPP1 paper. *J. Exp. Med.* **131,** 1325-1341 (1970).

182. W. Howard Evans, Diana O. Hood and James W. Gurd. Purification and properties of a mouse liver plasma-membrane glycoprotein hydrolysing nucleotide pyrophosphate and phosphodiester bonds. *Biochem. J.* **135,** 819–826 (1973).

183. Huang, R. *et al.* Expression of the murine plasma cell nucleotide pyrophosphohydrolase PC-1 is shared by human liver, bone, and cartilage cells. Regulation of PC-1 expression in osteosarcoma cells by transforming growth factor-beta. *J. Clin. Invest.* **94,** 560–567 (1994).

184. Grobben, B. *et al.* Ecto-nucleotide pyrophosphatase modulates the purinoceptor-mediated signal transduction and is inhibited by purinoceptor antagonists. *Br. J. Pharmacol.* **130,** 139–145 (2000).

185. Namasivayam, V., Lee, S.-Y. & Müller, C. E. The promiscuous ectonucleotidase NPP1: molecular insights into substrate binding and hydrolysis. *Biochim. Biophys. Acta Gen. Subj.* **1861,** 603–614 (2017).

186. Kato, K. *et al.* Structural insights into cGAMP degradation by Ecto-nucleotide pyrophosphatase phosphodiesterase 1. *Nat. Commun.* **9,** 4424 (2018).

187. Sabina I. Belli, Ian R. van Driel and James W. Goding. Identification and characterization of a soluble form of the plasma cell membrane glycoprotein PC-1 (5'-nucleotide phosphodiesterase). *Eur. J. Biochem.* **217,** 421–428 (1993).

References

188. Frittitta L, Camastra S, Baratta R, et al. A soluble PC-1 circulates in human plasma: relationship with insulin resistance and associated abnormalities. *J. Clin. Endocr.* **84,** 3620–3625 (1999).

189. Georgana, I., Sumner, R. P., Towers, G. J. & Maluquer de Motes, C. Virulent Poxviruses Inhibit DNA Sensing by Preventing STING Activation. *J. Virol.* **92,** e02145-17 (2018).

190. Schröder, M., Baran, M. & Bowie, A. G. Viral targeting of DEAD box protein 3 reveals its role in TBK1/IKKepsilon-mediated IRF activation. *EMBO J.* **27,** 2147–2157 (2008).

191. Unterholzner, L. *et al.* Vaccinia virus protein C6 is a virulence factor that binds TBK-1 adaptor proteins and inhibits activation of IRF3 and IRF7. *PLoS Pathog.* **7,** e1002247 (2011).

192. Ferguson, B. J. *et al.* Vaccinia virus protein N2 is a nuclear IRF3 inhibitor that promotes virulence. *J. Gen. Virol.* **94,** 2070–2081 (2013).

193. Eaglesham, J. B., McCarty, K. L. & Kranzusch, P. J. Structures of diverse poxin cGAMP nucleases reveal a widespread role for cGAS-STING evasion in host-pathogen conflict. *eLife.* **9,** e59753 (2020).

194. Fenner, F. The global eradication of smallpox. *Med. J. Aust.* **1,** 455 (1980).

195. Yang, Z., Gray, M. & Winter, L. Why do poxviruses still matter?. *Cell Biosci.* **11,** 96 (2021).

196. Editorial. The spectre of smallpox lingers. *Nature.* **560,** 281 (2018).

197. Hoy, S. M. Tecovirimat: First Global Approval. *Drugs.* **78,** 1377–1382 (2018).

198. Rautio, J. *et al.* Prodrugs: design and clinical applications. *Nat. Rev. Drug Discov.* **7,** 255–270 (2008).

199. Najjar, A., Najjar, A. & Karaman, R. Newly Developed Prodrugs and Prodrugs in Development; an Insight of the Recent Years. *Molecules.* **25,** 884 (2020).

200. Ettmayer, P., Amidon, G. L., Clement, B. & Testa, B. Lessons learned from marketed and investigational prodrugs. *J. Med. Chem.* **47,** 2393–2404 (2004).

201. Liederer, B. M. & Borchardt, R. T. Enzymes involved in the bioconversion of ester-based prodrugs. *J. Pharm. Sci.* **95,** 1177–1195 (2006).

202. Hosokawa, M. Structure and catalytic properties of carboxylesterase isozymes involved in metabolic activation of prodrugs. *Molecules.* **13,** 412–431 (2008).

203. Bencharit, S. *et al.* Structural insights into CPT-11 activation by mammalian carboxylesterases. *Nat. Struct. Biol.* **9,** 337–342 (2002).

204. Schlienger, N. *et al.* S-Acyl-2-thioethyl aryl phosphotriester derivatives as mononucleotide prodrugs. *J Med Chem.* **43,** 4570–4574 (2000).

205. Peyrottes, S. *et al.* A step further in the SATE mononucleotide prodrug approach. *Nucleic Acids Symp. Ser. (Oxf).* 539–540 (2008).

206. Wang, D. *et al.* Human carboxylesterases: a comprehensive review. *Acta Pharm. Sin. B.* **8,** 699–712 (2018).

207. Bencharit, S., Morton, C. L., Xue, Y., Potter, P. M. & Redinbo, M. R. Structural basis of heroin and cocaine metabolism by a promiscuous human drug-processing enzyme. *Nat. Struct. Biol.* **10,** 349–356 (2003).

References

208. Bencharit, S. *et al.* Multisite promiscuity in the processing of endogenous substrates by human carboxylesterase 1. *J. Mol. Biol.* **363,** 201–214 (2006).

209. Stazzoni, S. Design and Synthesis of Clickable Nucleic Acid Analogues for Cancer Therapy and Diagnosis. LMU Munich, Faculty for Cemistry and Pharmacy, 2020.

210. Testero, S. A. *et al.* Sulfonate-containing thiiranes as selective gelatinase inhibitors. *ACS Med. Chem. Lett.* **2,** 177–181 (2011).

211. Lee, M. *et al.* Structure-Activity Relationship for Thiirane-Based Gelatinase Inhibitors. *ACS Med. Chem. Lett.* **3,** 490–495 (2012).

212. Hamada, Y. Recent progress in prodrug design strategies based on generally applicable modifications. *Bioorg. Med. Chem. Lett.* **27,** 1627–1632 (2017).

213. Piasentin, N., Milotti, E. & Chignola, R. The control of acidity in tumor cells: a biophysical model. *Sci. Rep.* **10,** 13613 (2020).

214. Akinboye, E. S., Rosen, M. D., Denmeade, S. R., Kwabi-Addo, B. & Bakare, O. Design, synthesis, and evaluation of pH-dependent hydrolyzable emetine analogues as treatment for prostate cancer. *J. Med. Chem.* **55,** 7450–7459 (2012).

215. Kratz, F. DOXO-EMCH (INNO-206): the first albumin-binding prodrug of doxorubicin to enter c linical trials. *Expert Opin. Investig. Drugs.* **16,** 855–866 (2007).

216. Nie, W. *et al.* Magnetic Nanoclusters Armed with Responsive PD-1 Antibody Synergistically Improved Adoptive T-Cell Therapy for Solid Tumors. *ACS Nano.* **13,** 1469–1478 (2019).

217. Ji, T. *et al.* Enhanced Natural Killer Cell Immunotherapy by Rationally Assembling Fc Fragments of Antibodies onto Tumor Membranes. *Adv. Mater.* **31,** e1804395 (2019).

218. Engels, J. & Schlaeger, E. J. Synthesis, structure, and reactivity of adenosine cyclic 3',5'-phosphate benzyl triesters. *J. Med. Chem.* **20,** 907–911 (1977).

219. Horspool, W. M. (ed.). *CRC handbook of organic photochemistry and photobiology.* 2nd ed. (CRC Press, Boca Raton, Fla., 2004).

220. Klán, P. *et al.* Photoremovable protecting groups in chemistry and biology: reaction mechanisms and efficacy. *Chem. Rev.* **113,** 119–191 (2013).

221. Ankenbruck, N., Courtney, T., Naro, Y. & Deiters, A. Optochemical Control of Biological Processes in Cells and Animals. *Angew. Chem. Int. Ed. Engl.* **57,** 2768–2798 (2018).

222. Zhao, W. *et al.* Remote Light-Responsive Nanocarriers for Controlled Drug Delivery: Advances and Perspectives. *Small.* **15,** e1903060 (2019).

223. Piston, D. Imaging living cells and tissues by two-photon excitation microscopy. *Trends Cell Biol.* **9,** 66–69 (1999).

224. Benninger, R. K. P. & Piston, D. W. Two-photon excitation microscopy for the study of living cells and tissues. *Curr. Protoc. Cell Biol.* **59,** 4.11.1-4.11.24 (2013).

225. Aujard, I. *et al.* o-nitrobenzyl photolabile protecting groups with red-shifted absorption: syntheses and uncaging cross-sections for one- and two-photon excitation. *Chemistry.* **12,** 6865–6879 (2006).

226. Lunzer, M. *et al.* A Modular Approach to Sensitized Two-Photon Patterning of Photodegradable Hydrogels. *Angew. Chem.* **130,** 15342–15347 (2018).

References

227. Sakamoto, K. M. *et al.* Protacs: chimeric molecules that target proteins to the Skp1-Cullin-F box complex for ubiquitination and degradation. *Proc. Natl. Acad. Sci. U.S.A.* **98,** 8554–8559 (2001).

228. Ottis, P. & Crews, C. M. Proteolysis-Targeting Chimeras: Induced Protein Degradation as a Therapeutic Strategy. *ACS Chem. Biol.* **12,** 892–898 (2017).

229. Burslem, G. M. & Crews, C. M. Proteolysis-Targeting Chimeras as Therapeutics and Tools for Biological Discovery. *Cell.* **181,** 102–114 (2020).

230. Bai, L. *et al.* A Potent and Selective Small-Molecule Degrader of STAT3 Achieves Complete Tumor Regression In Vivo. *Cancer Cell.* **36,** 498-511 (2019).

231. Ciechanover, A. & Schwartz, A. L. The ubiquitin-proteasome pathway: the complexity and myriad functions of proteins death. *Proc. Natl. Acad. Sci. U.S.A.* **95,** 2727–2730 (1998).

232. Deshaies, R. J. & Joazeiro, C. A. P. RING domain E3 ubiquitin ligases. *Annu. Rev. Biochem.* **78,** 399–434 (2009).

233. Buetow, L. & Huang, D. T. Structural insights into the catalysis and regulation of E3 ubiquitin ligases. *Nat. Rev. Mol. Cell. Biol.* **17,** 626–642 (2016).

234. Chamberlain, P. P. *et al.* Evolution of Cereblon-Mediated Protein Degradation as a Therapeutic Modality. *ACS Med. Chem. Lett.* **10,** 1592–1602 (2019).

235. Zou, Y. *et al.* Lenalidomide versus thalidomide based regimens as first-line therapy for patients with multiple myeloma. *Leuk. Lymphoma.* **54,** 2219–2225 (2013).

236. Latif, T., Chauhan, N., Khan, R., Moran, A. & Usmani, S. Z. Thalidomide and its analogues in the treatment of Multiple Myeloma. *Exp Hematol Oncol.* **1,** 27 (2012).

237. Cecchini, C., Pannilunghi, S., Tardy, S. & Scapozza, L. From Conception to Development: Investigating PROTACs Features for Improved Cell Permeability and Successful Protein Degradation. *Front. Chem.* **9,** 672267 (2021).

238. Prabakaran, T. *et al.* A STING antagonist modulating the interaction with STIM1 blocks ER-to-Golgi trafficking and inhibits lupus pathology. *EBioMedicine.* **66,** 103314 (2021).

239. Shultz, M. D. Two Decades under the Influence of the Rule of Five and the Changing Properties of Approved Oral Drugs. *J. Med. Chem.* **62,** 1701–1714 (2019).

240. Doak, B. C., Over, B., Giordanetto, F. & Kihlberg, J. Oral druggable space beyond the rule of 5: insights from drugs and clinical candidates. *Chem. Biol.* **21,** 1115–1142 (2014).

241. Wurz, R. P. *et al.* A "Click Chemistry Platform" for the Rapid Synthesis of Bispecific Molecules for Inducing Protein Degradation. *J. Med. Chem.* **61,** 453–461 (2018).

242. Shin, D., Sinkeldam, R. W. & Tor, Y. Emissive RNA alphabet. *J. Am. Chem. Soc.* **133,** 14912–14915 (2011).

Note: Various cellular biology vector images used in the figures in this thesis are available at Servier Medical Art, under smart.servier.com